Charmed-meson fragmentation functions with finite-mass corrections and their application in various processes

Dissertation zur Erlangung des
Doktorgrades des Department
Physik der Universität Hamburg

vorgelegt von

Torben Kneesch
aus Hamburg

Hamburg
2010

Erstgutachter der Dissertation:	Prof. Dr. B. A. Kniehl
Zweitgutachter der Dissertation:	Prof. Dr. G. Kramer
Erstgutachter der Disputation:	Prof. Dr. B. A. Kniehl
Zweitgutachter der Disputation:	Prof. Dr. J. Bartels
Datum der Disputation:	19. November 2010
Vorsitzender des Prüfungsausschusses:	Prof. Dr. G. Sigl
Vorsitzender des Promotionsausschusses:	Prof. Dr. J. Bartels
Dekan der MIN-Fakultät:	Prof. Dr. Heinrich Graener

Abstract

Charmed-meson fragmentation functions with finite-mass corrections and their application in various processes

We have calculated the single-inclusive production cross section of massive quarks in electron-positron-annihilation with next-to-leading order QCD corrections. With these results we have extracted fragmentation functions for the fragmentation from partons into D^0, D^+ and D^* mesons, where we have used experimental data from the B factories Belle and CLEO and from the ALEPH and OPAL experiments at the LEP collider. In our analysis we have included the masses of c and b quarks and of the D mesons and tested the evolution of fragmentation functions with a global fit spanning the B factories' center-of-mass energy of $\sqrt{s} = 10.5\,\mathrm{GeV}$ to LEP's run at the Z boson resonance at M_Z.

We have applied this fragmentation functions in deep inelastic scattering for comparisons with HERA data using parton cross sections from the literature available in program form. We have then modified this cross section to calculate predictions for deep inelastic two-photon-scattering. By applying the Weizsäcker-Williams spectrum on the real photon we have calculated predictions for LEP1, LEP2 and the future ILC experiments. For ILC we have also included a beamstrahlung spectrum. Finally we have calculated production cross sections for the planned $e\gamma$ mode of the ILC with the help of a Compton spectrum.

Zusammenfassung

Charm-Meson Fragmentierungsfunktionen mit endlichen Massenkorrekturen und ihre Anwendung in verschiedenen Prozessen

Wir haben den einfach-inklusiven Produktionswirkungsquerschnitt von massiven Quarks in Elektron-Positron-Annihilation mit QCD-Korrekturen der nächstführenden Ordnung berechnet. Mit diesen Ergebnissen haben wir die Fragmentierungsfunktionen für die Fragmentierung von Partonen in D^0, D^+ und D^* Mesonen extrahiert, wobei wir experimentelle Daten von den B-Fabriken Belle und CLEO und von den ALEPH- und OPAL-Experimenten am LEP-Beschleuniger benutzt haben. In unserer Analyse haben wir die Massen der c- und b-Quarks und der D-Mesonen berücksichtigt und die Evolution der Fragmentierungsfunktionen mit einem globalen Fit getestet, welcher von der Schwerpunktsenergie der B-Fabriken von $\sqrt{s} = 10.5\,\mathrm{GeV}$ bis zu dem LEP-Lauf auf der Z-Resonanz bei M_Z reicht.

Wir haben diese Fragmentierungsfunktionen in tief-inelastischer Streuung für Vergleiche zu HERA-Daten angewandt mittels Partonwirkungsquerschnitten aus der Literatur, die in Programmform verfügbar sind. Wir haben diese Wirkungsquerschnitte dann modifiziert, um Vorhersagen für tief-inelastische Zwei-Photon-Streuung zu berechnen. Durch Anwendung des Weizsäcker-Williams-Spektrums auf das reelle Photon haben wir Vorhersagen für LEP1, LEP2 und das zukünftige ILC Experiment berechnet. Für ILC haben wir auch ein Beamstrahlungsspektrum berücksichtigt. Zu guter Letzt haben wir mit Hilfe eines Compton-Spektrums Produktionsquerschnitte für den geplanten $e\gamma$-Modus des ILC berechnet.

Contents

Chapter 1

Introduction

The production of heavy hadrons is a topic of high interest in particle physics of the last few years. These production processes are characterized by the involvement of quarks with masses m much larger than the QCD scale Λ_{QCD}, so that the strong coupling $\alpha_s(m)$ is much smaller than one. This introduces a scale into the calculation which makes the production of the heavy quarks calculable in perturbative quantum chromodynamics (QCD) and provides a cutoff for initial- and final-state collinear singularities. The definition of heavy quarks includes the charm, bottom and top quark (c, b, t), while the up, down and strange quarks (u, d, s) are regarded as light quarks and being massless.

A lot of next-to-leading-order (NLO) QCD calculations including heavy quarks are available in the literature (e.g. [1, 2, 3, 4, 5]). The results are reliable as long as m is the only large scale in the process. However, when for example the center-of-mass system (CMS) energy $\sqrt{S}$ in electron-positron-annihilation or the transverse momentum p_T of the produced heavy particle in $\gamma\gamma$ collisions is much larger than m, the process in question becomes a multi-scale process. This leads to logarithms of the form $\ln(p_T^2/m^2)$ to all orders in the perturbation series, so that the convergence of the series breaks down.

The usual way to restore the validity of the perturbation series is by using a proper factorization scheme. In perturbative QCD the hadron production cross section is factorized into two parts. The first part is the parton cross section containing the short-range effects, which means a small coupling α_S in QCD. Therefore this part is calculable with pertubation theory. The second part of the factorization are the parton distribution functions (PDF) for initial-state hadrons and fragmentation functions (FF) for final-state hadrons. The PDF describes the likelihood to find a parton with a given momentum fraction inside the incoming hadron, while the FF is a measure for the probability, that an outgoing parton fragments into a hadron with a certain fraction of the parton's momentum. There is some ambiguity which terms are factorized into which part, so that several different factorization schemes exist. Their respective validity depends on the energy range of the process. Singularities or problematic logarithms are absorbed into the PDFs and FFs and resummed with the help of evolution equations. The predictive power of perturbative QCD comes from the fact, that the PDFs and FFs are process-independent. So they can be extracted from experimental data of one experiment to make predictions for other processes.

In the zero-mass variable-flavor-number scheme (ZM-VFNS) all quarks are treated as massless. To accomodate for different energies the number of active flavors n_f in the parton model is a variable which depends on the factorization scale μ_f. In this work the common approach is used to increase n_f by one when the factorization scale crosses a heavy-quark mass. This scheme works well for high energies where

the quark masses become negligible. A different approach is the fixed-flavor-number scheme (FFNS), where m is kept as a large scale and n_f is fixed. This leads to logarithms of the scales in the partonic cross sections. As mentioned, the result in this scheme is not valid when the logarithms are large enough to spoil the convergence of the perturbation series. But the scheme works fine when the involved additional scales are comparable to the heavy quark masses, so that those logarithms are small. Our approach is a combination of these schemes, the general-mass variable-flavor-number scheme (GM-VFNS).

The GM-VFNS is a modification of the FFNS, based on the ACOT scheme [6, 7]. The masses of heavy quarks are kept in the parton cross section. To accomodate for large logarithms certain terms are subtracted into the PDFs and FFs so that the parton cross section approaches the ZM-VFNS result in the massless limit. This is not the case when only the logarithms of the mass are subtracted. In the latter case finite terms remain as a difference. Those terms are subtracted as well in the GM-VFNS. The GM-VFNS parton cross section therefore leads to the ZM-VFNS result for high energies but also contains finite mass terms, which improve the result near the mass thresholds.

The GM-VFNS has been worked out for photoproduction [8, 9, 10] and hadroproduction [11, 12, 13, 14]. It has been shown in [15] for electron-positron-annihilation, for other processes [16, 17, 8, 11] and on more general grounds in [18], that the subtraction terms can be generated by convoluting the partonic cross section with a process-independent partonic fragmentation function, which describes the transition from massless to massive quarks. However, in this work we use the more direct method to calculate the subtraction terms by subtracting the massless limit of the partonic cross section of the massive theory from the ZM-VFNS result.

In this work fragmentation functions for the GM-VFNS are extracted as usual from electron-positron-annihilation experiments. More specifically we perform a fit to inclusive production cross sections $\mathrm{d}\sigma/\mathrm{d}x$ for D^0, D^+ and D^{*+} mesons measured by the OPAL collaboration [19, 20]. For the D^{*+} we combine the OPAL data with data of the ALEPH experiment [21]. Both collaborations have collected their data during the Z boson resonance run of the LEP collider, which means that the center-of-mass (CMS) energy $\sqrt{s}$ has been set equal to the mass of the Z boson M_Z. This data has been used before for the extraction of fragmentation functions in [22, 23, 24], but in those works the masses of the heavy quarks have been neglected.

Furthermore we use data from the B factories KEK Asymmetric Eletronic-Positron Collider for B Physics (KEKB) and from the Cornell Electron-Positron Storage Ring (CESR). The measurement and the analysis of the data has been performed by the Belle Collaboration [25] and by the CLEO Collaboration [26]. The CMS energy has been set to 10.5 GeV, which is much closer to the production threshold of D mesons and justifies special attention towards mass effects.

Our final set is a global fit to all the data cited above. This is a test of the DGLAP evolution equations, which describes the change of the FFs when changing the factorization scale, and also a test of the GM-VFNS, which is supposed to work comparably well for small scales near the involved masses and for high scales, where the quark and the hadron masses become negligible. Our fit results have also been published in [27]. Studies incorporating data sets based at these scales based on different approaches have also been done in Refs. [28, 29].

We then show applications for our FFs. First we use the ZM-VFNS differential cross section for deep-inelastic scattering (DIS) from [30] together with our sets of FFs and compare with data from the H1 experiment at the HERA collider [31].

Then we modify the calculation to get predictions for deep-inelastic two-photon-scattering. This process occurs either during the run of an electron-positron-collider like LEP, where one lepton radiates a real photon, while the other takes part in the interaction via a virtual photon just like in DIS. Such processes are found as single-

tagged events - the lepton radiating the virtual photon is detected - in the analysis [32, 33]. The other possibility for this process is an $e\gamma$ mode of an electron-positron-collider, which is planned for the International Linear Collider (ILC) [34].

The necessary modifications look as follows: The proton is replaced by a photon, which has to be done for two contributions. First there is the resolved part, where the photon is treated like a hadron containing quarks and gluons. Here we replace the proton PDFs by the photon PDFs [35] by Aurenche et.al. The second part is the direct part, where we take out the PDFs altogether and use only the gluon. By replacing couplings, color factors and switching off the non-Abelian parts of the cross section, we can use that parton cross section to calculate the scattering of a real photon with a lepton.

We also have to add a convolution of the cross section with the spectrum of the photon. We explore two possibilities for the spectrum for the e^-e^+ mode: One is the Weizsäcker-Williams-approximation [36], which describes the radiation of a quasi-real photon by a lepton. The other spectrum is the effect of beamstrahlung [37], which becomes important for next-generation linear colliders. Here the leptons radiate off photons in the electromagnetic field of the opposing particle bunch.

For the $e\gamma$ mode we require a Compton scattering spectrum. In that mode high-energetic photons are produced by back-scattering a laser beam at one of the lepton beams. The resulting energy spectrum and luminosity have been discussed in [38] and references therein.

Results are then given for the following experiments: We give predictions for the differential cross section for D^* production in single-tagged events for LEP1, where we use the kinematic range of the charm quark analysis [32]. Then we attempt to verify the D^* production cross sections measured at the LEP2 run [33]. Finally we present a variety of differential cross sections for the ILC using all three photon spectra and focussing on D^* production, but also including D^0 and D^+ predictions for comparison.

This work is organised as follows: In chapter 2 we give an introduction to the theory of factorization in perturbative quantum chromo dynamics. We explain how collinear radiation is handled and give an overview over several factorization schemes, before we focus on the General Mass-Variable Flavor Number Scheme (GM-VFNS) which we apply in the rest of this work. In chapter 3 we calculate the semi-inclusive cross section for electron-positron-annihilation with quark masses. Together with the literature result we then deduce the GM-VFNS subtration terms for that process.

In chapter 4 we explain the fitting process including the ISR correction. We then analyse the results of the fits and discuss them together with branching fractions from our theory and from measured values from the literature. Chapter 5 is then dedicated to the applications of these FF sets in different processes. We conclude our work with a summary.

Chapter 2

Theoretical background

2.1 Perturbative QCD

Quantum field theories are the basis of the standard model of elementary particle physics, which is the most successful description of processes at subatomic length scales down to $\sim 10^{-18}$ metres currently available. Most quantities are calculated with the help of perturbation theory, where observables are expanded in a power series of a coupling constant. As a result in electro-weak theory with the coupling constant $\alpha \approx 1/137$ at low energies, the first orders are usually sufficient to reach the precision of measured scattering cross sections.

The situation is more complex in quantum chromodynamics (QCD). The running coupling $\alpha_s(\mu)$ of QCD is getting smaller for higher energies. At low energies we have $\alpha_s > 1$ for low energies, which is the cause for confinement, that means that colored objects like quarks cannot be observed as free particles due to the strong interaction getting larger with a higher distance. Only at scales μ much larger than the QCD scale Λ_{QCD} - meaning several hundred MeV - asymptotic freedom sets in: The coupling α_s becomes much smaller than 1 and perturbation theory becomes feasible again. The simplest model satisfying this characteristics is the parton model [39].

The parton model is based on the assumption that observable hadrons are composed of point-like massless particles called partons. The typical time scale of the interaction between the partons is much larger than the time scale of the scattering of an external particle, say an electron in deep-inelastic scattering on the proton. Therefore for the calculation of the hard scattering process of the electron with one of the hadron's partons, the other partons are regarded as spectator partons and are ignored. The scattering is then calculated from the Feynman tree graphs as a normal process between the external particle and the parton.

The parton model accounts for he inner structure of the hadron in the form of parton distributions, which describe the probability for the external particle to interact with a parton of given sort and a given fraction of the hadron's momentum. For final state hadrons, fragmentation functions describe the probability for each final state parton to hadronise into a particle jet containing a hadron of given sort with a given fraction of the parton's momentum. In both cases the parton's momenta are assumed to be collinear to the respective hadron's momentum.

The components of the parton model have to be combined in the form of a convolution. For example with one parton distribution function (PDF) in the initial state and one fragmentation function (FF) in the final state, a cross section is a convolution of the parton cross section with those two non-perturbative functions

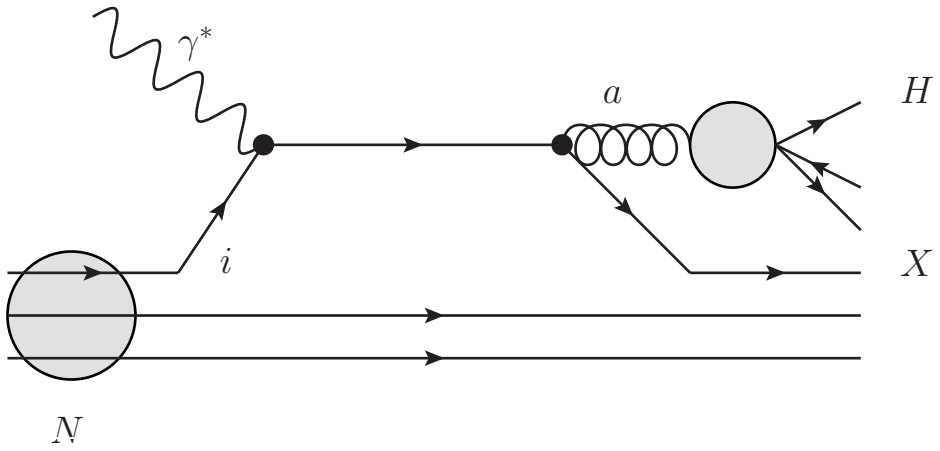

Figure 2.1: Sketch of typical factorization (here: deep inelastic scattering)

[39]:

$$\mathrm{d}\sigma(\tilde{x}, x) = \sum_{i,a} \int_0^1 \mathrm{d}\xi \int_0^1 \mathrm{d}z \; f_{i,N}(\xi)\, \mathrm{d}\hat{\sigma}_{i,a}\left(\tilde{y} = \xi\tilde{x}, y = x/z\right)\, D_a^H(z), \tag{2.1}$$

where $f_{i,N}(\xi)$ is the PDF which gives the probability density for finding a parton i in the initial state hadron N with the fraction ξ of the hadron's normalized momentum fraction $\tilde{x}$ resulting in the normalized initial state parton momentum $\tilde{y}$. Likewise $D_a^H(z)$ is the FF with the probability density for the fragmentation of the final-state parton a with momentum y into the hadron H with the fraction z of the parton's momentum resulting in the hadron momentum x. The normalized momenta run from 0 to the maximum possible value 1, however the situation becomes more complicated when including masses.

The structure is also shown graphically in Fig. 2.1. The PDFs and the FFs are not calculable in perturbation theory and must be extracted from experimental data. However the non-perturbative functions are universal. That means that since the hadronisation process is not sensitive to the particular hard scattering process in short range, the non-perturbative functions can be extracted from data from one kind of scattering experiments and can be used to make predictions for other scattering experiments.

We now take the step to perturbative QCD, which allows for higher orders of the hard-scattering or partonic cross section. The higher orders introduce singularities into the parton cross section. While the ultraviolet (UV) divergencies in the partonic cross section are being taken care of by the usual renormalization procedure, we can also encounter infrared (IR) singularities. Fortunately we can still factorize cross sections into short- and long-range parts [40], which allows us to treat IR singularities and logarithms connected to IR singularities in the partonic cross section in a proper way. In order to prove that factorization is indeed applicable, one has to show that the partonic cross section can be factorized into an IR-safe cross section and subprocesses containing the IR effects, so that they can be absorbed into PDFs and FFs.

As a prize for the higher order corrections we have to introduce a renormalization scale μ and a factorization scales μ_f, which marks the border between short range and long range. In general even seperate factorization scales for initial- and final-states are possible. In this work however we set $\mu = \mu_f$ for convenience and thus

only use one extra scale.

The PDFs $f_{i,N}(\xi, \mu_f)$ and the FFs $D_a^H(z, \mu_f)$ now depend on the factorization scale. This dependence is described by evolution equations, which allow the calculation of the PDFs and FFs, if they are known at an initial scale. Also the parton model interpretation as probability densities is now only approximately true, since the absorption of parts of the partonic cross section introduces ambiguities.

With the introduced scales the cross section in the nth order can be written as

$$\mathrm{d}\sigma^{(n)}(\tilde{x}, x, \mu, \mu_f) = \sum_{i,a} \int_0^1 \mathrm{d}\xi \int_0^1 \mathrm{d}z \; f_{i,N}^{(n)}(\xi) \, \mathrm{d}\hat{\sigma}_{i,a}^{(n)} \left(\tilde{y}, y, \mu, \mu_f\right) \; D_a^{H(n)}(z). \tag{2.2}$$

The number of PDFs per convolution term depends on the number of hadrons in the initial state. Furthermore it depends on the scheme, which PDFs are included in the summation over the parton species. For processes at lower energy scales, not all known quark flavors are taken into account. In our work we use a scheme with a variable flavor number, where the down, up and strange quarks are treated as massless. Therefore we always have the gluon g, the d, u and s quarks plus their respective anti-quarks $\bar{d}$, $\bar{u}$ and $\bar{s}$ as partons and the number of active flavors is $n_f = 3$ for low scales.

We activate additional quark flavors when our scale crosses their masses, so that we have $n_f = 4$ for $m_c < \mu < m_b$ and $n_f = 5$ for $\mu > m_b$. The choice of the heavy quark masses as threshold energies leads to the most simple matching conditions for the PDFs and FFs. Up to $\mathcal{O}(\alpha_s)$, the PDFs and FFs for the relevant number of flavors n_f are equal at $\mu_f = m_c$ and $\mu_f = m_b$ respectively [41]. We use $m_c = 1.5\,\mathrm{GeV}$ and $m_b = 5\,\mathrm{GeV}$ in this work, while the top quark is too heavy to be relevant.

The FFs occur for semi-inclusive processes, where we analyse data of the production of certain hadrons sorts, in our case the charmed D^0, D^+ and the D^{*+} mesons. FFs are not needed when analysing complete jets or total cross sections.

The exact seperation of parton cross section and non-perturbative functions introduces an ambiguity, and so several different factorization schemes are possible analogous to renormalization schemes. One common example is the $\overline{\mathrm{MS}}$-scheme, where the poles and their associated constant terms are subtracted just like in the $\overline{\mathrm{MS}}$ renormalization scheme. But also more finite terms can be absorbed into the non-perturbative functions in other factorization schemes.

As we will show further down, the absorbed IR singularities introduce a logarithmic scale dependence into the non-perturbative functions. These logarithms have to be resummed to all orders, which is done via evolution equations. As mentioned earlier, the evolution equations also allow us to calculate the PDFs and FFs at any given scale once the non-perturbative functions are known at an initial scale. By using the evolution equations in addition to the universality of the non-perturbative functions, we have the required tool to use the non-perturbative functions for predictions in other processes at different scales.

2.2 Mass singularities

Let us take a closer look at the leading IR effects, which can occur in the hard-scattering cross section in perturbative QCD. While the ultra-violet (UV) divergencies are associated with infinite large loop momenta and are taken care of by renormalization, the mass singularities are related to special constellations of finite momenta. They occur in the calculation of the parton cross sections and have to be taken care of by a suitable definition of the factorization scheme, which allows a factorization of the partonic cross section into an IR-safe part and an IR-sensitive

part, which is then absorbed into PDFs and FFs. We shall take a closer look at mass singularities in this section.

There are two types of mass singularities. First there are infrared (IR) singularities, which occur for vanishing masses and lead to logarithmic divergent integrals. In dimensional regularization they manifest themselves in the form of $1/\epsilon$ poles. Typical graphs with IR singularities are virtual corrections, where external particles exchange a massless particle like a gluon or photon.

The source of these divergencies are degenerate final states. A detector cannot distinguish between a certain particle in the final state and the same particle together with a very soft massless particle. Therefore we have to take the latter kind of processes into account. Typically soft particles are radiated off the external particle in the initial or final state and are called real corrections. The infrared singularities cancel when one sums the virtual corrections and the real corrections with the additional particle's phase space being integrated out.

The second type of singularities occur, when massless particles have collinear momenta. Again a detector cannot distinguish between final states with one particle and a final state consisting of two particles. This time the final state is degenerate when both particles fly in the same direction, so that the detector's angular resolution is not sufficient to recognize them as two particles. When the collinear particles have masses $m > 0$, we get logarithms of the mass instead of singularity. Here the mass acts as a natural regulator. However for $\mu \gg m$ these logarithms can spoil the convergence of the perturbation series, so for large scales these logarithms need to be treated similar to the poles in the case of massless particles. The divergence in the case of massless particles is a logarithmically divergent integral just like in the case of IR singularities. However both types of singularities can overlap and lead to more complicated divergencies.

If the radiated particle has a mass m, then this mass acts a regulator for the divergency and the result will contain factors of $\ln m$. However even with this natural regularization, the perturbation theory can again be spoiled since the logarithms occur in the form $\ln(m/E)$, where E is a typical energy in the process. With the possibility of multiple radiation, factors of the form $(\alpha \ln(m/E))^n$ occur to all orders, with these factors being close to one or even higher. In this way the convergence of the perturbation theory breaks down and in order to get meaningful results, we have to resum the collinear singularity.

2.2.1 Splitting functions

We sketch the derivation of the general effect of collinearly radiated gluons from quarks. This will lead to the splitting functions, which are widely used in this topic. The process is looked at in the massless limit, leaving us with logarithms of a regulator.

We assume we have a process with an incoming quark with momentum p with known amplitude $A^{qi\to f}$. Now we take a look of the matrix element, when the incoming quark radiates a gluon with momentum k as depicted in Fig.2.2(a). We are only interested in the collinear limit, which simplifies the calculation. The matrix element of the full process is then

$$\mathcal{M}_{\kappa\lambda}^{qi\to gf}(p,k,p_j) = \bar{A}^{qi\to f}(p-k,p_j)\frac{\mathrm{i}(\not{p}-\not{k}+m)}{(p-k)^2-m^2+\mathrm{i}\epsilon}[\mathrm{i}g_s\not{\epsilon}^*(k,\lambda)]u(p,\kappa). \quad (2.3)$$

The p_j are the remaining occuring momenta of external particles beside p, m is the mass of the quark, g_s is the strong coupling, $\epsilon(k,\lambda)$ is the polarization vector of the emitted gluon with polarization λ and $u(p,\kappa)$ is the spinor of the incoming quark with spin κ. We omit the color factor in the expression above. The added

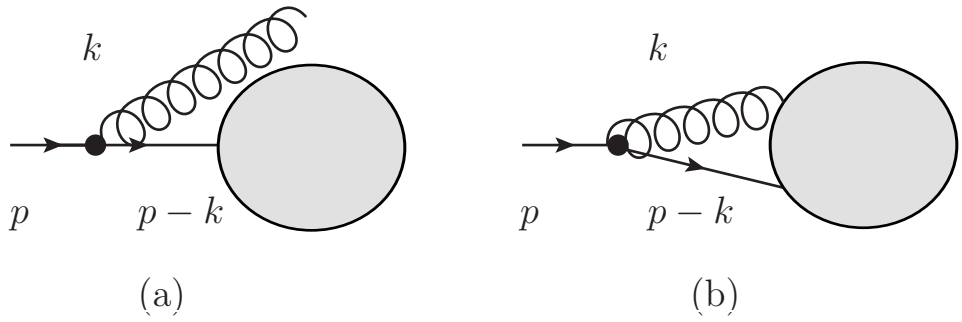

Figure 2.2: Graph for collinear emission: (a) real, (b) virtual

vertex contributes a color group generator generator T^a, which has to be multiplied with the color group factors in $A^{qi\to f}$. The new factors in the matrix element are the propagator of the quark after the emission of the gluon and the vertex factor together with the polarization vector of the emitted gluon.

The four-momenta of the external quark p, of the emitted gluon k and of the internal quark p' can be parametrized as

$$\begin{aligned} p^\mu &= (E,0,0,E), \\ k^\mu &= \left((1-z)E + \frac{\mathbf{k}_\perp^2}{4(1-z)E}, 0, 0, (1-z)E - \frac{\mathbf{k}_\perp^2}{4(1-z)E}\right) + k_\perp^\mu, \\ p'^\mu &= \left(xE - \frac{\mathbf{k}_\perp^2}{4(1-z)E}, 0, 0, xE + \frac{\mathbf{k}_\perp^2}{4(1-z)E}\right) - k_\perp^\mu, \\ k_\perp^\mu &= (0, \mathbf{k}_\perp) = (0, |\mathbf{k}_\perp|\cos\phi, |\mathbf{k}_\perp|\sin\phi, 0), \end{aligned} \tag{2.4}$$

and obey

$$p^2 = 0, \quad k^2 = 0, \quad p'^2 = -\frac{\mathbf{k}_\perp^2}{1-z}. \tag{2.5}$$

The variable z determines the fraction of the energy, that the quark retains after the emission of the gluon. The soft-photon limit corresponds to $z \to 1$. Collinear gluons are emitted for $|\mathbf{k}_\perp| \ll (1-z)E$. Therefore $|\mathbf{k}_\perp|$ - also known as acollinearity - serves as the regulator for the collinear singularities. Using expansions in $|\mathbf{k}_\perp|$ for simplifications, the squared matrix element summed over all gluon polarization can be written as

$$\sum_{\lambda=\pm} |\mathcal{M}_{\kappa\lambda}^{qi\to gf}|^2 = 2C_F\, g_s^2 \frac{1-z}{z\mathbf{k}_\perp^2}\frac{1+z^2}{1-z}|\mathcal{M}_\kappa^{qi\to f}|^2 + \mathcal{O}\left(|\mathbf{k}_\perp|^{-1}\right). \tag{2.6}$$

The color factor C_F stems from the extension of the color group generators. Let $\mathrm{Tr}A_F$ be the color factor of the cross section without gluon emission, where A_F is a product of SU(3) generators. Then the color factor with gluon emission is

$$\sum_a \mathrm{Tr}(T_F^a A_F T_F^a) = \sum_a \mathrm{Tr}(A_F T_F^a T_F^a) = C_F \mathrm{Tr}(A_F). \tag{2.7}$$

For the cross section we have to integrate out the photon phase space. It can be written as:

$$\frac{\mathrm{d}^3k}{(2\pi)^3 2E_k} = \frac{\mathrm{d}z\,\mathrm{d}\phi\,\mathrm{d}\mathbf{k}_\perp^2}{4(2\pi)^3(1-z)} + \mathcal{O}\left(|\mathbf{k}_\perp|^2.\right) \tag{2.8}$$

After integrating over ϕ and $\mathbf{k}_\perp^2$ the leading logarithm term is

$$\mathrm{d}\sigma_\kappa^{qi\to gf}(p,p_j) = \frac{\alpha}{2\pi}\ln\left(\frac{\mathbf{k}_{\perp,\max}^2}{\mathbf{k}_{\perp,\min}^2}\right) C_F \int_0^1 \mathrm{d}z \frac{1+z^2}{1-z}\mathrm{d}\sigma_\kappa^{qi\to f}(zp,p_j) + \mathcal{O}\left(|\mathbf{k}_\perp|^{1/2}\right). \tag{2.9}$$

The upper limit of $|\mathbf{k}_\perp|$ is in the dimension of the process scale μ. The lower limit is in the dimension of the regulator. When using the quark mass m as a regulator instead of the acollinearity, the form of the leading logarithm term doesn't change [53]. Thus the leading logarithm can also be written as

$$\mathrm{d}\sigma_{\mathrm{LL},\kappa}^{qi\to gf}(p,p_j) = \frac{\alpha}{2\pi}\ln\left(\frac{\mu^2}{m^2}\right) C_F \int_0^1 \mathrm{d}z \frac{1+z^2}{1-z}\mathrm{d}\sigma_\kappa^{qi\to f}(zp,p_j) + \mathcal{O}\left(|\mathbf{k}_\perp|^{1/2}\right). \tag{2.10}$$

We find the IR singularity in the form of the $1-z$ in the denominator.

We have to include the possibility of virtual collinear gluons. In this case the emitted gluon takes part in the process and acts as an additional incoming particle (Fig.2.2(b)). The possibility of virtual collinear particles leads to the new matrix element (in Feynman gauge):

$$\begin{aligned}\mathcal{M}_{\mathrm{virt},\kappa}^{qi\to f}(p,p_j) \quad &= \quad \int \frac{\mathrm{d}^4k}{(2\pi)^4} \\ &\bar{A}_\mu^{egi\to f}(p-k,k,p_j)\frac{\mathrm{i}(\not{p}-\not{k}+m)}{(p-k)^2-m^2+\mathrm{i}\epsilon}\mathrm{i}g_s\gamma_\nu u(p,\kappa)\frac{-\mathrm{i}g^{\mu\nu}}{k^2+\mathrm{i}\epsilon}.\end{aligned} \tag{2.11}$$

Here we introduce propagators for the now virtual quark and the gluon. The gluon's momentum acts as the loop momentum and is integrated out.

This leads, together with the quark-field renormalization and the use of a Ward identity to replace the amplitude with extra gluon in the initial state by one without that gluon, to the cross section

$$\mathrm{d}\sigma_{\mathrm{virt},\kappa}^{qi\to f}(p,p_j) = -\frac{\alpha}{2\pi}\ln\left(\frac{\mu^2}{m^2}\right) C_F \int_0^1 \mathrm{d}z \frac{1+z^2}{1-z}\mathrm{d}\sigma_\kappa^{qi\to f}(p,p_j) + \mathcal{O}\left(|\mathbf{k}_\perp|^{1/2}\right). \tag{2.12}$$

When we sum the leading logarithm terms of real and virtual collinear emission, the soft singularity at $z=1$ cancels. The sum is best written in the form of a plus-distribution, which is defined by:

$$\int_z^1 \mathrm{d}y \left[\frac{g(y)}{1-y}\right]_+ f(y) = \int_z^1 \mathrm{d}y \frac{(f(y)-f(1))g(y)}{1-y} - f(1)\int_0^z \mathrm{d}y \frac{g(y)}{1-y}. \tag{2.13}$$

It is IR-safe by construction.

The sum is

$$\mathrm{d}\sigma_{\mathrm{LL},\kappa}^{qi\to gf}(p,p_j) = \frac{\alpha}{2\pi}\ln\left(\frac{\mu^2}{m^2}\right) C_F \int_0^1 \mathrm{d}z \left(\frac{1+z^2}{1-z}\right)_+ \mathrm{d}\sigma_\kappa^{qi\to f}(zp,p_j). \tag{2.14}$$

This motivates the definition of the quark-quark splitting function in lowest order:

$$P_{qq}^{(0)}(z) = C_F\left(\frac{1+z^2}{1-z}\right)_+. \tag{2.15}$$

It is related to the probability of finding a collinear quark with momentum fraction z in the original quark. There are more splitting function in lowest order

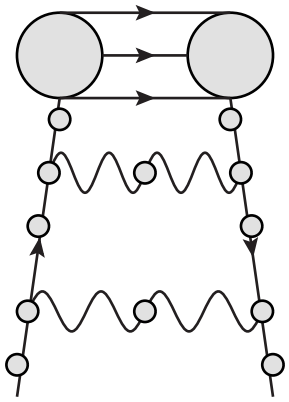

Figure 2.3: Cut ladder diagram which provides leading mass singularities

QCD, which describe probabilities of finding a gluon in a quark, a quark in a gluon and a gluon in a gluon respectively [42]:

$$P_{qg}^{(0)}(z) = T_F(z^2+(1-z)^2), \tag{2.16}$$

$$P_{gq}^{(0)}(z) = C_F\frac{1+(1-z)^2}{z},$$

$$P_{gg}^{(0)}(z) = 2C_A\left(z\left(\frac{1}{1-z}\right)_+ + \frac{1-z}{z} + z(1-z)\right) + \left(\frac{11}{6}C_A - \frac{2}{3}N_f T_F\right)\delta(1-z). \tag{2.17}$$

The occuring color group factors are $T_F = 1/2$ and $C_A = 3$. In addition the gluon-gluon splitting function contains the number of active flavors n_f.

The splitting functions are closely related to the distribution functions, which describe the probability of finding partons with certain momentum inside other partons. This means that the latter parton has to emit a collinear parton of the first sort. These functions are similar to the hadronic PDFs, but unlike them they are calculable in perturbation theory. The relations are:

$$f_{q,q}(z,\mu^2) = f_{\bar{q},\bar{q}}(z,\mu^2) = \delta(1-z) + \frac{\alpha}{2\pi}\ln\left(\frac{\mu^2}{m^2}\right)P_{qq}^{(0)}(z), \tag{2.18}$$

$$f_{q,\bar{q}}(z,\mu^2) = f_{\bar{q},q}(z,\mu^2) = 0,$$

$$f_{g,q}(z,\mu^2) = f_{g,\bar{q}}(z,\mu^2) = \frac{\alpha}{2\pi}\ln\left(\frac{\mu^2}{m^2}\right)P_{gq}^{(0)}(z),$$

$$f_{g,g}(z,\mu^2) = \delta(1-z) + \frac{\alpha}{2\pi}\ln\left(\frac{\mu^2}{m^2}\right)P_{gg}^{(0)}(z),$$

$$f_{q,g}(z,\mu^2) = f_{\bar{q},g}(z,\mu^2) = \frac{\alpha}{2\pi}\ln\left(\frac{\mu^2}{m^2}\right)P_{qg}^{(0)}(z).$$

Multiple splittings allow more complicated graphs, especially through the non-Abelian property of gluons emitting more gluons. However it has been examined in the literature [43], that the leading contribution comes from ladder graphs as

depicted in Fig.2.3. Here we see a cut-diagram which represents $\mathcal{M}\mathcal{M}^*$. The lines which are cut by a vertical line in the middle are on-shell, real particles. The interesting graphs are the ones, where all propagators are emitted collinearly, where the vertices and the propagators may be dressed.

We therefore take a look at graphs for illustration, where the incoming quark emits two collinear gluons. The leading contribution comes from the case, where the first emitted gluon has a small acollinerity. Then the quark is still close to its mass-shell and the second emission can give a similarly enhanced contribution. The integration over the kinematic region, which gives the leading contribution, leads to a logarithm squared:

$$\left(\frac{\alpha}{2\pi}\right)^2 \int_{m^2}^{\mu^2} \frac{\mathrm{d}\mathbf{k}_{\perp,2}^2}{\mathbf{k}_{\perp,2}^2} \int_{m^2}^{|\mathbf{k}_{\perp,2}|^2} \frac{\mathrm{d}\mathbf{k}_{\perp,1}^2}{\mathbf{k}_{\perp,1}^2} = \frac{1}{2}\left(\frac{\alpha}{2\pi}\ln\left(\frac{\mu^2}{m^2}\right)\right)^2. \tag{2.19}$$

In general, the leading logarithm contribution for the emission of n gluons is proportional to

$$\frac{1}{n!}\left(\frac{\alpha_s}{2\pi}\ln\left(\frac{\mu^2}{m^2}\right)\right)^n. \tag{2.20}$$

2.3 Evolution equations

With the partonic distribution functions (2.18), we can derive the μ^2-dependence of the FFs and PDFs. If a distribution function $f(x,\mu^2)$ is given for a scale μ, then the function $f(x,\mu^2+\mathrm{d}\mu^2)$ must take into account the possibility of an additional emission of a parton with transverse momentum $\mu^2 < \mathbf{k}_\perp^2 < \mu^2+\mathrm{d}\mu^2$. The probability to split off a parton that carries away the part $1-x$ of the energy is

$$\frac{\alpha_s}{2\pi}\frac{\mathrm{d}\mathbf{k}_\perp^2}{\mathbf{k}_\perp^2}P(x) \tag{2.21}$$

and thus

$$\begin{aligned} f(x,\mu^2+\mathrm{d}\mu^2) &= f(x,\mu^2) + \int_0^1 \mathrm{d}y \int_0^1 \mathrm{d}z\,\delta(x-yz) \\ &\quad \times\frac{\alpha_s}{2\pi}\frac{\mathrm{d}\mu^2}{\mu^2}P(y)f(z,\mu^2) \\ &= f(x,\mu^2) + \frac{\mathrm{d}\mu^2}{\mu^2}\frac{\alpha_s}{2\pi}\int_x^1 \frac{\mathrm{d}z}{z}P\left(\frac{x}{z}\right)f(z,\mu^2). \end{aligned} \tag{2.22}$$

This leads to an integro-differential equation

$$\frac{\partial}{\partial(\ln\mu^2)}f(x,\mu^2) = \frac{\alpha_s}{2\pi}\int_x^1 \frac{\mathrm{d}z}{z}P\left(\frac{x}{z}\right)f(z,\mu^2). \tag{2.23}$$

This is an evolution equation, which describes the scale dependence of a distribution function. The distribution function must be known at an initial scale μ_0. For QCD all partons must be considered. Through splitting of gluons off quarks and the production of collinear quark-antiquark pairs from gluons, all sorts of partons mix. The result is a system of coupled integro-differential equations, known as the DGLAP equations [44, 42, 45]. For fragmentation functions they can be written as:

$$\frac{\mathrm{d}}{\mathrm{d}\ln\mu_f^2}D_a(x,\mu_f) = \frac{\alpha_s(\mu)}{2\pi}\sum_b \int_x^1 \frac{\mathrm{d}z}{z}P_{a\to b}^T(z,\alpha_s(\mu))D_b\left(\frac{x}{z},\mu_f\right). \tag{2.24}$$

The T at the splitting function stands for time-like splitting functions in contrast to the space-like splitting functions, that are used for the PDFs. We have only presented the LO splitting functions in equations (2.15) and (2.16), where time-like and space-like splitting functions are equal. For the evolution in NLO, we need the NLO splitting functions, which are of $\mathcal{O}\left(\alpha_s^2\right)$. They can be found in [46, 47].

We like to point out some properties of this set of coupled DGLAP equations. The summation over the partons only includes the active flavors. Therefore in the case of a scheme with a variable number of active flavors, the right side of the equation gets new terms, when the factorization scale μ_f crosses the flavor thresholds (m_c and m_b in this work).

In our scheme we assume that charmed mesons are only directly produced via the hadronisation of c, $\bar{c}$, b and $\bar{b}$ quarks. Therefore the FFs of the light quarks d, u and s, their respective anti-quarks and of the gluon are set to zero at the initial scale. Only when the c quark and the b quark become active flavors, the former FFs gain values through the coupled DGLAP equations. The light quarks can fragment into heavy hadrons by splitting off a collinear heavy quark which then fragments into the hadron of interest.

2.4 Factorization schemes

We now turn our attention to the various factorization schemes which have been used in the literature. By explaining the advantages and disadvantages we motivate our scheme. We use heavy quark production in deep-inelastic scattering as an example, which is also used in more detail in [7]. The two most important contributions are shown in Fig.2.4. Graph (a) shows quark-scattering, graph (b) depicts gluon-fusion. Gluon-fusion is one order higher in power of α_s, but quark-scattering requires a heavy quark in the initial state, which is only present as sea-quark in protons. Therefore we regard both processes as effectively being of the same order.

2.4.1 ZM-VFNS

The first scheme is the *zero-mass variable-flavor-number scheme* (ZM-VFNS). All quarks are treated as massless particles. In order to account for the masses of the heavy quarks, the number of active flavors varies with the the factorization scale. Only for scales higher than the respective flavor thresholds, the quark is active as a parton. For the transition scales, matching equation between the non-perturbative functions and the couplings have to be used.

In the ZM-VFNS the collinear singularities are encountered in the form of singularities in the parton cross section, e.g. $1/\epsilon$ poles in dimensional regularization. These poles are absorbed into the PDFs and FFs. For the absorption a scheme has to be chosen similar to renormalization. In the following we assume dimensional regularization with the $\overline{\text{MS}}$ scheme, where only the pole and with the pole associated constant terms are subtracted from the parton cross section.

Since no masses enter the cross section, no large logarithms $\ln(\mu^2/m^2)$ can occur. This scheme works best for high energy scales, where $m_Q = 0$ is a good approximation. But naturally its accuracy suffers at lower scales just above the production thresholds. Here the production cross section is typically overestimated due to the heavy quark being in full effect without taking its threshold behaviour into account.

In Fig.2.4 the quark-scattering graph (a) is only present for $\mu_f > m_Q$. Below that scale the leading order of the parton cross section consists only of the gluon-fusion process (b).

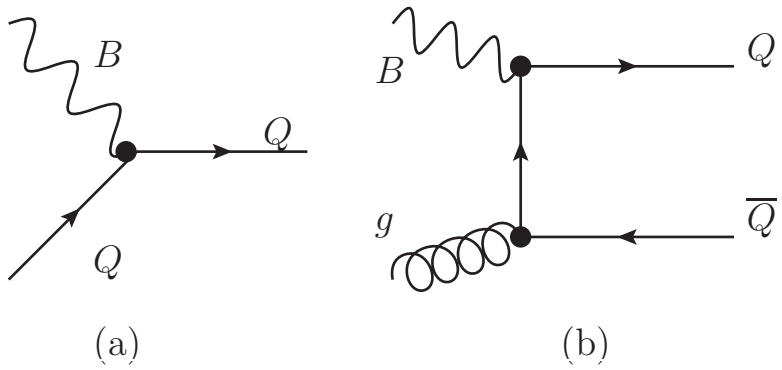

Figure 2.4: Dominant processes for heavy quark production (omitting antiquark-production): (a) quark-scattering, (b) gluon-fusion

2.4.2 FFNS

In the *fixed-flavor-number scheme* (FFNS), the number of active partons in the initial state is kept fixed. The heavy quark only occurs in final states, but its mass is kept as a large scale in the partonic cross section. As a consequence logarithms of the form $\ln(\mu^2/m^2)$ occur in the parton cross section, which are not subtracted. In our example only the gluon-fusion Fig.2.4(b) enters the parton cross section.

This logarithms only spoil the convergence of the perturbation series when they become large. Therefore this scheme works well in the kinematic regime where the logarithms are small, hence for $\mu_f \sim m_Q$. Only for $\mu_f \gg m$ the convergence breaks down and the scheme fails.

2.4.3 FONLL

In the *fixed-order next-to-leading-logartihm* approach, the ZM-VFNS and the FFNS are superimposed with a one-parameter-function. Near the mass threshold the FFNS dominates, while for high energies the results of the ZM-VFNS are obtained.

While this scheme has the desired property to match the best suited scheme at their respectice scales, the parameter is not fixed by the theory and the mixing happens arbitrary. While the FFNS works over a larger scale than the ZM-VFNS and the FFNS alone, the results in the range where both contributions are sizable cannot be expected to give accurate predictions.

2.5 The ACOT scheme

The ACOT scheme, named after Aivazis, Collins, Olness and Tung [7], combines the ZM-VFNS and the FFNS on a more solid theoretical fundament. The scheme is presented and its factorization proven for heavy quark production in deep-inelastic scattering. We will go over the most important points from [7].

First the heavy masses are kept in the structure functions, so logarithms of the multiple scales have to be expected. The basic assumption is, that the structure functions can be factorized into IR-safe structure functions and partonic distribution functions, which contain the logarithms coming from collinear singularities. The factorization formula is applied to the structure function on the parton level, where $\otimes$ denotes a multiplicative convolution:

$$\omega_{Bg}^{\lambda(1)} = \sum_a f_g^a \otimes \hat{\omega}_{Ba}^{\lambda}. \tag{2.25}$$

Here the structure function $\omega_{Bg}^{\lambda(1)}$ in order $\mathcal{O}\left(\alpha_s^1\right)$ with helicity λ for the scattering of a virtual boson B and a gluon g is factorized into a respective IR-safe strucure function $\hat{\omega}_{Ba}^{\lambda}$ and a partonic density function f_g^a for the probability of finding a collinear parton a in the gluon g. We remind the reader that the partonic density functions (2.18) are calculable in perturbation theory unlike the hadronic PDFs.

In order to examine the factors order by order, we write

$$\begin{aligned} f_g^a &= f_g^{a(0)} + f_g^{a(1)}, \\ \hat{\omega}_{Ba}^{\lambda} &= \hat{\omega}_{Ba}^{\lambda(0)} + \hat{\omega}_{Ba}^{\lambda(1)}, \\ \omega_{Ba}^{\lambda} &= \omega_{Ba}^{\lambda(0)} + \omega_{Ba}^{\lambda(1)}, \end{aligned} \tag{2.26}$$

where the superscript denotes the order in α_s.

This leads to

$$\begin{aligned} \omega_{Bg}^{\lambda(1)} &= \sum_a (f_g^{a(0)} \otimes \hat{\omega}_{Ba}^{\lambda(1)} + f_g^{a(1)} \otimes \hat{\omega}_{Ba}^{\lambda(0)}) \\ &= \hat{\omega}_{Ba}^{\lambda(1)} + f_g^{Q(1)} \otimes \omega_{BQ}^{\lambda(0)}, \end{aligned} \tag{2.27}$$

using $f_b^{a(0)}(\xi) = \delta_b^a \delta(1-\xi)$, $\hat{\omega}_{Ba}^{\lambda(0)} = \omega_{Ba}^{\lambda(0)}$ and $\omega_{Bg}^{\lambda(0)} = 0$.

Inverting this result gives the IR-safe structure function in terms of the calculated structure function and a subtraction term:

$$\hat{\omega}_{Bg}^{\lambda(1)} = \omega_{Bg}^{\lambda(1)} - f_g^{Q(1)} \otimes \omega_{BQ}^{\lambda(0)}. \tag{2.28}$$

For the physical structure function follows

$$W_{BN}^{\lambda} = f_N^Q \otimes \omega_{BQ}^{\lambda(0)} - \sum_i f_N^g \otimes f_g^{Q_i(0)} \otimes \omega_{BQ_i}^{\lambda(0)} + f_N^g \otimes \omega_{Bg}^{\lambda(1)} + \mathcal{O}\left(\alpha_s^2\right), \tag{2.29}$$

where the term of $\mathcal{O}\left(\alpha_s^1\right)$ with the heavy quark-PDF is omitted, because it is supressed in comparison to the other terms of the same order. It is shown in [7] by explicit calculation that the resulting structure function is IR-safe and converges to the ZM-VFNS result in the massless limit.

The physical interpretation of the subtraction term in the middle is, that it corrects for double counting of the collinear singularity that occurs, when the incoming gluon is collinear to the inner quark. This case is already resummed in the quark-scattering process, where the incoming quark can be split off from a gluon in the evolution equations. With the masses in the structure functions, it occurs again in the gluon-fusion graph as a potentially large logarithm.

The proof of the ACOT scheme is valid for any specific scheme that contains the same leading infrared sensitive terms.

2.6 General mass-variable flavor number scheme

We use the *general mass-variable flavor number scheme* (GM-VFNS) in the following chapters. The GM-VFNS is based on the proof of the ACOT scheme. However the scheme is defined by construction of the subtraction terms. Just like in the ACOT scheme the subtraction term will lead to a partonic cross section that is IR-safe and converges to the ZM-VFNS result in the massless limit. The latter goal is not achieved by a simple subtraction of the logarithm terms. The construction of the GM-VFNS leads to a natural transition to the ZM-VFNS at high energies and

contains finite mass terms in the cross section to give a good description near mass thresholds.

To achieve this goal, the parton cross sections in the GM-VFNS are constructed in the following way: We calculate the parton cross sections $\mathrm{d}\sigma_{m_Q}$ similar to the FFNS with the heavy quark's mass as an extra scale. This leads to the dreaded logarithms of the form $\ln(\mu^2/m_Q^2)$. Furthermore the cross section differs by finite terms from the ZM-VFNS version.

Now we take the massless limit of the FFNS cross section where possible. The logarithms of the mass are kept, since they are singular in the limit. Terms proportional to powers of the mass however disappear. Now we subtract the ZM-VFNS cross section from our result. The result of this procedure are our subtraction terms. They contain the logarithms and finite terms, which only occur in the FFNS cross section. So our subtraction terms are defined through:

$$\mathrm{d}\sigma_{\mathrm{Sub}} = \lim_{m_Q \to 0} \mathrm{d}\sigma_{m_Q} - \mathrm{d}\sigma_{\mathrm{ZM}}. \tag{2.30}$$

We then calculate the difference between the cross section with masses and the subtraction terms and receive the GM-VFNS cross section:

$$\mathrm{d}\sigma_{\mathrm{GM}} = \mathrm{d}\sigma_{m_Q} - \mathrm{d}\sigma_{\mathrm{Sub}}. \tag{2.31}$$

In this way the logarithms of the masses are absorbed into the non-perturbative functions together with the finite terms, that don't occur in the ZM-VFNS cross section. However the GM-VFNS cross section still contains terms which depend on the mass and disappear in the massless limit. These finite mass terms are supposed to improve the description of cross sections at lower scales and intermediate scales. The cross section contains the phase space with quark masses and therefore reproduces a correct threshold behavior, while the ZM-VFNS switches from a infinitely massive charm quark to a massless charm quark at the threshold scale.

We want to note that the subtraction terms, constructed in this way, may agree with subtraction terms calculated from similar approaches. In [12] it is shown, that the definition in (2.30) and (2.31) is equivalent to the convolution of the massless cross section with calculable partonic fragmentation functions, which describe the transition from a massless quark to a massive one. However there is no universal proof yet. The equivalency has been shown for some scattering processes.

Chapter 3

Heavy hadron production in electron-positron annihilation

The process of inclusive heavy hadron production in electron-positron annihilation is well suited for the extraction of fragmentation functions from experimental data. One reason is that e^+e^- processes have in general less contributions by background processes compared to hadron collisions, the other reason is that we don't have to deal with the uncertainty introduced by parton density functions.

Therefore we study the process

$$e^+ + e^- \to (\gamma, Z) \to H + X, \tag{3.1}$$

where X stands for the content of the jets that are produced together with the hadron H, which is observed. All kinematic variables of X are integrated out. Also the scattering angles of H are integrated out. We keep the scaling variable $x = 2(p_H \cdot q)/q^2$, where p_H is the four-momentum of the hadron and q the four-momentum of the intermediate gauge boson γ or Z. In the CMS, $x = 2E/\sqrt{s}$ measures the energy E of the hadron in units of the beam energy. The aim of the calculation is the semi-inclusive cross section $\mathrm{d}\sigma/\mathrm{d}x$.

To complete our definitions, we call the four-momenta of the incoming electron and positron l_1 and l_2 respectively and the four-momenta of the outgoing quark and anti-quark p_1 and p_2. We refer to the angle of the outgoing hadron toward the beam axis as θ and we use the Mandelstam-variables:

$$s = (l_1 + l_2)^2, \quad t = (l_1 - p_1)^2, \quad u = (l_1 - p_2)^2. \tag{3.2}$$

3.1 Structure of the cross section

For unpolarized beams and fixed $\sqrt{s}$ the differential cross section can only depend on x and θ. A tensor analysis shows that, since the virtual boson has spin one, the cross section can be seperated into three polarization terms [15, 5]:

$$\frac{\mathrm{d}^2\sigma}{\mathrm{d}x\,\mathrm{d}\cos\theta} = \frac{3}{8}(1+\cos^2\theta)\frac{\mathrm{d}\sigma^T}{\mathrm{d}x} + \frac{3}{4}\sin^2\theta\frac{\mathrm{d}\sigma^L}{\mathrm{d}x} + \frac{3}{4}\cos\theta\frac{\mathrm{d}\sigma^A}{\mathrm{d}x}. \tag{3.3}$$

The three terms on the right-hand side stand for the transversal, the longitudinal and the asymmetric contribution, where the first two are associated with the polarization states of the boson with respect to the direction of the hadron H. The

asymmetric term stems from the parity-violating interference term, which contains the vector coupling from the intermediate photon and Z boson times the axial coupling from the Z boson. The normalization is chosen so that equation

$$\frac{\mathrm{d}\sigma}{\mathrm{d}x} = \int_{-1}^{+1} \mathrm{d}\cos\theta \frac{\mathrm{d}^2\sigma}{\mathrm{d}x\,\mathrm{d}\cos\theta} = \frac{\mathrm{d}\sigma^T}{\mathrm{d}x} + \frac{\mathrm{d}\sigma^L}{\mathrm{d}x} \tag{3.4}$$

is fulfilled. The asymmetric contribution disappears when integrating out $\cos\theta$, so we only have to deal with $\mathrm{d}\sigma^T/\mathrm{d}x$ and $\mathrm{d}\sigma^L/\mathrm{d}x$, which we will refer to as $\mathrm{d}\sigma^P/\mathrm{d}x$ with $P = T, L$.

In the parton model each component $\mathrm{d}\sigma^P/\mathrm{d}x$ can be written up to power corrections as a sum of convolutions of partonic cross sections $\mathrm{d}\sigma_a^P(y,\mu,\mu_f)/\mathrm{d}y$ with fragmentation functions $D_a^H(z,\mu_f)$, where the a stands for one of the partons (g,u,$\bar{u}$,...,b,$\bar{b}$) and P for the transversal or longitudinal polarization. The renormalization and factorization scales are given by μ and μ_f respectively, however we set $\mu = \mu_f$ in this work. y is defined in analogy to x as $2(p_a \cdot q)/q^2$, where p_a is the four-momentum of parton a and $z = x/y$. In the CMS z is the fraction of the energy passed on from parton a to the hadron H, it should be noted that in the massive case z could be defined in different ways. With these variables the convolution can be written as:

$$\frac{\mathrm{d}\sigma^P}{\mathrm{d}x}(x,s) = \sum_a \int_{y_{\min}}^{y_{\max}} \frac{\mathrm{d}y}{y} \frac{\mathrm{d}\sigma_a^P}{\mathrm{d}y}(y,\mu,\mu_f) D_a\left(\frac{x}{y},\mu_f\right). \tag{3.5}$$

For the massless case the integration limits are $y_{\min} = x$ and $y_{\max} = 1$. Since we include the charm quark mass $m_c = 1.5\,\mathrm{GeV}$, the bottom quark mass $m_b = 5.0\,\mathrm{GeV}$ and the hadron mass m_H, these limits become more complicated due to kinematic constraints. If we calculate the partonic subprocess for the production of a heavy quark with mass m_a and $\rho_a = 4m_a^2/s$, the boundaries are $y_{\min} = \max(x, \sqrt{\rho_a})$ and $y_{\max} = 1$ and x must be in the range of $\sqrt{\rho_H} \leq x < 1$. If we look at the production of a gluon which is accompanied by a pair of a heavy quark and a heavy anti-quark both with mass m_a, then the limits are $y_{\min} = x$ and $y_{\max} = 1 - \rho_a$ and $\sqrt{\rho_H} \leq x < 1 - \rho_a$.

In order to apply the GM-VFNS we need the expressions for all partonic subprocesses with the masses of heavy quarks as well as in the ZM-VFNS, where the masses are neglected. On the following pages the semi-inclusive cross section for the production of a heavy quark with the QCD corrections of $\mathcal{O}(\alpha_s)$ is calculated. We compare the result and its massless limit with the formulas in refs.[15, 5]. The remaining expressions for the production of a fragmenting gluon together with a heavy quark-antiquark-pair and for all relevant ZM-VFNS subprocesses are also taken from those references.

3.2 Cross section for heavy quark production

Our goal is to calculate the semi-inclusive cross section $\mathrm{d}\sigma/\mathrm{d}y$ of the process

$$e^-(l_1) + e^+(l_2) \to \gamma^*/Z^*(q) \to q(p_1) + \bar{q}(p_2). \tag{3.6}$$

In NLO we have to calculate the virtual corrections to the LO process and - as the real corrections - the LO cross section of the process

$$e^-(l_1) + e^+(l_2) \to \gamma^*/Z^*(q) \to q(p_1) + \bar{q}(p_2) + g(p_3), \tag{3.7}$$

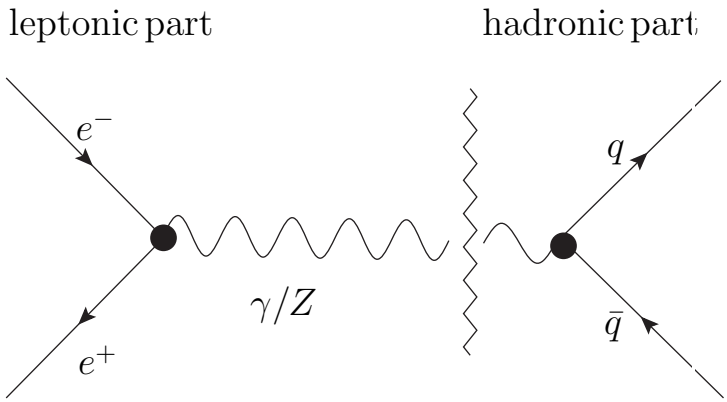

Figure 3.1: Sketch of the factorization of the $e^+e^- \to q\bar{q}$ process into leptonic and hadronic part in the form of a Feynman graph

where the variables in brackets indicate the names of the associated four-momenta of the particles. We will integrate out the gluon's four-momentum p_3, after which we can sum both contributions to cancel the divergencies associated with the radiation of a soft gluon. We apply dimensional regularization with $D = 4 + \epsilon$ dimensions for singularities and use on-shell-renormalization for the UV divergencies. The infrared divergencies and other terms will be subtracted according to the rules of the GM-VFNS.

In general the differential cross section for the scattering of two antiparallel particles with negligible mass is calculated from

$$\mathrm{d}\sigma = \frac{1}{4\sqrt{(l_1 l_2)^2}} |\mathcal{M}|^2 \mathrm{d}P, \tag{3.8}$$

where $1/(4\sqrt{(l_1 l_2)^2}) = 1/(2s)$ is the flux factor of the incoming leptons, $\mathcal{M}$ is the matrix element of the scattering process and $\mathrm{d}P$ is the phase space of the outgoing particles. In our case $|\mathcal{M}|^2$ contains single poles in ϵ. Therefore we have to take terms up to $\mathcal{O}(\epsilon)$ into account.

3.2.1 Factorization into lepton and hadron tensor

We factorize the cross section into a leptonic and a hadronic tensor. Due to the axial part of the Z boson coupling, we have to factorize the vector-part, the axial-part and the interference term seperately:

$$\frac{\mathrm{d}\sigma}{\mathrm{d}y} = \hat{L}_{VV\mu\nu}\hat{H}^{\mu\nu}_{VV} + 2\hat{L}_{AV\mu\nu}\hat{H}^{\mu\nu}_{AV} + \hat{L}_{AA\mu\nu}\hat{H}^{\mu\nu}_{AA}. \tag{3.9}$$

The indices V and A stand for vector- and axial-coupling respectively. The interference term in the middle on the right-hand-side leads leads to the asymmetric term due to a single γ_5 matrix and vanishes after the integration over $\cos\theta$. Therefore we will ignore it from now on.

We will need the following effective charges for the vector- and the axial-part:

$$\begin{aligned} V^2_{q_i} &= e^2_{q_i} + v_e e_{q_i} v_{q_i} \rho_1(s) + (v_e^2 + a_e^2) v^2_{q_i} \rho_2(s), \\ A^2_{q_i} &= (v_e^2 + a_e^2) a^2_{q_i} \rho_2(s) \end{aligned} \tag{3.10}$$

with the electro-weak couplings $v_{q_i} = (T_{3q_i} - 2e_f \sin^2\theta_W)/(2\sin\theta_W\cos\theta_W)$ and $a_f = T_{3q_i}/(2\sin\theta_W\cos\theta_W)$ of the quark q_i. The quark's fractional electric charge

is given by e_{q_i}, its third component of weak isospin to the Z boson by T_{3q_i}, and we use the propagator functions

$$\begin{aligned} \rho_1(s) &= \frac{s(s-m_Z^2)}{(s-m_Z^2)^2+m_Z^2\Gamma_Z^2}, \\ \rho_2(s) &= \frac{s^2}{(s-m_Z^2)^2+m_Z^2\Gamma_Z^2}. \end{aligned} \tag{3.11}$$

θ_W is the weak mixing angle, m_Z the mass and Γ_Z the total decay width of the Z boson.

With these charges we write

$$\frac{\mathrm{d}\sigma}{\mathrm{d}y} = V_{q_i}^2 L_{\mu\nu} H_{VV}^{\mu\nu} + A_{q_i}^2 L_{\mu\nu} H_{AA}^{\mu\nu}. \tag{3.12}$$

The lepton tensor $L_{\mu\nu}$ is relatively simple and does not contain strong corrections in NLO. It is the same for vector-vector- and for axial-axial-case, because we can swap a γ_5-matrix twice in the Dirac trace of the axial case and use $\gamma_5^2 = 1$. Our lepton tensor includes the incoming leptons and the propagator of the intermediate boson excluding the vertex connecting the boson to the quark pair. A calculation of the squared matrix element yields:

$$\begin{aligned} \mathcal{M}_L \mathcal{M}_L^* &= \frac{e^2}{4q^4}\mathrm{Tr}(\gamma_\mu l_1 \gamma_\nu l_2) \\ &= \frac{e^2}{s^2}\left(l_{1\mu}l_{2\nu} + l_{2\mu}l_{1\nu} - \frac{s}{2}g_{\mu\nu}\right). \end{aligned} \tag{3.13}$$

We include the flux factor $1/(2s)$ of the incoming particles in the leptonic tensor:

$$L_{\mu\nu} = \frac{e^2}{2s^3}(l_{1\mu}l_{2\nu} + l_{2\mu}l_{1\nu} - \frac{s}{2}g_{\mu\nu}). \tag{3.14}$$

In reference [15] projectors $P_T^{\mu\nu}$ and $P_L^{\mu\nu}$ are given which can be used, when contracted with he hadronic tensor, to calculate the transversal and the longitudinal part of the cross section. In the following paragraphs we verify those projectors and give an expression for the leptonic tensor as a linear combination of $P_T^{\mu\nu}$ and $P_L^{\mu\nu}$.

We contract the lepton tensor with the general hadron tensor. The general ansatz for a Lorentz-invariant hadronic tensor $H_G^{\mu\nu}$ depending on two four-momenta q and p_1 is given by:

$$\begin{aligned} H_G^{\mu\nu} &= C_1\left(-g^{\mu\nu} + \frac{q^\mu q^\nu}{s}\right) + C_2\left(p_1^\mu - q^\mu\frac{p_1 q}{s}\right)\left(p_1^\nu - q^\nu\frac{p_1 q}{s}\right) \\ &\quad + C_3 i\epsilon^{\mu\nu\rho\sigma}q_\sigma p_{1\rho} + C_4\frac{q^\mu q^\nu}{s} + C_5(q^\mu p_1^\nu + p_1^\mu q^\nu) \end{aligned} \tag{3.15}$$

with scalar functions C_1 to C_5.

Now we contract this tensor with the leptonic tensor:

$$\begin{aligned} & L_{\mu\nu}H_G^{\mu\nu} \\ = \; & \frac{e^2}{2s^2}\left(\frac{D-2}{4}C_1(1+\cos^2\theta) + \left(\frac{D-2}{4}C_1 + \frac{1}{8}sy^2\beta_y^2 C_2\right)(1-\cos^2\theta)\right) \end{aligned} \tag{3.16}$$

with

$$\beta_y = \sqrt{1-\rho_a/y}. \tag{3.17}$$

The projectors from [15] have the following form:

$$\begin{aligned} P^L_{\mu\nu} &= \frac{\left(p_{1\mu} - q_\mu \frac{p_1 q}{s}\right)\left(p_{1\nu} - q_\nu \frac{p_1 q}{s}\right)}{(s/4) y^2 \beta_y^2} \\ P^T_{\mu\nu} &= \frac{1}{2}\left[-g_{\mu\nu} + \frac{q_\mu q_\nu}{s} - \frac{\left(p_{1\mu} - q_\mu \frac{p_1 q}{s}\right)\left(p_{1\nu} - q_\nu \frac{p_1 q}{s}\right)}{(s/4) y^2 \beta_y^2}\right]. \end{aligned} \tag{3.18}$$

The action of the projectors onto the general hadronic tensor is the following:

$$\begin{aligned} P^L_{\mu\nu} H_G^{\mu\nu} &= C_1 + \frac{1}{4} s y^2 \beta_y^2 C_2, \\ P^T_{\mu\nu} H_G^{\mu\nu} &= \frac{D-2}{2} C_1. \end{aligned} \tag{3.19}$$

The projectors don't contain a dependence of $\cos\theta$. So in order to write the lepton tensor in terms of the projectors we also integrate out $\cos\theta$ in (3.16). This is a trivial task in LO, but as we will see further down, the hadronic tensor is no longer independent from θ when applying dimensional regularization. It contains the factor $(1-\cos^2\theta)^{\epsilon/2}$, which contributes terms of $\mathcal{O}(\epsilon)$. The equations

$$\begin{aligned} \int \mathrm{d}\cos\theta (1+\cos^2\theta)(1-\cos^2\theta)^{\epsilon/2} &= \frac{8}{3} + \left(-\frac{26}{9} + \frac{8\ln 2}{3}\right)\epsilon + \mathcal{O}\left(\epsilon^2\right) \\ \int \mathrm{d}\cos\theta (1-\cos^2\theta)^{1+\epsilon/2} &= \frac{4}{3} + \frac{2}{9}\left(-5 + 6\ln 2\right)\epsilon + \mathcal{O}\left(\epsilon^2\right) \end{aligned} \tag{3.20}$$

allow us to fix the coefficients C_1 and C_2 and we can write the operation of contracting leptonic and hadronic tensor and integrating out $\cos\theta$ in terms of the projectors:

$$\int_{-1}^{1} \mathrm{d}\cos\theta\, L^{\mu\nu} = \frac{e^2}{4s^2}\left(\frac{4}{3}\left(1 + \epsilon\left(\frac{5}{6} + \ln 2\right)\right) P_L^{\mu\nu} + \frac{8}{3}\left(1 + \epsilon\left(-\frac{5}{6} + \ln 2\right)\right) P_T^{\mu\nu}\right). \tag{3.21}$$

3.3 Tree-level and virtual corrections

3.3.1 Matrix element

The leading order contribution to the matrix element of the hadron tensor is calculated from the tree-level graph in figure (3.2). For the next-to-leading order we have to look at virtual and real corrections. The graphs containing a virtual gluon have two strong vertices so that we get the α_s-term by multiplying a virtual contribution with the tree-level graph's expression.

In this section we focus on the virtual corrections. The main technical problem in this case are Feynman diagrams with loops. In 1-loop-order the resulting expressions are well-known as Passarino-Veltman functions [48]. Furthermore we have to renormalize fields and couplings. On the other hand the phase space for two outgoing particles is relatively simple and the kinematics only allow back-to-back production of quark and anti-quark, so that the phase space integration results in a simple delta-function and does not require any integrations over the matrix element.

First we need the tree-level graph's contributions:

$$\mathcal{M}_T^{\mu} = e\left[\bar{u}(p_1)\gamma^\mu (c_{V,B} + c_{A,B}\gamma_5) v(p_2)\right]\delta_{ij} \tag{3.22}$$

$$\mathcal{M}_T^{\nu *} = e\left[\bar{v}(p_2)\gamma^\nu (c_{V,B} + c_{A,B}\gamma_5) u(p_1)\right]\delta_{ij}. \tag{3.23}$$

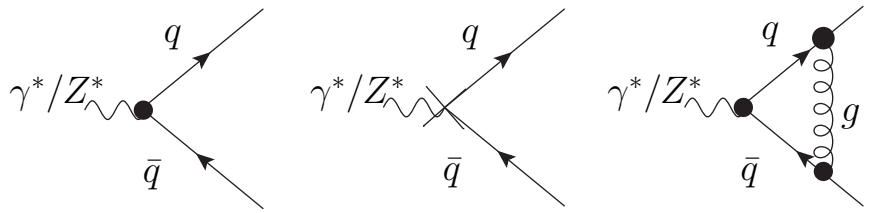

Figure 3.2: Contributing Feynman graphs for $\gamma^*/Z^* \to q\bar{q}$: Born, Counterterm and virtual corrections

We introduce the spinors $\bar{u}(p_1)$ and $v(p_2)$ of the outgoing quark and anti-quark respectively and the constants $c_{V,B}$ and $c_{A,Z}$ for vector and axial coupling, which are $c_{V,Z} = v_f$ and $c_{A,Z} = a_f$ in the case of an incoming Z boson to the fermions ($B = Z$). In case of a photon ($B = \gamma$) the constants are $c_{V,\gamma} = -Q_f$, which is the electrical charge of the fermion in units of the elementary charge, and $c_{A,\gamma} = 0$. We take care of the color factor of QCD with the δ_{ij}, which describes the color conservation of the quark lines at the vertex.

We want to calculate $(|\mathcal{M}_T|^2)^{\mu\nu} = \mathcal{M}_T^\mu \mathcal{M}_T^{\nu *}$ including all color and polarization states of outgoing particles. For the sum over all polarization states of the quarks we apply the formula

$$\sum_{\text{Spins}} [\bar{u}(a)\Gamma_1 u(b)][\bar{u}(b)\Gamma_2 u(a)] = \text{Tr}[\Gamma_1(\not{p}_b + m_b)\Gamma_2(\not{p}_a + m_a)], \tag{3.24}$$

For anti-particles the prefix of the related mass on the right side of the equation changes to a minus sign. Γ_1 and Γ_2 are products of Dirac matrices. With the help of this formula the Dirac chains of the matrix element and of the conjugated matrix element can be easily combined in the algebra software FORM [49]. FORM then evaluates the trace in D dimensions except for the γ_5-matrix, which is only defined in 4 dimensions. We use the naive approach to calculate the γ_5-terms in 4 dimensions, which is sufficient for the vector-vector- and for the axial-axial-part. The contributing graphs to the virtual corrections are the graph with the virtual gluon and the graph with the counterterm vertex in figure (3.2). In general graphs with self-energy corrections to the quarks lines also contribute, but we renormalize the UV divergencies in the on-shell scheme, in which corrections of the external legs don't contribute.

The matrix element for the virtual corrections with the loop momentum l is

$$\begin{aligned}
\mathcal{M}_V^\mu &= -\mathrm{i}eg_s^2 \int \frac{d^D l}{(2\pi)^D \mu^{D-4}} \frac{1}{(l+p_1)^2 - m_q^2} \frac{1}{(l-p_2)^2 - m_q^2} \frac{1}{l^2} \\
&\quad \times \left[\bar{u}(p_1)\gamma^\rho(\not{p}_1 + \not{l} + m)\gamma^\mu(c_{V,B} + c_{A,B}\gamma_5)(-\not{p}_2 + \not{l} + m)\gamma_\rho v(p_2)\right] \\
&\quad \times C_F \delta_{ij}, \\
\mathcal{M}_V^{\nu *} &= \mathrm{i}eg_s^2 \int \frac{d^D l}{(2\pi)^D \mu^{D-4}} \frac{1}{(l+p_1)^2 - m_q^2} \frac{1}{(l-p_2)^2 - m_q^2} \frac{1}{l^2} \\
&\quad \times \left[\bar{v}(p_2)\gamma_\rho(-\not{p}_2 + \not{l} + m)(c_{V,B} + c_{A,B}\gamma_5)\gamma^\mu(\not{p}_1 + \not{l} + m)\gamma^\rho u(p_1)\right] \\
&\quad \times C_F \delta_{ij}.
\end{aligned} \tag{3.25}$$

Here we introduce the strong coupling $g_s^2 = 4\pi\alpha_s$. The group theory factor $C_F = 4/3$ stems from the color factor $\sum_{a,b}[T_a^{(F)} T_b^{(F)}]_{ij}\delta_{ab} = C_F \delta_{ij}$. The 3×3 matrices

$T_c^{(F)}$ are the generators of the color group $SU(3)$. The indices a, b describe the possible color charges of the gluon, the indices i and j the color charges of the outgoing quarks as in LO. Combining matrix elements with the corresponding conjugated matrices and summing over possible color states of the quarks lead to the color factor $C_A C_F = 4$.

We write the loop integral in terms of Passarino-Veltman integrals [48, 50]. The following substitutions are made:

$$\begin{aligned}
\int \frac{\mathrm{d}^D l}{(2\pi)^D \mu^{D-4}} \frac{1}{((l+p_1)^2-m^2)((l-p_2)^2-m^2)l^2} &\rightarrow \frac{\mathrm{i}\pi^2}{(2\pi)^4} C_0(p_1,-p_2,0,m,m) \\
\int \frac{\mathrm{d}^D l}{(2\pi)^D \mu^{D-4}} \frac{l_\mu}{((l+p_1)^2-m^2)((l-p_2)^2-m^2)l^2} &\rightarrow \frac{\mathrm{i}\pi^2}{(2\pi)^4} C_\mu(p_1,-p_2,0,m,m).
\end{aligned} \tag{3.26}$$

The values of the loop integrals will be discussed below. Written in terms of Passarino-Veltman functions eq.(3.25) reads:

$$\begin{aligned}
\mathcal{M}_V^\mu &= \frac{e g_s^2}{16\pi^2} [T_a^{(F)} T_b^{(F)}]_{ij} \delta_{ab} \\
&\times \Bigg(\Big[\bar{u}(p_1)\gamma^\rho (\not{p}_1 + m)\gamma^\mu (c_{V,B} + c_{A,B}\gamma_5)(-\not{p}_2 + m)\gamma_\rho v(p_2) \Big] C_0(p_1,-p_2,0,m,m) \\
&+ \Big[\bar{u}(p_1)\gamma^\rho\gamma^\sigma\gamma^\mu (c_{V,B} + c_{A,B}\gamma_5)(-\not{p}_2 + m)\gamma_\rho v(p_2) \\
&+ \bar{u}(p_1)\gamma^\rho (\not{p}_1 + m)\gamma^\mu (c_{V,B} + c_{A,B}\gamma_5)\gamma^\sigma\gamma_\rho v(p_2) \Big] C_\sigma(p_1,-p_2,0,m,m) \\
&+ \Big[\bar{u}(p_1)\gamma^\rho\gamma^\sigma\gamma^\mu (c_{V,B} + c_{A,B}\gamma_5)\gamma^\tau\gamma_\rho v(p_2) \Big] C_{\sigma\tau}(p_1,-p_2,0,m,m) \Bigg).
\end{aligned} \tag{3.27}$$

The contribution from the counterterm graph is

$$\begin{aligned}
\mathcal{M}_C^\mu &= -\mathrm{i}e(\delta Z_e + \delta Z_\psi) \left[\bar{u}(p_1)\gamma^\mu (c_{V,B} + c_{A,B}\gamma_5) v(p_2) \right] \delta_{ij} \\
\mathcal{M}_C^{\nu *} &= \mathrm{i}e(\delta Z_e + \delta Z_\psi) \left[\bar{v}(p_2)\gamma^\nu (c_{V,B} + c_{A,B}\gamma_5) u(p_1) \right] \delta_{ij}.
\end{aligned} \tag{3.28}$$

We have to renormalize the occuring fields and vertices to fix the value of the renormalization constants $Z_e = e(1+\delta Z_e)$ and $Z_\psi = 1 + \delta Z_\psi$. But first we deal with the Passarino-Veltman integrals.

3.3.2 Loop integrals

We re-write the occuring tensor functions as linear combinations of basic tensors with scalar functions as coefficients. In our calculation we need the following functions:

$$\begin{aligned}
B_\mu(-p_1,0,m) &= -p_{1\mu} B_1(-p_1,0,m) \\
C_\mu(p_1,-p_2,0,m,m) &= p_{1\mu} C_1(p_1,-p_2,0,m,m) - p_{2\mu} C_2(p_1,-p_2,0,m,m) \\
C_{\mu\nu}(p_1,-p_2,0,m,m) &= g_{\mu\nu} C_{00}(p_1,-p_2,0,m,m) + p_{1\mu}p_{1\nu} C_{11}(p_1,-p_2,0,m,m) \\
&\quad + p_{2\mu}p_{2\nu} C_{22}(p_1,-p_2,0,m,m) \\
&\quad - (p_{1\mu}p_{2\nu} + p_{2\mu}p_{1\nu}) C_{12}(p_1,-p_2,0,m,m).
\end{aligned} \tag{3.29}$$

The scalar functions are then decompositioned into more fundamental loop integrals using FeynCalc [51]. To do this by hand one has to contract equations (3.29) with the occuring momentum tensors and the metric tensor. We give the results omitting terms of $\mathcal{O}(\epsilon)$ and introduce the variable $\beta = \sqrt{1-\rho}$.

$$\begin{aligned}
B_1(p_1,0,m) &= \frac{1}{2} - \frac{1}{2}B_0(m,0,m) \qquad (3.30)\\
C_1(p_1,-p_2,0,m,m) &= \frac{1}{-s\beta^2}(B_0(m,0,m) - B_0(\sqrt{s},m,m))\\
C_2(p_1,-p_2,0,m,m) &= C_1(p_1,-p_2,0,m,m)\\
C_{00}(p_1,-p_2,0,m,m) &= \frac{1}{4}B_0(\sqrt{s},m,m) + \frac{1}{4}\\
C_{11}(p_1,-p_2,0,m,m) &= -\frac{1}{2s^2\beta^2}((2m^2-s)(B_0(m,0,m) - B_0(\sqrt{s},m,m))\\
&\quad +s\beta^2)\\
C_{22}(p_1,-p_2,0,m,m) &= C_{11}(p_1,-p_2,0,m,m)\\
C_{12}(p_1,-p_2,0,m,m) &= \frac{1}{s^2\beta^2}(m^2B_0(m,0,m) - m^2B_0(\sqrt{s},m,m) + \frac{1}{2}s\beta^2).
\end{aligned}$$

The results and the methods of calculation for A_0, B_0 and C_0 can be found in literature, for example ref.[50]. We cite the relevant results:

$$\begin{aligned}
A_0(m) &= m^2\left(\Delta - \ln\left(\frac{m^2}{\mu^2}\right) + 1\right) + \mathcal{O}(\epsilon) \qquad (3.31)\\
B_0(p,0,m) &= \Delta - \ln\frac{m^2}{\mu^2} + 2 + \frac{m^2-p^2}{p^2}\ln\left(\frac{m^2-p^2-\mathrm{i}\epsilon}{m^2}\right) + \mathcal{O}(\epsilon)\\
B_0(\sqrt{s},m,m) &= \Delta - \ln\frac{m^2}{\mu^2} + 2 - \beta\ln\left(-\frac{s(1+\beta)}{2m^2} + 1\right) + \mathcal{O}(\epsilon)
\end{aligned}$$

with the pole

$$\Delta := -\frac{2}{\epsilon} - \gamma_E + \ln(4\pi). \qquad (3.32)$$

The function $C_0(p_1,-p_2,0,m,m)$ is taken from ref.[52]:

$$\begin{aligned}
C_0(p_1,-p_2,0,m,m) &= \left(\frac{s}{4\pi\mu^2}\right)^{\epsilon/2}\frac{1}{s\beta}\frac{1}{\Gamma(1+\epsilon/2)}\Bigg[\left(\frac{2}{\epsilon} + \ln\left(\frac{m^2}{s}\right)\right)\ln\left(\frac{1+\beta}{1-\beta}\right)\\
&\quad -2\Bigg(\mathrm{Li}_2\left(\frac{1-\beta}{1+\beta}\right) + \pi^2/3 + \ln\left(\frac{2\beta}{1+\beta}\right)\ln\left(\frac{1-\beta}{1+\beta}\right)\\
&\quad -1/4\ln^2\left(\frac{1-\beta}{1+\beta}\right)\Bigg)\Bigg]. \qquad (3.33)
\end{aligned}$$

For this expression we need Euler's dilogarithm or Spence function $\mathrm{Li}_2(x)$ and Euler's Gamma function $\Gamma(x)$. The dilogarithm is defined by

$$\mathrm{Li}_2(x) = \int_x^0 \mathrm{d}t\frac{\ln(1-t)}{t}. \qquad (3.34)$$

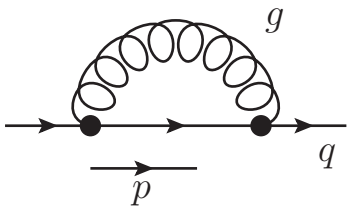

Figure 3.3: Feynman graph for the NLO correction to the quark-propagator

The Gamma function is defined by

$$\Gamma(x) = \int_0^\infty t^{x-1} \mathrm{e}^{-t} \mathrm{d}t, \tag{3.35}$$

and is a generalization of the factorial thanks to its property

$$n! = \Gamma(n+1). \tag{3.36}$$

3.3.3 Renormalization

We have to renormalize the $\gamma q\bar{q}$-/$Zq\bar{q}$-vertex for corrections in α_s. Apart from being necessary for physical meaningful results, this will also cancel the UV singularity of the loop diagram. We will go shortly through the calculation of the required renormalization constants in the on-shell scheme.

We start with the renormalization of the propagator for a heavy quark, which will fix the constants for the renormalized quark mass δm and for the quark field δZ_ψ, which are the $\mathcal{O}(\alpha_s)$-terms of the renormalized mass $m = m_0 + \delta m + \mathcal{O}\left(\alpha_s^2\right)$ and of the wave function renormalization constant $Z_\psi = 1 + \delta Z_\psi + \mathcal{O}\left(\alpha_s^2\right)$.

The self-energy $\Sigma^{q\bar{q}}(p)$ of a heavy quark with momentum p follows from the Feynman graph in figure (3.3):

$$\Sigma_{ij}^{q\bar{q}}(p^2) = \not{p}\Sigma_{V,ij}^{q\bar{q}}(p^2) + m\Sigma_{S,ij}^{q\bar{q}}(p^2) \tag{3.37}$$

with the vector part $\Sigma_{V,ij}^{q\bar{q}}(p^2)$ and the scalar part $\Sigma_{S,ij}^{q\bar{q}}(p^2)$:

$$\begin{aligned}
\Sigma_{S,ij}^{q\bar{q}}(p^2) &= \frac{\alpha_s}{4\pi} C_F (D-2) \left(\frac{p^2+m^2}{p^2} B_0(-p,0,m) - \frac{1}{2p^2} A_0(m) \right) \delta_{ij} \\
\Sigma_{V,ij}^{q\bar{q}}(p^2) &= -\frac{\alpha_s}{4\pi} C_F D B_0(-p,0,m) \delta_{ij}.
\end{aligned} \tag{3.38}$$

After the renormalization constants are introduced in the Lagrangian, the renormalized vertex function $\hat{\Gamma}_{ij}^{q\bar{q}}(-p,p)$ has the following form:

$$\hat{\Gamma}_{ij}^{q\bar{q}}(-p,p) = \mathrm{i}\not{p}\left(\delta_{ij} + \Sigma_{V,ij}^{q\bar{q}}(p) + \delta_{ij}\delta Z_\psi\right) + \mathrm{i}m\left(-\delta_{ij} + \Sigma_{S,ij}^{q\bar{q}}(p) - \delta Z_\psi \delta_{ij} - \frac{\delta m}{m}\delta_{ij}\right). \tag{3.39}$$

The on-shell-condition dictates that the pole of the propagator is at $p^2 = m^2$. Use of this condition written as

$$\hat{\Gamma}_{ij}^{q\bar{q}}(-p,p)u(p) = 0 \tag{3.40}$$

and the Dirac equation $(\not{p} - m)u(p) = 0$ allows us to calculate the first renormalization constant:

$$\begin{aligned} \frac{\delta m}{m}\delta_{ij} &= \Sigma^{q\bar{q}}_{V,ij}(m^2) + \Sigma^{q\bar{q}}_{S,ij}(m^2) \\ &= -\frac{\alpha_s}{4\pi} 2 C_F B_0(-p, 0, m)\delta_{ij}. \end{aligned} \tag{3.41}$$

The second condition is that the residuum of the propagator is 1 at $\not{p} = m$. This can be written as

$$\left(\lim_{p^2 \to m^2} \frac{\mathrm{i}}{\not{p} - m} \hat{\Gamma}^{q\bar{q}}_{ij} \right) u(p) = 1 \tag{3.42}$$

and leads - again with the help of the Dirac equation - to the general formula for the fermion field renormalization constant

$$\delta Z_\psi \delta_{ij} = -\Sigma^{q\bar{q}}_{V,ij}(m^2) - 2m^2 \left(\Sigma^{q\bar{q}\prime}_{V,ij}(m^2) + \Sigma^{q\bar{q}\prime}_{S,ij}(m^2) \right). \tag{3.43}$$

The on-shell condition for the coupling e is, that the NLO contribution becomes 0 in the limit of a soft incoming boson. That means that the renormalized vertex $\hat{\Gamma}_{\mu,ij}(q, p_1, p_2)$for $q = 0$ fulfills the condition

$$\bar{u}(p)\hat{\Gamma}_{\mu,ij}(0, -p, p)u(p) = \bar{u}(p)\gamma_\mu \delta_{ij} u(p), \tag{3.44}$$

where the right-side term is the LO contribution to the vertex. Subtracting the LO contributions on both sides yields

$$\bar{u}(p) \left(\Lambda_{\mu,ij}(p, p) + \gamma_\mu \delta_{ij} (\delta Z_e + \delta Z_\psi) \right) u(p) = 0. \tag{3.45}$$

In the on-shell scheme and dimensional regularization we can use the Ward identity to calculate the vertex correction:

$$\begin{aligned} \Lambda_{\mu,ij}(p, p) &= \frac{\partial}{\partial p^\mu} \Sigma^{q\bar{q}}_{ij}(p) \\ &= \gamma_\mu \Sigma^{q\bar{q}}_{V,ij}(p^2) + 2p_\mu \left(\not{p} \Sigma^{q\bar{q}\prime}_{V,ij}(p^2) + m \Sigma^{q\bar{q}\prime}_{S,ij}(p^2) \right). \end{aligned} \tag{3.46}$$

We insert the latter equation into eq.(3.45), use the Dirac equation and the Gordon identity and $p^2 = m^2$:

$$0 = \bar{u}(p)\gamma_\mu u(p) \left[\Sigma^{q\bar{q}}_{V,ij}(m^2) + 2m^2 \left(\Sigma^{q\bar{q}\prime}_{V,ij}(m^2) + \Sigma^{q\bar{q}\prime}_{S,ij}(m^2) \right) + (\delta Z_e + \delta Z_\psi)\delta_{ij} \right]. \tag{3.47}$$

A comparison with eq.(3.43) leads to

$$\delta Z_e = 0. \tag{3.48}$$

As a consequence only Z_ψ contributes to the counterterm vertex. We put equation (3.38) into (3.43) and receive Z_ψ in terms of Passarino-Veltman-integrals:

$$\delta Z_\psi = \frac{\alpha_s}{4\pi} C_F \left(\frac{2 - D}{2m^2} A_0(m^2) + 4m^2 B_0'(m^2, 0, m) \right). \tag{3.49}$$

We use equation (2.5.114) from reference [53], where the IR divergence is controlled with the help dimensional regularization:

$$B_0'(m^2, 0, m) = \frac{1}{2m^2} \left(\Delta + \ln\left(\frac{\mu^2}{m^2} \right) + 2 \right) + \mathcal{O}(\epsilon). \tag{3.50}$$

The result for the renormalization constant is

$$\delta Z_\psi = \frac{\alpha_s}{4\pi} C_F \left(-3\Delta + 3\ln\left(\frac{m^2}{\mu^2}\right) - 4 \right) + \mathcal{O}(\epsilon). \tag{3.51}$$

We can put this result into eq. (3.28). It is interesting to note that a contribution of $-\Delta$ will cancel with the pole of the loop diagram. The remaining -2Δ are related to the IR divergency of the radiation of a soft gluon and will disappear when we combine virtual and real corrections.

3.3.4 Phase space integrand

The general phase space factor for two massive particles - both with the mass m - in the final state is:

$$\mathrm{d}^{2D-2}P_2 = \frac{\mathrm{d}^{D-1}\vec{p}_1}{(2\pi)^{D-1}(2E_1)} \frac{\mathrm{d}^{D-1}\vec{p}_2}{(2\pi)^{D-1}(2E_2)} (2\pi)^D \delta^D(q - p_1 - p_2), \tag{3.52}$$

where the $\vec{p}_n$ are the momentum components of the four-vectors of the particles and the E_n are the energies. D is assumed to be an integer number for the first steps, before we reach a point where we can regard the result as an analytic continuation. The relation between energy and momentum is

$$|\vec{p}_n| = \beta_n E_n, \tag{3.53}$$

where

$$\beta_n := \sqrt{1 - \frac{m^2}{E_n^2}}. \tag{3.54}$$

β_1 is identical to our formerly introduced variable β_y, but the point here is to stress the differentiation of the variables of the two particles.

We integrate over $\vec{p}_2 = -\vec{p}_1$ using $D-1$ components of the delta function. Now the remaining integrand $\mathrm{d}\vec{p}_1$ is written in polar coordinates:

$$\frac{\mathrm{d}^{D-1}\vec{p}_1}{(2E_1)} = \frac{1}{2E_1} |\vec{p}_1|^{D-2} \mathrm{d}|\vec{p}_1| \prod_{k=1}^{D-2} \sin^{D-2-k}\theta_k \, \mathrm{d}\theta_k. \tag{3.55}$$

For the integration the following formula is used:

$$\int_0^\pi \sin^n\theta \, \mathrm{d}\theta = \sqrt{\pi} \frac{\Gamma\left(\frac{n+1}{2}\right)}{\Gamma\left(\frac{n+2}{2}\right)}. \tag{3.56}$$

The integration over all angles except for θ_1, which is identical to our θ, leads to

$$\int_0^\pi \prod_{k=2}^{D-2} \sin^{D-2-k}\theta_k \mathrm{d}\theta_k = \pi^{\frac{D-3}{2}} \prod_{k=2}^{D-2} \frac{\Gamma\left(\frac{D}{2} - \frac{k}{2} - \frac{1}{2}\right)}{\Gamma\left(\frac{D}{2} - \frac{k}{2}\right)} \tag{3.57}$$

$$= \pi^{\frac{D-2}{2}} \frac{1}{\Gamma\left(\frac{D}{2} - 1\right)}. \tag{3.58}$$

Now we put the parts together and convert with $E_1 = y\sqrt{s}/2$ to our set of variables. The result is

$$\mathrm{d}P_2 = \frac{\beta_y^{1+\epsilon} y^\epsilon s^{\epsilon/2}}{2^{4+2\epsilon}\pi^{1+\epsilon/2}} \frac{(1-\cos^2\theta)^{\epsilon/2}}{\Gamma(1+\epsilon/2)} \delta(1-y) \mathrm{d}y \, \mathrm{d}(\cos\theta). \tag{3.59}$$

3.3.5 Final steps and pole result

Now we can put together matrix element and phase space according to eq.(3.8). We do this with the help of a FORM script in the following order:

- The starting point is the expression $P_{\mu\nu}^{L/T}\mathcal{M}^{\mu}\mathcal{M}^{\nu *}$.
- The projectors are replaced by their expressions (3.18).
- We calculate the squared matrix element from equations (3.22), (3.27) and (3.28). FORM multiplies the respective elements of the Dirac algebra to one chain.
- The formulas for the Passarino-Veltman integrals from equations (3.30) and (3.31) are put in.
- Now FORM evaluates the traces of the Dirac chains, which leads to a result in terms of scalar products.
- The scalar products are expressed through our preferred variables, e.g. $p_1{\cdot}p_2 = 2-\rho$.
- The result is multiplied with the phase space factor (3.59).
- All functions of ϵ are replaced by power expansions of ϵ up to $\mathcal{O}(\epsilon)$ where necessary.
- FORM automatically expands all expressions, so we can let it discard all terms of $\mathcal{O}(\epsilon)$ now.
- The remaining work is some tidying up, which means that higher powers of factors in denominator and numerator are cancelled. Also we replace ρ by $\rho = [2-\rho]+\rho$ for an easier comparison with the literature result.

The intermediate result has no physical meaning, because the contribution from the real corrections has to be added. However the result for the pole in ϵ is interesting, because we expect to cancel with the pole from the real corrections. The pole in the virtual corrections stems from loop integrals, while the pole of the real corrections occurs in the phase space integration. Therefore this is a strong check of this calculation, so we write down the $\mathcal{O}\left(\epsilon^{-1}\right)$-terms of the intermediate result. We calculate the contributions for the vector-vector-coupling and for axial-axial-coupling seperately for clearer output:

$$
\begin{aligned}
P_{\mu\nu}^{L}\mathcal{M}_{V+C}^{\mu}\mathcal{M}_{V+C}^{\nu *}\mathrm{d}P_2|_{VV} &= C_A C_F 16\pi^2\alpha\alpha_s\frac{1}{\epsilon}\rho\left(2\beta-(2-\rho)\ln\left(\frac{1+\beta}{1-\beta}\right)\right),\\
P_{\mu\nu}^{T}\mathcal{M}_{V+C}^{\mu}\mathcal{M}_{V+C}^{\nu *}\mathrm{d}P_2|_{VV} &= C_A C_F 16\pi^2\alpha\alpha_s\frac{1}{\epsilon}\left(2\beta-(2-\rho)\ln\left(\frac{1+\beta}{1-\beta}\right)\right),\\
P_{\mu\nu}^{L}\mathcal{M}_{V+C}^{\mu}\mathcal{M}_{V+C}^{\nu *}\mathrm{d}P_2|_{AA} &= 0, \qquad (3.60)\\
P_{\mu\nu}^{T}\mathcal{M}_{V+C}^{\mu}\mathcal{M}_{V+C}^{\nu *}\mathrm{d}P_2|_{AA} &= C_A C_F 16\pi^2\alpha\alpha_s\\
&\quad\times\frac{1}{\epsilon}\left(2\beta(1-\rho)-(\rho^2-3\rho+2)\ln\left(\frac{1+\beta}{1-\beta}\right)\right)
\end{aligned}
$$

with $\mathcal{M}_{V+C}^{\mu} = \mathcal{M}_{V}^{\mu}+\mathcal{M}_{C}^{\mu}$.

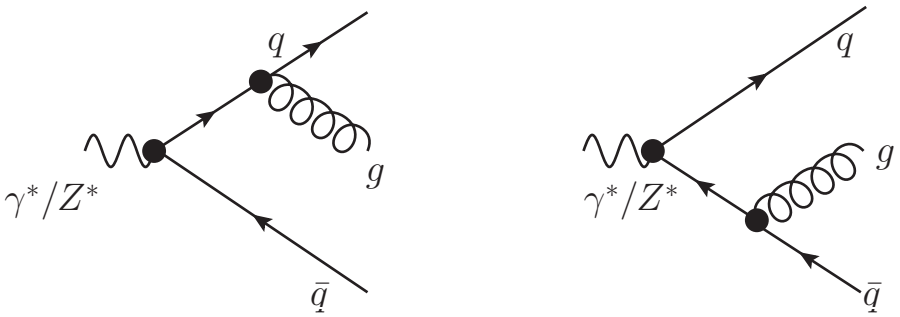

Figure 3.4: Contributing Feynman graphs for $\gamma^*/Z^* \to q\bar{q}g$

3.4 Real Corrections

For the real corrections, we examine the LO process $e^+e^- \to q\bar{q}g$. The treatment of the matrix element becomes simpler, since we don't have any diagrams with loops. Instead the phase space integration becomes more complicated. Two of the three final-state particles' momenta are integrated out completely, which is not possible without an integration over the matrix element. Furthermore the kinematics are more complex and lead to a result, that we write in terms proportional to the plus-distribution $1/(1-y)_+$ in addition to the terms proportional to the delta-function $\delta(1-y)$.

3.4.1 Matrix element

The two Feynman graphs in fig.(3.4) contribute to the real corrections. The corresponding terms for the matrix elements are:

$$\begin{aligned}\mathcal{M}^{\mu}_{R1} &= eg_s^2 \frac{1}{(p_1+p_3)^2-m^2}\left[\bar{v}(p_2)\gamma_{\omega_1}(\not{p}_1+\not{p}_3+m)\gamma^{\mu}(c_{V,B}+c_{A,B}\gamma_5)u(p_1)\right] \\ &\quad \times(\epsilon^{\omega_1})^*(p_3)[T_c]_{ij} \qquad (3.61)\\ \mathcal{M}^{\mu}_{R2} &= eg_s^2 \frac{1}{(p_2+p_3)^2-m^2}\left[\bar{v}(p_2)\gamma^{\mu}(c_{V,B}+c_{A,B}\gamma_5)(-\not{p}_2-\not{p}_3+m)\gamma_{\omega_1}u(p_1)\right] \\ &\quad \times(\epsilon^{\omega_1})^*(p_3)[T_c]_{ij}.\end{aligned}$$

In addition to the polarization vector of the incoming boson - which is hidden in the projectors - we also have to take the polarization vector $(\epsilon^{\omega 1})^*(p_3)$ of the outgoing gluon into account. In the squared matrix element we sum over all polarization states of the outgoing gluon. In this case we can use the equation

$$\sum_{\text{Polar.}} (\epsilon^{\omega_1})^*(p_3)(\epsilon^{\omega_2})(p_3) = -g^{\omega_1\omega_2}. \qquad (3.62)$$

The color factor in the squared matrix element becomes

$$\sum_{i,j}[T_c]_{ij}[T_c]_{ji} = \text{Tr}[T_cT_c] = C_AC_F = 4. \qquad (3.63)$$

3.4.2 Phase space integrand for three final state particles

We have to extend the phase space factor (3.52) to include the radiated real gluon, which is considered massless. We introduce a factor for the third particle and

adapt the formula in the delta function, which accounts for energy and momentum conservation. This time we use the delta function to integrate out $\vec{p}_3$:

$$\begin{aligned} & \int \mathrm{d}^{3D-3}P_3 \qquad (3.64)\\ = & \int \frac{\mathrm{d}^{D-1}\vec{p}_1}{(2\pi)^{D-1}(2E_1)}\frac{\mathrm{d}^{D-1}\vec{p}_2}{(2\pi)^{D-1}(2E_2)}\frac{\mathrm{d}^{D-1}\vec{p}_3}{(2\pi)^{D-1}(2E_3)}(2\pi)^D\delta^D(q-p_1-p_2-p_3)\\ = & \int \frac{\mathrm{d}^{D-1}\vec{p}_1}{(2\pi)^{D-1}(2E_1)}\frac{\mathrm{d}^{D-1}\vec{p}_2}{(2\pi)^{D-1}(2E_2)}\frac{(2\pi)\delta(\sqrt{s}-E_1-E_2-E_3)}{2E_3}. \end{aligned}$$

The angular dependence of $\vec{p}_1$ is treated in analogy to the two-particle-phase space using equations (3.55) to (3.57). For $\vec{p}_2$ we look at the angle between the vectors $\vec{p}_1$ and $\vec{p}_2$ and introduce the variable ζ, which is defined to be the cosine of the angle between $\vec{p}_1$ and $\vec{p}_2$. So if one thinks of $\vec{p}_1$ defining the z-axis of a coordinate system for $\vec{p}_2$, then ζ is the cosine of the polar angle of $\vec{p}_2$ in spherical coordinates. Integrating out the azimuthal angle of $\vec{p}_2$ gives:

$$\int \frac{\mathrm{d}^{D-1}\vec{p}_2}{(2\pi)^{D-1}(2E_2)} = \frac{1}{2}E_2^{D-3}(\beta_2 E_2)^{D-3}\mathrm{d}E_2\int_{-1}^{1}\mathrm{d}\zeta\,(1-\zeta^2)^{\frac{D-4}{2}}\frac{\pi^{\frac{D-2}{2}}}{\Gamma\left(\frac{D-2}{2}\right)}. \qquad (3.65)$$

Now we rewrite the delta function in (3.64) to integrate out ζ:

$$\begin{aligned} \frac{\delta(\sqrt{s}-E_1-E_2-E_3)}{2E_3} &= \delta([q-p_1-p_2-p_3]^2) \qquad (3.66)\\ &= \frac{\delta\left(\zeta-\frac{1}{\beta_1\beta_2}\left(1+2\frac{1+\rho/2-y_1-y_2}{y_1y_2}\right)\right)}{sy_1y_2\beta_1\beta_2}. \end{aligned}$$

We replace the number of dimensions by $D=4+\epsilon$ and the phase space integrand becomes:

$$\mathrm{d}P_3 = \frac{s}{2^{2+2\epsilon}(4\pi)^3}\left(\frac{s}{4\pi}\right)^{\epsilon}\frac{(1-\cos^2\theta)^{\epsilon/2}}{\Gamma(1+\epsilon/2)}\left(1-\zeta^2\right)^{\epsilon/2}(\beta_1y_1\beta_2y_2)^{\epsilon}\mathrm{d}y_1\mathrm{d}y_2\mathrm{d}\cos\theta. \qquad (3.67)$$

We will only be able to integrate over y_2 after the multiplication with the squared matrix element, since the latter is not independent of y_2. Therefore we are going to need the integration boundaries for the integration over y_2. Since ζ is a cosine, it can only run from -1 to 1. By setting ζ^2 - as defined through eq.(3.66) - to 1, we get a relation between y_1 and y_2 at the boundary. Rearranged for y_2 the equation is:

$$y_2 = \frac{\rho+2(1-y_1)-y_1\rho/2-y_1(1-y_1)(1\mp\beta_1)}{\rho/2+2(1-y_1)}. \qquad (3.68)$$

The minus sign in the last term gives the upper bound, while the plus sign is used in the lower bound. Note that the bounds coincide for the case $y_1=\sqrt{\rho}$, which is the lower bound of y_1.

3.4.3 Integration of particle energy

Putting together all components for our cross section, we get the following formula:

$$P_{\mu\nu}^{L/T}\mathcal{M}_R^{\mu}\mathcal{M}_R^{\nu *}\mathrm{d}^2P_3 = \frac{s}{2^{2+2\epsilon}(4\pi)^3}\left(\frac{s}{4\pi}\right)^{\epsilon}\frac{1}{\Gamma(1+\epsilon/2)}(1-\zeta^2)^{\epsilon/2}(\beta_1y_1\beta_2y_2)^{\epsilon}$$

$$\times \mathrm{d}y_1 \mathrm{d}y_2 P_{\mu\nu}^{L/T} (\mathcal{M}_{R1}^{\mu} + \mathcal{M}_{R2}^{\mu})(\mathcal{M}_{R1}^{\nu *} + \mathcal{M}_{R2}^{\nu *}). \tag{3.69}$$

After factoring out all factors which are independent of y_1 and y_2, we have to solve the following integral:

$$f^{L/T}(\rho) = \int \mathrm{d}y_1 \int \mathrm{d}y_2 (\beta_1 y_1 \beta_2 y_2)^{\epsilon} (1-\zeta^2)^{\epsilon/2} P_{\mu\nu}^{L/T} \mathcal{M}_R^{\mu} \mathcal{M}_R^{\nu *}. \tag{3.70}$$

We substitute y_2 by the new variable v which has the property that the limits of the inner integral become 0 and 1. This eliminates the problem, that the width of the integration interval becomes 0 for $y_1 \to \sqrt{\rho}$, while the integrand becomes infinite. We achieve this by replacing y_2 by

$$y_2(v) = \frac{\rho + 2(1-y_1) - y_1\rho/2 - y_1(1-y_1)(1-\beta_1) - 2y_1(1-y_1)\beta_1 v}{\rho/2 + 2(1-y_1)} \tag{3.71}$$

so that v is

$$v(y_2) = \frac{\rho/2 + 1 - y_1}{y_1(1-y_1)\beta_1} - \frac{\rho}{4(1-y_1)\beta_1} - \frac{1-\beta_1}{2\beta_1} - \frac{\rho/4 + 1 - y_1}{y_1(1-y_1)\beta_1} y_2. \tag{3.72}$$

The differential is

$$\frac{\mathrm{d}y_2}{\mathrm{d}v} = -\frac{y_1(1-y_1)\beta_1}{\rho/4 + 1 - y_1}. \tag{3.73}$$

With this definition the inner integral runs from 1 to 0. So the minus sign is used to exchange the limits. Equation (3.70) then becomes

$$\begin{aligned} f^{L/T}(\rho) &= \int_{\sqrt{\rho}}^{1} \mathrm{d}y_1 \frac{(1-y_1)^{1+\epsilon}}{(\rho/4 + 1 - y_1)^{1+\epsilon/2}} (y_1^2 - \rho)^{\frac{1+\epsilon}{2}} \\ &\quad \times \int_0^1 \mathrm{d}v (4v(1-v))^{\epsilon/2} P_{\mu\nu}^{L/T} \mathcal{M}_R^{\mu} \mathcal{M}_R^{\nu *}. \end{aligned} \tag{3.74}$$

The squared matrix element, the calculation of its trace and the multiplication with the phase space factor can be implemented straightforward in FORM. At this point we examine the intermediate result, where the terms are sorted by their dependence of $y_2(v)$. From the phase space part we have the factor

$$\mathrm{d}^2 P_3 \sim v(4v(1-v))^{\epsilon/2}. \tag{3.75}$$

In the matrix element we find terms proportional to $y_2(v)$, $(1-y_2(v))^{-1}$, $(1-y_2(v))^{-2}$ and terms independent of $y_2(v)$. We calculate these integrals with the help of Mathematica up to $\mathcal{O}(\epsilon)$:

$$\int_0^1 \mathrm{d}v \, (4v(1-v))^{\epsilon/2} = 1 + \epsilon(\ln 2 - 1) + \mathcal{O}\left(\epsilon^2\right), \tag{3.76}$$

$$\int_0^1 \mathrm{d}v \, v(4v(1-v))^{\epsilon/2} = \frac{1}{2} + \frac{1}{2}\epsilon(\ln 2 - 1) + \mathcal{O}\left(\epsilon^2\right),$$

$$\int_0^1 \mathrm{d}v \frac{(4v(1-v))^{\epsilon/2}}{1-y_2(v)} = \frac{\rho}{8\beta(1-y_1)}\left(4\ln\left(\frac{1+\beta}{1-\beta}\right)+\epsilon\left(4\ln 2\ln\left(\frac{1+\beta}{1-\beta}\right)\right.\right.$$
$$\left.\left.+\mathrm{Li}_2\left(-\frac{4\beta}{(1-\beta)^2}\right)-\mathrm{Li}_2\left(-\frac{4\beta}{(1+\beta)^2}\right)\right)\right)+\mathcal{O}\left(\epsilon^2\right),$$

$$\int_0^1 \mathrm{d}v \frac{(4v(1-v))^{\epsilon/2}}{(1-y_2(v))^2} = \frac{1}{(1-y_1)^2}\left(1+\epsilon\left(\ln 2-\frac{2-\rho}{2\beta}\ln\left(\frac{1+\beta}{1-\beta}\right)\right)\right)+\mathcal{O}\left(\epsilon^2\right).$$

FORM identifies the dependence on $y_2(v)$ of each term and substitutes the relevant factors by the respective integration result. After this integration we have a result for $\mathrm{d}\sigma/\mathrm{d}y_1$, but it needs further treatment for the pole at $y_1 = 1$.

3.4.4 Pole subtraction

The real corrections contain singularities for $y_1 \to 1$. In order to handle this singularities we write the differential cross section in terms of two distributions: The first is the delta-distribution, the other one is the plus distribution, which we defined in equation (2.13). Alternatively it can be defined by:

$$\left(\frac{1}{1-y}\right)_+ = \lim_{\beta\to 0}\left[\theta(1-y-\beta)\frac{1}{1-y}-\delta(1-y-\beta)\int_0^{1-\beta}\frac{1}{1-\hat{y}}\mathrm{d}\hat{y}\right]. \tag{3.77}$$

The latter form shows the basic properties of a plus distribution. It behaves just like a normal function for $y < 1$, however when integrating up to $y = 1$, where the pole is, the integral yields zero due to the second term. So the plus distribution is IR-safe by construction. We use it to split our result in a part for $y < 1$ written in terms of the distribution and one for the pole at $y = 1$ proportional to $\delta(1-y)$, which can be added to the virtual contributions. Since we know that the first part is IR-safe it can be calculated in 4 dimensions. Only for $y = 1$ we need the result in $4+\epsilon$ dimensions.

In detail the splitting looks as follows. The function, which we write under an integral to deal with distributions, has the form

$$\sigma = \int_{\sqrt{\rho}}^1 \mathrm{d}y_1 \frac{R(y_1)}{(1-y_1)^{1-\epsilon}}, \tag{3.78}$$

where $R(y_1)$ is finite at $y_1 = 1$. We bring the integral in the form of equation (2.13):

$$\begin{aligned}\sigma &= \int_{\sqrt{\rho}}^1 \mathrm{d}y_1 \frac{R(y_1)-R(1)}{(1-y_1)^{1-\epsilon}} + \int_{\sqrt{\rho}}^1 \mathrm{d}y_1 \frac{R(1)}{(1-y_1)^{1-\epsilon}} \qquad (3.79)\\ &= \int_{\sqrt{\rho}}^1 \mathrm{d}y_1 \frac{R(y_1)}{(1-y_1)_+} + \int_0^1 \mathrm{d}y_1 \frac{R(1)}{(1-y_1)^{1-\epsilon}} + \mathcal{O}(\epsilon)\\ &= \int_{\sqrt{\rho}}^1 \mathrm{d}y_1 \frac{R(y_1)}{(1-y_1)_+} + \frac{1}{\epsilon}R(1) + \mathcal{O}(\epsilon)\end{aligned}$$

$$= \int_{\sqrt{\rho}}^{1} \left[\mathrm{d}y_1 \frac{R(y_1)}{(1-y_1)_+} + \frac{1}{\epsilon} R(1)\delta(1-y_1) \right] + \mathcal{O}(\epsilon).$$

The result shows that we need $R(y_1 = 1)$ up to $\mathcal{O}(\epsilon)$, since it is multiplied with the pole. The more general function $R(y_1)$ can be integrated in 4 dimensions.

3.4.5 Implementation in FORM

We calculate the two contributions from equation (3.79) in two seperate FORM scripts. The script for the plus-distribution part is in principle complete after the integration of y_2. We use FORM for some substitutions to simplify the result and the comparison to the literature result.

The script for the soft-gluon part, for which we require $R(1)$ in D dimensions, works as follows: The matrix element is calculated and y_2 integrated. For the factors $(y_1^2 - \rho)$ and $\rho/4 + 1 - y_1$ within $R(y_1)$ we can set y_1 to 1. The occuring functions $\beta_1(y_1)$ are replaced by β. What remains of y_1 are factors of $(1-y_1)^{\epsilon-1}$. We can drop terms without this factor, since they don't contribute to the pole. In the remaining terms we perform the integration over y_1 by replacing $(1-y_1)^{\epsilon-1}$ with $1/\epsilon$. After that, the script performs some simplifications of the result. Analogue to the pole result of the virtual corrections (3.60), we write down the $\mathcal{O}\left(\epsilon^{-1}\right)$ terms:

$$\begin{aligned}
\int P^L_{\mu\nu} \mathcal{M}^\mu_R \mathcal{M}^{\nu *}_R \mathrm{d}^2 P_3|_{VV} &= C_A C_F 16\pi^2 \alpha\alpha_s \frac{1}{\epsilon}\rho \left(-2\beta + (2-\rho)\ln\left(\frac{1+\beta}{1-\beta}\right)\right), \\
\int P^T_{\mu\nu} \mathcal{M}^\mu_R \mathcal{M}^{\nu *}_R \mathrm{d}^2 P_3|_{VV} &= C_A C_F 16\pi^2 \alpha\alpha_s \frac{1}{\epsilon} \left(-2\beta + (2-\rho)\ln\left(\frac{1+\beta}{1-\beta}\right)\right), \\
\int P^L_{\mu\nu} \mathcal{M}^\mu_R \mathcal{M}^{\nu *}_R \mathrm{d}^2 P_3|_{AA} &= 0, \\
\int P^T_{\mu\nu} \mathcal{M}^\mu_R \mathcal{M}^{\nu *}_R \mathrm{d}^2 P_3|_{AA} &= C_A C_F 16\pi^2 \alpha\alpha_s \\
&\quad \times \frac{1}{\epsilon} \left(-2\beta(1-\rho) + (\rho^2 - 3\rho + 2)\ln\left(\frac{1+\beta}{1-\beta}\right)\right).
\end{aligned} \tag{3.80}$$

The integral sign refers to the integration over y_2. We see that these poles cancel with the poles from the virtual corrections in eq.(3.60) as they are supposed to.

3.5 Result

We can now insert the results from our FORM scripts into equation (3.12) and compare the result with the one from [5]. It is identical and written in the following decomposition:

$$\frac{\mathrm{d}\sigma^P_{q_i}}{\mathrm{d}y}(y,\rho) = N_c \sigma_0 \left[V^2_{q_i} F^{(v)}_P(y,\rho) + A^2_{q_i} F^{(a)}_P(y,\rho) \right]. \tag{3.81}$$

Here we use the color factor $N_c = 3$ and the leading order total cross section without mass effects

$$\sigma_0 = \frac{4\pi\alpha^2}{3s}. \tag{3.82}$$

The coefficient functions are then divided into Born, virtual-soft and real contributions:

$$F_P^{(u)}(y,\rho) = \delta(1-y)B_P^{(u)}(\rho) + \frac{\alpha_s(\mu)}{2\pi}C_F\left[\delta(1-y)S_P^{(u)}(\rho) + \left(\frac{1}{1-y}\right)_+ R_P^{(u)}(y,\rho)\right]. \tag{3.83}$$

The LO terms are

$$B_T^{(v)}(\rho) = \beta, \quad B_L^{(v)}(\rho) = \frac{\rho\beta}{2}, \quad B_T^{(a)}(\rho) = \beta^3, \quad B_L^{(a)}(\rho) = 0. \tag{3.84}$$

For the NLO coefficient functions we use the short-hand notation:

$$\begin{aligned} \tau_y &= 1-y, \\ \xi(y,\rho) &= \ln\left(\frac{\rho - 2y - 2\sqrt{y^2-\rho}}{\rho - 2y + 2\sqrt{y^2-\rho}}\right). \end{aligned} \tag{3.85}$$

The virtual-soft coefficient functions are:

$$\begin{aligned} S_T^{(v)}(\rho) &= \frac{1}{2}\Bigg((2-\rho)\Big[4\ln\frac{4}{\rho}\ln\frac{1+\beta}{1-\beta} - 4\mathrm{Li}_2\left(-\frac{1-\beta}{2\beta}\right) - 2\ln^2\frac{2\beta}{1-\beta} \\ &\quad + \frac{4}{3}\pi^2 + \ln^2\frac{1+\beta}{1-\beta} + \mathrm{Li}_2\left(-\frac{4\beta}{(1-\beta)^2}\right) - \mathrm{Li}_2\left(\frac{4\beta}{(1+\beta)^2}\right)\Big] \\ &\quad + (10-8\rho)\ln\frac{1+\beta}{1-\beta} - 4\beta - 8\beta\ln\frac{4}{\rho}\Bigg), \\ S_L^{(v)}(\rho) &= \frac{\rho}{2}S_T^{(v)}(\rho) - \frac{\rho\beta^2}{2}\ln\frac{1+\beta}{1-\beta}, \\ S_T^{(a)}(\rho) &= \beta^2 S_T^{(v)}(\rho) + 2\rho\beta^2\ln\frac{1+\beta}{1-\beta}, \\ S_L^{(a)}(\rho) &= 0, \\ S_A(\rho) &= \beta S_T^{(v)}(\rho) + \rho\beta\ln\frac{1+\beta}{1-\beta}. \end{aligned} \tag{3.86}$$

The real corrections lead to the following terms:

$$\begin{aligned} R_T^{(v)}(y,\rho) &= \frac{2}{\sqrt{y^2-\rho}}\Big[\rho(2-\tau_y^2) + 4\frac{\tau_y^2(1+\tau_y)^3}{(4\tau_y+\rho)^2} + \tau_y(4+\tau_y)\left(1 - \frac{2\tau_y(1+\tau_y)}{4\tau_y+\rho}\right) \\ &\quad - 2\Big] + \frac{\rho^2(2-\tau_y^2) + \rho(2y^3-7y^2-1) + 2y^2(1+y^2)}{2(y^2-\rho)}\xi(y,\rho), \\ R_L^{(v)}(y,\rho) &= \frac{2}{\sqrt{y^2-\rho}}\left[-\rho(1-\rho) - \tau_y(\tau_y-2\rho) + \frac{2\tau_y^2(1+\tau_y)}{4\tau_y+\rho}\right] \\ &\quad + \frac{\rho^3 + \rho^2(4\tau_y-3) + \rho(3y^2-1)}{2(y^2-\rho)}\xi(y,\rho), \\ R_T^{(a)}(y,\rho) &= \frac{4}{\sqrt{y^2-\rho}}\Big[-\rho^2 + 2\rho y + \tau_y^3 + \frac{3}{2}\tau_y^2 + 2\tau_y - 1 \end{aligned} \tag{3.87}$$

$$
\begin{aligned}
&+\frac{2\tau_y^2(1+\tau_y)^3}{(4\tau_y+\rho)^2}-\frac{\tau_y^2(1+\tau_y)(5\tau_y+4)}{4\tau_y+\rho}\Big]\\
&+\frac{-2\rho^3+8\rho^2 y+\rho y^2(2\tau_y-9)-\rho+2y^2(1+y^2)}{2(y^2-\rho)}\xi(y,\rho),\\
R_L^{(a)}(y,\rho) &= \frac{2\tau_y^2}{\sqrt{y^2-\rho}}\left[\rho+y^2-5-\frac{8\tau_y(1+\tau_y)^3}{(4\tau_y+\rho)^2}-\frac{2(1+\tau_y)}{4\tau_y+\rho}(\tau_y^2-8\tau_y-2)\right]\\
&+\frac{\tau_y^2\rho(\rho+\tau_y^2-2)}{2(y^2-\rho)}\xi(y,\rho),\\
R_A(y,\rho) &= 4\rho-4y+8\frac{\tau_y^2(1+\tau_y)^2}{(4\tau_y+\rho)^2}-4\frac{\tau_y^2(3+\tau_y)}{4\tau_y+\rho}\\
&-\frac{-\rho^2+3\rho y-y(1+y^2)}{\sqrt{y^2-\rho}}\xi(y,\rho).
\end{aligned}
$$

As a bonus we have included the projector for the asymmetric contribution from [15] in our FORM script:

$$P_{\mu\nu}^A = i\epsilon_{\mu\nu\sigma\rho}\frac{q^\rho p_1^\sigma}{sy\beta_y}. \tag{3.88}$$

This projector succesfully reproduces the asymmetric coefficient functions $S_A(\rho)$ and $R_A(y,\rho)$ from [5], despite FORM's naive treatment of traces with γ_5 in four dimensions.

For the hadron production cross section we also need the gluon production cross section. In this case we use the result from reference [5]. To verify the result one could use our matrix elements, but would have to change the integration of the phase space factor and keep the gluon's energy. The problematic soft-gluon case then occurs for $y \to 0$, however it is kinematically forbidden for a soft gluon to fragment into heavy hadrons.

The cross section reads

$$\frac{\mathrm{d}\sigma_g^P}{\mathrm{d}y}(y) = N_c\sigma_0\frac{\alpha_s}{2\pi}C_F\left[V_{q_i}^2 G_P^{(v)}(y,\rho)+A_{q_i}^2 G_P^{(a)}(y)\right] \tag{3.89}$$

with the coefficient functions

$$
\begin{aligned}
G_T^{(v)}(y,\rho) &= 2\left[\frac{1+(1-y)^2}{y}+\rho\frac{1-y}{y}-\frac{\rho^2}{2y}\right]\left(\ln\frac{1+\beta_\tau}{1-\beta_\tau}-\beta_\tau\right)-4\frac{1-\tau}{\tau}\beta_\tau-\frac{\rho^2\beta_\tau}{\tau},\\
G_L^{(v)}(\tau,\rho) &= -\frac{2\rho}{\tau}\ln\frac{1+\beta_\tau}{1-\beta_\tau}+4\beta_\tau\frac{1-\tau}{\tau},\\
G_T^{(a)}(y,\rho) &= 2\left[\frac{1+(1-y)^2}{y}-\rho\frac{1-y}{y}+\frac{\rho^2}{2y}\right]\left(\ln\frac{1+\beta_\tau}{1-\beta_\tau}-\beta_\tau\right)-4\frac{1-y}{y}\beta_\tau+\frac{\rho^2\beta_\tau}{y},\\
G_L^{(a)}(y,\rho) &= \rho\frac{\rho+y^2+2y-4}{y}\ln\frac{1+\beta_\tau}{1-\beta_\tau}+2\beta_\tau(2+\rho)\frac{1-y}{y}
\end{aligned}
\tag{3.90}
$$

and with $\beta_\tau = \sqrt{1-\rho/\tau}$.

3.6 The massless limit

In order to apply the GM-VFN scheme we have to take the massless limit of the result. In terms where the heavy quark mass acts as a regulator for collinear singularities - specifically where logarithms of the mass occur - we keep it. So the

massless limit here is not a limit in the strict mathematical sense and we write lim on both sides of the equation:

$$\begin{aligned}
\lim_{\rho\to 0} S_T^{(v)}(\rho) &= \lim_{\rho\to 0}\left(\ln^2\left(\frac{4}{\rho}\right)+\ln\left(\frac{4}{\rho}\right)+\pi^2-2\right), \qquad (3.91)\\
\lim_{\rho\to 0} S_L^{(v)}(\rho) &= 0,\\
\lim_{\rho\to 0} S_T^{(a)}(\rho) &= \lim_{\rho\to 0} S_T^{(v)}(\rho),\\
\lim_{\rho\to 0} S_L^{(a)}(\rho) &= 0
\end{aligned} \qquad (3.92)$$

which can be verified with the help of the equations

$$\begin{aligned}
\ln\left(\frac{1+\beta}{1-\beta}\right) &\to \ln\left(\frac{4}{\rho}\right), \qquad (3.93)\\
\mathrm{Li}_2\left(\frac{1-\beta}{1+\beta}\right) &\to 0,\\
\mathrm{Li}_2\left(\frac{4\beta}{(1+\beta)^2}\right) &\to \mathrm{Li}_2(1)=\frac{\pi^2}{6},\\
\mathrm{Li}_2\left(-\frac{4\beta}{(1-\beta)^2}\right) &= \mathrm{Li}_2\left(1-\frac{(1+\beta)^2}{(1-\beta)^2}\right)\\
&= -\mathrm{Li}_2\left(\frac{4\beta}{(1+\beta)^2}\right)-\frac{1}{2}\ln^2\left(\frac{(1+\beta)^2}{(1-\beta)^2}\right)\\
&\to -\mathrm{Li}_2(1)-2\ln^2\left(\frac{4}{\rho}\right)\\
&= -\frac{\pi^2}{6}-2\ln^2\left(\frac{4}{\rho}\right).
\end{aligned}$$

For the latter we used the identity

$$\mathrm{Li}_2(1-x)+\mathrm{Li}_2\left(1-x^{-1}\right)=-\frac{1}{2}\ln^2 x. \qquad (3.94)$$

For the real corrections the massless limit is more complicated. We have rewritten the result in terms of distributions to handle the poles at $y=1$. The mass ρ however has acted as a regulator for additional poles, which occur in the pure massless calculation. So when we take the massless limit we have to watch out for new poles in $y=1$. But first we take $\rho\to 0$ where this leaves the remaining expression finite. This simplifies the expressions to:

$$\begin{aligned}
\lim_{\rho\to 0} R_T^{(v)}(\rho) &= \lim_{\rho\to 0}\left(\frac{y}{2\sqrt{y^2-\rho}}\left(y^2-6y-2\right)+(y^2+1)\xi(y,\rho)\right),\\
\lim_{\rho\to 0} R_L^{(v)}(\rho) &= 1-y,\\
\lim_{\rho\to 0} R_T^{(a)}(\rho) &= \lim_{\rho\to 0} R_T^{(v)}(\rho),\\
\lim_{\rho\to 0} R_L^{(a)}(\rho) &= 1-y.
\end{aligned}$$

The square root in the denominator requires special attention, since the integrand diverges in $y = \sqrt{\rho}$ for the terms not proportional to ρ. While the integral is still finite, it leads to a false result if we take ρ to zero in that expression before integrating if that changes the divergence behavior. So we do this only in safe cases and then the result in the proper order is

$$\lim_{\rho\to 0}\int\limits_{\sqrt{\rho}}^{1}\frac{\mathrm{d}y}{(1-y)_+}\frac{y}{2\sqrt{y^2-\rho}}\left(y^2-6y-2\right)=\frac{1}{2}\ln\left(\frac{4}{\rho}\right)+\frac{7}{4}. \tag{3.95}$$

On the other hand we want to write the result after $\rho \to 0$. The integral then results in

$$\int\limits_{0}^{1}\mathrm{d}y\frac{y^2-6y-2}{2(1-y)_+}=\frac{9}{4}. \tag{3.96}$$

As a consequence we can write

$$\lim_{\rho\to 0}\frac{1}{(1-y)_+}\frac{y}{2\sqrt{y^2-\rho}}\left(y^2-6y-2\right)=\frac{y^2-6y-2}{2(1-y)_+}+\delta(1-y)\left(\frac{1}{2}\ln\left(\frac{4}{\rho}\right)-\frac{1}{2}\right). \tag{3.97}$$

For the remaining term we first simplify $\xi(y,\rho)$ for small ρ:

$$\begin{aligned}\ln\left(\frac{\rho-2y-2\sqrt{y^2-\rho}}{\rho-2y+2\sqrt{y^2-\rho}}\right) &= \ln\left(\frac{(\rho-2y-2\sqrt{y^2-\rho})^2}{(\rho-2y)^2-4(y^2-\rho)}\right) \\ &\to \ln\left(\frac{16y^2}{\rho(\rho+4(1-y))}\right).\end{aligned} \tag{3.98}$$

For the point $y = \sqrt{\rho}$ this approximation gives $\ln(4)$, while the correct result is 0. We have to work under an integral to have properly defined distributions. Since the difference is only finite and only occurs in one point, we can use the simpler expression and break down the logarithm into several terms:

$$\lim_{\rho\to 0}\int\limits_{\sqrt{\rho}}^{1}\mathrm{d}y\frac{1+y^2}{(1-y)_+}\xi(y,\rho) \tag{3.99}$$

$$= \lim_{\rho\to 0}\int\limits_{\sqrt{\rho}}^{1}\mathrm{d}y\left[\frac{1+y^2}{(1-y)_+}\ln\left(\frac{4}{\rho}\right)+\frac{1+y^2}{(1-y)_+}2\ln(y)+\frac{1+y^2}{(1-y)_+}\ln\left(\frac{4}{\rho+4(1-y)}\right)\right].$$

The first term is final. The second term is 0 for $y = 1$, therefore we can simply write $1/(1-y)$ instead of $1/(1-y)_+$. The third term is the most interesting. While $\rho > 0$ it is infrared-safe, but in the massless limit we get a $(\ln(1-y)/(1-y))_+$-pole. So we compare the following two integrals:

$$\begin{aligned}-\lim_{\rho\to 0}\int\limits_{\sqrt{\rho}}^{1}\frac{1+y^2}{(1-y)_+}\ln(\rho/4+1-y) &= -\ln^2\left(\frac{4}{\rho}\right)-\frac{7}{4}-\frac{\pi^2}{3}, \\ -\int\limits_{0}^{1}\mathrm{d}y(1+y^2)\left(\frac{\ln(1-y)}{1-y}\right) &= -\frac{7}{4}.\end{aligned} \tag{3.100}$$

So we can write

$$-\lim_{\rho\to 0}\frac{1+y^2}{(1-y)_+}\ln(\rho/4+1-y) = -(1+y^2)\left(\frac{\ln(1-y)}{1-y}\right)+\delta(1-y)\left(-\ln^2\left(\frac{4}{\rho}\right)-\frac{\pi^2}{3}\right). \tag{3.101}$$

The result including the longitudinal part is:

$$\begin{aligned}\lim_{\rho\to 0}\frac{R_T^{(u)}(y,\rho)+R_L^{(u)}(y,\rho)}{(1-y)_+} &= \left\{\delta(1-y)\left(-\ln^2\frac{4}{\rho}+\frac{1}{2}\ln\frac{4}{\rho}-\frac{1}{2}-\frac{\pi^2}{3}\right)\right.\\ &\quad+\left(\frac{1}{1-y}\right)_+\left[(1+y^2)\ln\frac{4}{\rho}-4y+\frac{y^2}{2}\right]\\ &\quad\left.-(1+y^2)\left[\frac{\ln(1-y)}{1-y}\right]_+ + 2\frac{1+y^2}{1-y}\ln y\right\}.\end{aligned} \tag{3.102}$$

The massless limit of the gluon coefficients (3.90) is simpler. We only need to know that

$$\begin{aligned}\ln\left(\frac{1+\beta_\tau}{1-\beta_\tau}\right) &= \ln\left(\frac{(1+\beta_\tau)^2}{1-\beta_\tau^2}\right) &(3.103)\\ &\to \ln\left(\frac{4(1-y)}{\rho}\right) &(3.104)\end{aligned}$$

and thus

$$\lim_{\rho\to 0}\left[G_T^{(u)}(y,\rho)+G_L^{(u)}(y,\rho)\right] = 2C_F\frac{1+(1-y)^2}{y}\left[\ln\frac{4}{\rho}+\ln(1-y)-1\right]. \tag{3.105}$$

3.7 Subtraction terms for GM-VFNS

We now list the result for the the NLO calculation in the $\overline{\rm MS}$ scheme cited from [54]. The result is required for the light quarks and for the calculation of the GM-VFNS subtraction terms. The respective cross sections for quark and for gluon production are given by

$$\begin{aligned}\frac{1}{\sigma_{\rm tot}}\frac{{\rm d}\sigma_{q_i}}{{\rm d}y}(y,\mu,\mu_f) &= \frac{V_{q_i}^2+A_{q_i}^2}{\sum_{j=1}^{n_f}\left(V_{q_j}^2+A_{q_j}^2\right)}\left\{\delta(1-y)+\frac{\alpha_s(\mu)}{2\pi}\left[P_{q\to q}^{(0,T)}(y)\ln\frac{s}{\mu_f^2}+C_q(y)\right]\right\},\\ \frac{1}{\sigma_{\rm tot}}\frac{{\rm d}\sigma_g}{{\rm d}y}(y,\mu,\mu_f) &= 2\frac{\alpha_s(\mu)}{2\pi}\left[P_{q\to g}^{(0,T)}(y)\ln\frac{s}{\mu_f^2}+C_g(y)\right].\end{aligned} \tag{3.106}$$

$P_{a\to b}^{(0,T)}$ are the LO timelike splitting functions

$$\begin{aligned}P_{q\to q}^{(0,T)}(y) &= C_F\left[\frac{3}{2}\delta(1-y)+\frac{1+y^2}{(1-y)_+}\right], &(3.107)\\ P_{q\to g}^{(0,T)}(y) &= C_F\frac{1+(1-y)^2}{y}.\end{aligned}$$

The coefficient functions read

$$\begin{aligned} C_q(y) &= C_F \left\{ \left(-\frac{9}{2} + \frac{2}{3}\pi^2 \right) \delta(1-y) - \frac{3}{2} \left(\frac{1}{1-y} \right)_+ + 2 \left[\frac{\ln(1-y)}{1-y} \right]_+ + \frac{5}{2} - \frac{3}{2} y \right. \\ &\quad \left. + 4 \frac{\ln y}{1-y} - (1+y)[2 \ln y + \ln(1-y)] \right\}, \qquad (3.108) \\ C_g(y) &= C_F \frac{1+(1-y)^2}{y} [2 \ln y + \ln(1-y)]. \end{aligned}$$

A comparison of this result with the massles limit (3.102) yields, that the latter can be written as:

$$\begin{aligned} &\lim_{\rho \to 0} \left\{ \delta(1-y) C_F \left[S_T^{(u)}(\rho) + S_L^{(u)}(\rho) \right] + \frac{R_T^{(u)}(y,\rho) + R_L^{(u)}(y,\rho)}{(1-y)_+} \right\} \qquad (3.109) \\ = \; & P_{q \to q}^{(0,T)}(y) \ln \frac{s}{\mu_f^2} + C_q(y) + d_q^{(1)}(y, \mu_f), \\ & \lim_{\rho \to 0} C_F \left[G_T^{(u)}(y,\rho) + G_L^{(u)}(y,\rho) \right] \\ = \; & 2 \left[P_{q \to g}^{(0,T)}(y) \ln \frac{s}{\mu_f^2} + C_g(y) \right] + d_g^{(1)}(y, \mu_f), \end{aligned}$$

where the functions $d_q^{(1)}(y, \mu_f)$ and $d_g^{(1)}(y, \mu_f)$ are

$$\begin{aligned} d_q^{(1)}(y, \mu_f) &= P_{q \to q}^{(0,T)}(y) \ln \frac{\mu_f^2}{m^2} \qquad (3.110) \\ &\quad + C_F (1+y^2) \left\{ \delta(1-y) - \left(\frac{1}{1-y} \right)_+ - 2 \left[\frac{\ln(1-y)}{1-y} \right]_+ \right\}, \\ d_g^{(1)}(y, \mu_f) &= 2 P_{q \to g}^{(0,T)}(y) \ln \frac{\mu_f^2}{m^2} - 2 C_F (2 \ln y + 1). \end{aligned}$$

We observe that the logarithms $\ln(s/\mu_f^2)$ and $\ln(\mu_f^2/m^2)$ combine in both expressions to $\ln(s/m^2)$, so that the subtraction terms do not depend on the factorization scale μ_f. We write them down as $C_q^{\mathrm{Sub}}(y)$ and $C_g^{\mathrm{Sub}}(y)$:

$$\begin{aligned} C_q^{\mathrm{Sub}}(y) &= P_{q \to q}^{(0,T)}(y) \ln \frac{s}{m^2} \qquad (3.111) \\ &\quad + C_F (1+y^2) \left\{ \delta(1-y) - \left(\frac{1}{1-y} \right)_+ - 2 \left[\frac{\ln(1-y)}{1-y} \right]_+ \right\}, \\ C_g^{\mathrm{Sub}}(y) &= 2 P_{q \to g}^{(0,T)}(y) \ln \frac{s}{m^2} - 2 C_F (2 \ln y + 1). \end{aligned}$$

With these results we have everything that we need for the parton cross section in the convolution integral (3.5). Only the fragmentation functions remian unknown. We are going to extract them from experimental data in the next chapter.

Chapter 4

Extraction of Fragmentation Functions

In this chapter we apply the theoretical result of chapter 3 to extract fragmentation functions (FFs) from the heavy hadron production in electron-positron-annihilation. In particular we use the cross section (3.81) with the coefficient functions (3.86) and (3.87) and the subtraction terms (3.111) for the GM-VFNS and the cited cross section (3.106) with the coefficients (3.109) for the ZM-VFNS for comparison. By fitting a set of parameters, which describe the shape of the FFs, to experimental data from the experiments Belle, CLEO, ALEPH and OPAL [25, 26, 21, 19, 20] we find FFs for D^0, D^+ and D^{*+} hadrons. The quality of the fits, measured with the chi-squared-function, is a first check for the theory. This is especially true for the global fit, where we use data sets at two different scales in one fit and therefore test the DGLAP evolution equations. The universality of the FFs will be used in chapter 5 to make predictions for other hadron production processes to.

4.1 Experimental data

Our first data sets are the results from the OPAL [19, 20] and the ALEPH [21] experiments, which were collected during the run of the Large Electron-Positron Collider (LEP1) at CERN. The data in question is from collisions at the Z-boson resonance $\sqrt{s} = m_Z = 91.2\,\mathrm{GeV}$. We find the data in the form of $1/N(Z \to \text{hadrons}) \times (\mathrm{d}N(H_c)/\mathrm{d}x)$, where N is the number of detected events. This accords to the normalized production cross section $1/\sigma_{\mathrm{tot}}(\mathrm{d}\sigma/\mathrm{d}x)$ for one of the hadrons $H_c = D^0, D^+, D^{*+}$ times the branching fraction of the decay channel which was used to identify the produced hadron. For the normalization we use

$$\sigma_{\mathrm{tot}} = N_c \sigma_0 \sum_{i=1}^{n_f} (V_{q_i}^2 + A_{q_i}^2) \left[1 + \frac{\alpha_s(\mu)}{2\pi} C_F \frac{3}{2} \right] \tag{4.1}$$

with σ_0 from eq.(3.82). Here we use the massless cross section, since the charm and bottom quark masses are negligible at the LEP1 scale.

For consistency, for each data set we adapt the values of the branching fractions which were used in the according publication. For the OPAL data sets the values are $B(D^0 \to K^-\pi^+) = (3.84 \pm 0.13)\%$ and $B(D^+ \to K^-\pi^+\pi^+) = (9.1 \pm 0.6)\%$ from [55] for data from [19], and $B(D^{*+} \to D^0\pi^+) = (68.3 \pm 1.4)\%$ and $B(D^0 \to K^-\pi^+) = (3.83 \pm 0.12)\%$ from [56] for data from [20]. For ALEPH [21] we use $B(D^{*+} \to D^0\pi^+) = (68.3 \pm 1.4)\%$ and $B(D^0 \to K^-\pi^+) = (3.85 \pm 0.09)\%$ from [57].

Both OPAL and ALEPH provide extra data for b-tagged events, which we use to enhance the differentiation between fragmentation functions of the b-quark and of the c-quark, which dominate the D-hadron production. In the case of the ALEPH data we have to multiply the b-tagged events with $R_b = \Gamma(Z \to b\bar{b})/\Gamma(Z \to \text{hadrons})$ - the fraction of the b-tagged events in the full hadronic sample - and $f(b \to D^{*+})$, the probability of a b quark to hadronize into a D^{*+} meson. We use the value $R_b f(b \to D^{*+}) = (4.66 \pm 0.51)\%$, which was determined in the ALEPH publication [21] together with the hadron production data.

The second sort of data is from the B-factory experiments Belle [25] and CLEO [26]. Both collaborations have collected electron-positron-annihilation events near the $\Upsilon(5S)$ resonance at $\sqrt{s} = 10.58\,\text{GeV}$ and present them in the form $\mathrm{d}\sigma/\mathrm{d}x_p$, where $x_p = |\vec{p}|/|\vec{p}|_{\max}$. The highest possible momentum is related to the maximum energy $\sqrt{s}/4$ by $|\vec{p}|_{\max} = \sqrt{s/4}\sqrt{1-\rho_H}$. While x runs from $\sqrt{\rho_H} \le x \le 1$, x_p takes values from 0 to 1. Near the production threshold x_p is more appropiate for meaningful plots. The conversion formulas between x and x_p read

$$\begin{aligned} x_p &= \sqrt{(x^2-\rho_H)/(1-\rho_H)} \\ x &= \sqrt{(1-\rho_H)x_p^2+\rho_H} \\ \frac{\mathrm{d}\sigma}{\mathrm{d}x_p} &= (1-\rho_H)\frac{x_p}{x}\frac{\mathrm{d}\sigma}{\mathrm{d}x}(x). \end{aligned} \tag{4.2}$$

The data from CLEO is analyzed for $\sqrt{s} = 10.55\,\text{GeV}$, where we use the data in the range of $0.20 < x_p < 0.95$. In the case of Belle we find seperate data for the continuum at $\sqrt{s} = 10.52\,\text{GeV}$ and directly on the resonance at $\sqrt{s} = 10.58\,\text{GeV}$, which is used to seperate contributions from fragmenting charm- and bottom-quarks. We only use the continuum data. Both Belle and CLEO provide their data with the b-quark contribution being subtracted, so we won't add them in the theory either when fitting. However the $b \to H_c$ FF will still have a small influence on the cross section through the evolution equations.

The used range of data is $0.08 < x_p < 0.94$. Since the data from the B-factories is not normalized with the total cross section, it depends on the squared running fine-structure constant α^2. At $\sqrt{s} = 10.52\,\text{GeV}$ we use the value $1/\alpha = 132$ [58].

4.2 Initial state radiation

The experimental data on inclusive single-hadron production in e^+e^- annihilation naturally contains electroweak corrections, which are not subtracted in the analysis. The largest correction stems from electromagnetic radiation coming from the incoming electrons and positrons, the initial state radiation (ISR). The ISR is suppressed by a factor of α, but enhanced by the logarithm $\ln(s/m_e^2)$, where $m_e = 511\,\text{keV}$ is the electron mass. At Belle and CLEO energies, the hadronic cross section decreases with increasing invariant mass of the hadronic system. ISR reduces the invariant mass, therefore the cross section is increased and the shape of the FFs is modified. The effect of ISR has been examined in [28] and found to be non-negligible for the analysis of Belle and CLEO data. In contrast the OPAL and ALEPH data has been taken at the Z resonance, which means that a loss of energy of the incoming leptons takes the invariant hadronic mass away from the resonance peak. Therefore we have good reason to assume that the effect is suppressed for the data from the LEP collider.

Unlike the procedure in [28], where the experimental data is modified in several iterations, we apply the ISR effects on the theory output, which is then fitted to the

experimental data. This is possible thanks to some approximations, which allow us to include the ISR effects into each theory curve during the fitting process to Belle and CLEO data without slowing the program down too much.

The dominant ISR corrections are incorporated with the help of the structure-function approach, in which the photon emission is taken to be collinear to the incoming leptons [59, 60]. With this assumption the ISR corrections can be treated in analogy to the collinear parton model. We call the ISR-corrected differential cross section $\mathrm{d}\sigma_{\mathrm{ISR}}(p_+, p_-)$, where the $p_\pm$ denote the four-momenta of the incoming positron and electron respectively. The corrected cross section is obtained by convoluting the uncorrected differential cross section $\mathrm{d}\sigma(p_+, p_-)$ with radiator functions $D_{e^\pm}(x_\pm, s)$, which measure the probability for the positron/electron to retain the fraction $x_\pm$ of its energy after photon emission. This convolution reads

$$\mathrm{d}\sigma_{\mathrm{ISR}}(p_+, p_-) = \int_0^1 \mathrm{d}x_+ \int_0^1 \mathrm{d}x_- D_{e^+}(x_+, s) D_{e^-}(x_-, s) \mathrm{d}\sigma(x_+ p_+, x_- p_-). \tag{4.3}$$

The radiator functions $D_{e^\pm}(x_\pm, s)$ contain the leading logarithms, which have been resummed using the method by Gribov and Lipatov [61]. The expression can be found in [60]. It is

$$\begin{aligned} D_{e^\pm}(x_\pm, s) &= \frac{1}{2}\tilde{\beta}(1-x)^{\tilde{\beta}/2-1}\Delta' - \frac{1}{4}(1+x)\tilde{\beta} \\ &\quad + \frac{1}{32}\tilde{\beta}^2\left((1+x)[-4\ln(1-x) + 3\ln x] - \frac{4}{1-x}\ln x - 5 - x\right) \end{aligned} \tag{4.4}$$

with $\tilde{\beta} = (2\alpha/\pi)(L-1)$, $L = \ln(s/m_e^2)$ and

$$\Delta' = 1 + \frac{3}{8}\tilde{\beta} + \mathcal{O}\left(\tilde{\beta}^2\right). \tag{4.5}$$

The structure-function approach was mostly applied to total cross sections in the literature. In this case, one integration can be carried out independently of the considered process and leads to the luminosity function

$$H(\tau, s) = \int_0^1 \mathrm{d}x_+ \int_0^1 \mathrm{d}x_- \delta(\tau - x_+ x_-) D_e(x_+, s) D_e(x_-, s). \tag{4.6}$$

with $\tau = x_+ x_-$.

An expression for $H(\tau, s)$ can also be found in [60] in terms of the variable $\chi = 1 - \tau$. Since it will be sufficient as an approximation we cite it here:

$$\begin{aligned} H(\chi, s) &= \Delta\tilde{\beta}\chi^{\tilde{\beta}-1} - \frac{1}{2}\tilde{\beta}(2-\chi) + \frac{1}{8}\tilde{\beta}^2\{(2-\chi)[3\ln(1-\chi) - 4\ln\chi] \\ &\quad -4[\ln(1-\chi)/\chi - 6 + \chi\} + \mathcal{O}\left(\tilde{\beta}^3\right), \end{aligned} \tag{4.7}$$

with

$$\begin{aligned} \Delta &= 1 + \frac{\alpha}{\pi}\left(\frac{3}{2}L + \frac{\pi^2}{3} - 2\right) \\ &\quad + \left(\frac{\alpha}{\pi}\right)^2\left\{\left[\frac{9}{8} - 2\zeta(2)\right]L^2 + \left[-\frac{45}{16} + \frac{11}{2}\zeta(2) + 3\zeta(3)\right]L - \frac{6}{5}[\zeta(2)]^2\right. \\ &\quad \left. -\frac{9}{2}\zeta(3) - 6\zeta(2)\ln 2 + \frac{3}{8}\zeta(2) + \frac{57}{12}\right\}. \end{aligned} \tag{4.8}$$

Since we need the cross section differential in x, we have to perform a Lorentz boost along the beam axis. We obtain from eq.(4.3) the formula

$$\begin{aligned}\frac{\mathrm{d}\sigma_{\mathrm{ISR}}}{\mathrm{d}x}(x,s) &= \int \mathrm{d}x_+\,\mathrm{d}x_-\,\mathrm{d}x'\,\mathrm{d}\cos\theta'\,\delta(x-x(x_+,x_-,x',\cos\theta'))D_e(x_+,s)D_e(x_-,s)\\ &\quad\times\frac{\mathrm{d}^2\sigma}{\mathrm{d}x'\,\mathrm{d}\cos\theta'}(x',\cos\theta',x_+x_-s),\end{aligned}\tag{4.9}$$

where the primed variables refer to the hadronic CMS. The result of chapter 3 is valid for the hadronic reference frame, while in experiment only the e^+e^- CMS can be observed. We reach the hadronic system through a Lorentz boost along the beam axis. The four-momenta of the leptons - neglecting their masses in the kinematics - after ISR are in the e^+e^- CMS

$$p_+ = \begin{pmatrix} x_+E_l \\ 0 \\ 0 \\ x_+E_l \end{pmatrix}, \quad p_- = \begin{pmatrix} x_-E_l \\ 0 \\ 0 \\ -x_-E_l \end{pmatrix},\tag{4.10}$$

with the energy E_l of the lepton in the laboratory frame before radiating a photon. We assume equal energies for both beams, otherwise we would have to perform another boost from the laboratory frame to the leptonic CMS.

After a Lorentz boost with velocity β_L and associated Lorentz factor $\gamma_L = 1/\sqrt{1-\beta_L^2}$ we have

$$p'_+ = \gamma_L x_+ E_l \begin{pmatrix} 1-\beta_L \\ 0 \\ 0 \\ 1-\beta_L \end{pmatrix}, \quad p'_- = \gamma_L x_- E_l \begin{pmatrix} 1+\beta_L \\ 0 \\ 0 \\ -1-\beta_L \end{pmatrix}.\tag{4.11}$$

We want to boost into the hadronic CMS, where the sum of the three-vectors is zero, so β_L has to fulfill the condition

$$x_+(1-\beta_L) + x_-(-1-\beta_L) = 0,\tag{4.12}$$

which leads to

$$\beta_L = \frac{x_+ - x_-}{x_+ + x_-}.\tag{4.13}$$

From this it follows that our observable x can be expressed in terms of the boost variables by

$$x(x_+,x_-,x',\cos\theta') = \gamma_L\left(\sqrt{\tau}x' + \beta_L\sqrt{\tau x'^2 - \rho_H}\cos\theta'\right).\tag{4.14}$$

We use the delta function to integrate out $\cos\theta'$. With the help of eq.(4.14) we find that

$$\begin{aligned}&\delta(x - x(x',x_+,x_-,\cos\theta'))\\ &= \frac{2}{|x_+-x_-|\sqrt{x'^2-\rho_H/\tau}}\,\delta\left(\cos\theta' - \frac{2x-(x_++x_-)x'}{(x_+-x_-)\sqrt{x'^2-\rho_H/\tau}}\right).\end{aligned}\tag{4.15}$$

We now need the integration boundaries for the other variables. From the condition $|\cos\theta'| \le 1$ and eq.(4.15) we can derive a quadratic equation for x_- at the integration boundaries

$$(4x'^2x_+^2 - 4xx'x_+ + \rho_H)x_-^2 + (-4xx'x_+^2 + 4x^2x_+ - 2\rho_H x_+)x_- + x_+^2\rho_H = 0.\tag{4.16}$$

This equation is symmetric under exchange of x_+ and x_-. We will use this fact below.

The solutions are with $a_\pm = (x \pm \sqrt{x^2 - \rho_H})/2$:

$$\begin{aligned} x_- &= -\frac{1}{8}\frac{1}{x_+x'(x'x_+ - x) + a_+a_-} \\ &\quad \times \left(4x_+(x(x - x'x_+) - 2a_+a_-) \pm \sqrt{16x_+^2(x - x_+x')^2(x^2 - \rho_H)}\right) \\ &= \frac{x_+}{2}\frac{1}{x_+x'(x - x_+x') + a_+a_-}\left(2a_\pm(x - x_+x') - 2a_+a_-\right) \\ &= a_\pm\frac{(x - x_+x') - a_\mp}{x'(x - x_+x') - \frac{a_+a_-}{x_+}} \\ &= a_\pm\frac{(x - x_+x') - a_\mp}{((x - x_+x') - a_\mp)\left(x' - \frac{a_\mp}{x_+}\right)} \\ &= \frac{a_\pm}{x' - \frac{a_\mp}{x_+}}. \end{aligned} \tag{4.17}$$

In the massless limit the solutions become x/x' and 0, therefore we can conclude that the valid range for x_- is

$$\frac{a_-}{x' - \frac{a_+}{x_+}} \leq x_- \leq \frac{a_+}{x' - \frac{a_-}{x_+}}. \tag{4.18}$$

Now we make use of the fact that eq.(4.16) is symmetric under exchange of x_- and x_+. If we integrate first over x_- and then over x_+, the lower integration boundary for x_+ become quite complicated due to the Lorentz transformation involved. Since the problem is symmetric, the same happens with the x_- boundaries when the integration over x_+ is the inner integral.

Therefore we split the integral into two parts for the cases $x_+ > x_-$ and $x_+ < x_-$ and integrate over the smaller variable first. Then the lower integration boundary for the respective outer integral is the situation where $x_+ = x_-$. In this case our boost velocity β_L is zero, and the only effect of ISR is the energy loss for the CM energy, which reads $x/x' = \sqrt{x_+x_-} = x_\pm$. One can check with the help of eq.(4.17) that, if $x_\pm > x_\mp$ and $x_\pm = x/x'$, then the upper bound for the $x_\mp$ integral becomes x/x', which satisifies the condition $x_\pm \geq x_\mp$.

The upper boundaries for the outer integrals are the obvious limits $x' \leq 1$ and $x_\pm \leq 1$. We just have to make sure that $x' \geq x$ in all cases. Without a Lorentz boost this is true, because then the relation is just $x' = \sqrt{\tau}x$ due to the definitions $x' = 2E'/\sqrt{\tau s}$ and $x = 2E/\sqrt{s}$ and $E' = E$. However with a Lorentz boost, whenever we boost against the flight direction of the hadron, we get $E > E'$.

So we check that $x' \geq x$ is true in that cases as well, which means that the energy loss due to the radiation of the photon always has a greater impact than the raise in the hadron energy due to a Lorentz transformation. We have to show $E\sqrt{\tau} \leq E'$. In the worst case the hadron's momentum is parallel to the axis and we boost in the opposite direction. In that case the Lorentz transformation for E' - still under the assumption that $x_+ > x_-$ - leads to:

$$\begin{aligned} E\sqrt{\tau} &\leq \gamma_L(E + \beta_L\sqrt{E^2 - m^2}) \\ E\sqrt{\tau} &\leq \frac{x_+ + x_-}{2\sqrt{\tau}}\left(E + \frac{x_+ - x_-}{x_+ + x_-}\sqrt{E^2 - m^2}\right) \end{aligned} \tag{4.19}$$

$$\begin{aligned} 1 &\leq \frac{x_+ + x_-}{2\tau}\left(1 + \frac{x_+ - x_-}{x_+ + x_-}\sqrt{1 - \frac{m^2}{E^2}}\right) \\ &= \frac{x_+}{2x_+x_-}\left(1 + \sqrt{1 - \frac{m^2}{E^2}}\right) + \frac{x_-}{2x_+x_-}\left(1 - \sqrt{1 - \frac{m^2}{E^2}}\right). \end{aligned}$$

The last expression is bigger than 1, because of

$$\begin{aligned} & \frac{x_+}{2x_+x_-}\left(1 + \sqrt{1 - \frac{m^2}{E^2}}\right) + \frac{x_-}{2x_+x_-}\left(1 - \sqrt{1 - \frac{m^2}{E^2}}\right) \qquad (4.20) \\ \geq\ & \frac{x_-}{2x_+x_-}\left(1 + \sqrt{1 - \frac{m^2}{E^2}}\right) + \frac{x_-}{2x_+x_-}\left(1 - \sqrt{1 - \frac{m^2}{E^2}}\right) \\ =\ & \frac{1}{x_+} \\ \geq\ & 1. \end{aligned}$$

The result is then

$$\begin{aligned} & \frac{\mathrm{d}\sigma_{\mathrm{ISR}}}{\mathrm{d}x}(x,s) \qquad (4.21) \\ =\ & \int_x^1 \mathrm{d}x' \left(\int_{x/x'}^1 \mathrm{d}x_+ \int_{a_-/(x'-a_+/x_+)}^{a_+/(x'-a_-/x_+)} \mathrm{d}x_- + \int_{x/x'}^1 \mathrm{d}x_- \int_{a_-/(x'-a_+/x_-)}^{a_+/(x'-a_-/x_-)} \mathrm{d}x_+ \right) \\ & \times \frac{D_{e^+}(x_+,s) D_{e^-}(x_-,s)}{|x_+ - x_-|\sqrt{x'^2 - \rho_H/\tau}} \frac{\mathrm{d}^2\sigma}{\mathrm{d}x'\,\mathrm{d}\cos\theta'}\left(x', \frac{2x - (x_+ + x_-)x'}{(x_+ - x_-)\sqrt{x'^2 - \rho_H/\tau}}, \tau s\right), \end{aligned}$$

where the boundaries have also been checked during run-time by having the program control that all integration variables are within their expected limits.

By numerical inspection in our specific application we find that we can safely use the substitution

$$D_{e^+}(x_+,s) D_{e^-}(x_-,s) \approx \delta(1 - x_+) H_{e^+e^-}(\tau, s). \qquad (4.22)$$

The reason of course is that there is a symmetry whether the electron or the positron emitts a photon and if one substitutes the angle $\theta' \to \pi - \theta'$ at the same time.

We further simplify eq.(4.22) by using an approximation for the dependence on the polar angle.

$$\begin{aligned} \frac{\mathrm{d}^2\sigma}{\mathrm{d}x'\,\mathrm{d}\cos\theta'}(x', \cos\theta', \tau s) &\approx \frac{3}{8}(1 + \cos^2\theta')\frac{\mathrm{d}\sigma}{\mathrm{d}x'}(x', \tau s) \qquad (4.23) \\ &\approx \frac{3}{8}(1 + \cos^2\theta')\frac{\sigma(\tau s)}{\sigma(s)}\frac{\mathrm{d}\sigma}{\mathrm{d}x'}(x', s). \end{aligned}$$

We justify the first line by pointing to eq.(3.3). The longitudinal component $\mathrm{d}\sigma^L/\mathrm{d}x$ is zero in the ZM approach and suppressed for $m^2 \ll s$. The asymmetric component disappears when integrating over $\cos\theta'$. The second line describes the leading power-like dependence on the CMS energy while neglecting the scaling violations of the FFs, which are just logarithmic. For the factor $\sigma(\tau s)/\sigma(s)$ we use the LO in the GM approach, but we neglect the contribution from Z-boson exchange which

is suppressed for $\sqrt{s} \ll m_Z$:

$$\frac{\sigma(\tau s)}{\sigma(s)} = \frac{1}{\tau}\,\frac{1+\rho/(2\tau)}{1+\rho/2}\sqrt{\frac{1-\rho/\tau}{1-\rho}}. \tag{4.24}$$

With these simplifications we get the working formula

$$\begin{aligned}\frac{\mathrm{d}\sigma_{\mathrm{ISR}}}{\mathrm{d}x}(x,s) &\approx \int_x^1 \mathrm{d}x'\,\frac{\mathrm{d}\sigma}{\mathrm{d}x'}(x',s) \\ &\times \int_{a_-/(x'-a_+)}^{a_+/(x'-a_-)} \mathrm{d}\tau\,\frac{2H_{e^+e^-}(\tau,s)}{(1-\tau)\sqrt{x'^2-\rho_H/\tau}}\,\frac{3}{8}(1+\cos^2\theta')\,\frac{\sigma(\tau s)}{\sigma(s)},\end{aligned} \tag{4.25}$$

which we inserted in our fit program as a correction for the CLEO and for the Belle data. When applying the ISR correction to the ZM approach, we set $\rho = 0$ in Eq.(4.24) for consistency.

We show the effect of ISR corrections on the distribution of $e^+ + e^- \to D^+ + X$ in Fig.(4.1), where the solid line shows the distribution after applying the ISR corrections on the slashed line. We observe that the initial state radiation shifts the spectrum to smaller values of x_p while increasing the maximum. This is expected since ISR reduces the available hadronic energy, which softens the spectrum and increases the cross section.

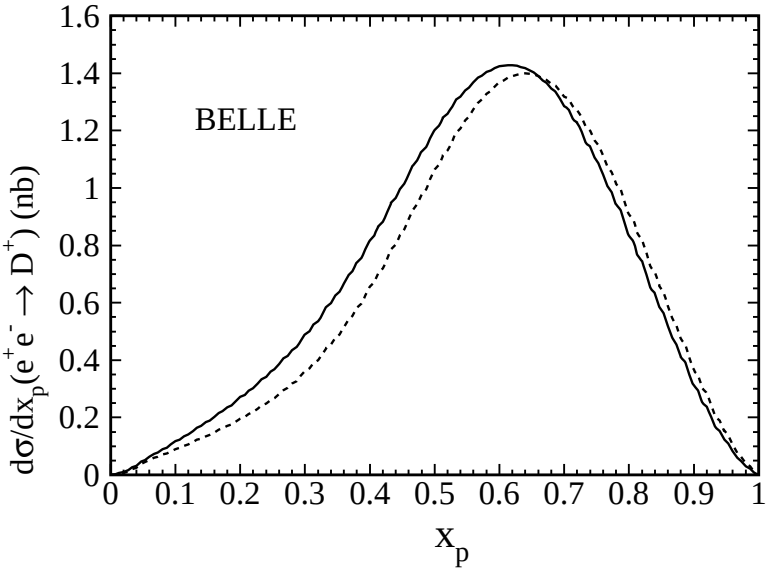

Figure 4.1: x_p distributions of D^+ production at $\sqrt{s} = 10.52\,\mathrm{GeV}$ from the fit to the Belle [25] and CLEO [26] data including ISR corrections (solid line) and corresponding result with the latter subtracted (dashed line).

4.3 Parametrization of fragmentation functions

We parametrize the c and b quark FFs as suggested by Bowler [62] at their respective starting scales m_c and m_b. This parametrization contains three parameters - the normalization N and a and γ in the form

$$D_Q^{H_c}(z, \mu_0) = N z^{-(1+\gamma^2)} (1-z)^a \mathrm{e}^{-\gamma^2/z}. \tag{4.26}$$

This parametrization yielded the best fit to Belle data in an analysis using the Monte Carlo event generator JETSET/PYTHIA [25], which contains several fragmentation models. The main difference is that we evolve our parametrization from the starting scale while it is common in experimental analyses to apply the parametrization directly at the experimental scale. However the evolution of the fragmentation function from $\mu_0 = 5\,\mathrm{GeV}$ to $\sqrt{s} = 10.52\,\mathrm{GeV}$ only has a mild influence on the form of the FFs function curve. We use a parameter γ instead of a parameter b times the transversal mass $m_\perp$ squared since the polar angle is already integrated out in the partonic part of our convolution integral.

The Bowler parametrization is a refinement of the similar parametrization of the Lund group [63]. Both parametrizations model fragmentation as an initial produced pair of a quark and an antiquark. The two particles are connected by a string of colour, which is cut by a pair of a light quark and antiquark from the vacuum. In the end two jets are produced, each one containing one particle of the original heavy pair. Bowler refines the method how the colour string is cut following a model formulated by Artru and Mennessier [64] and succeeds to conform with Bjorken [65], who predicted on general grounds that heavy hadrons retain a fraction of $1 - 1\,\mathrm{GeV}/m_Q$ of the original heavy quark's momentum. This translates into the FFs having their peak at that momentum fraction.

For comparison we tested the Lund parametrizations as well as the common Peterson parametrization [66] and the power ansatz both used for older fits to the LEP data [22]. Bowler proved far superior to the latter two parametrizations to fit to the Belle and CLEO data, which is not surprising since it was formulated with heavy quarks in mind, and is still a clear improvement over the Lund parametrization. Modifying Bowler by adding another parameter in different ways hardly improved the fit, which shows the accuracy of the modelling.

4.4 Implementation

The fit procedure has been implemented in the programming language FORTRAN. The heart of the program is the chi-squared function:

$$\chi^2(N_c, a_c, \gamma_c, N_b, a_b, \gamma_b) = \sum_{i=1}^{k} \left(\frac{(\mathrm{d}\sigma/\mathrm{d}x)_{\mathrm{exp},i} - (\mathrm{d}\sigma/\mathrm{d}x)_{\mathrm{th},i}(N_c, a_c, \gamma_c, N_b, a_b, \gamma_b)}{\Delta(\mathrm{d}\sigma/\mathrm{d}x)_{\mathrm{exp},i}} \right)^2. \tag{4.27}$$

Here we sum over the k bins of the experimental data $(\mathrm{d}\sigma/\mathrm{d}x)_{\mathrm{exp},i}$, where $\Delta(\mathrm{d}\sigma/\mathrm{d}x)_{\mathrm{exp},i}$ is the error of that value. We compare that number with our theoretical prediction for that bin $(\mathrm{d}\sigma/\mathrm{d}x)_{\mathrm{th},i}(N_c, a_c, \gamma_c, N_b, a_b, \gamma_b)$, which has to be integrated over the x range of the bin and depends on the parameters of the FFs. We find the set of parameters, where the function has its global minimum, with the help of the MINUIT library [67].

Our program first loads an input file, which contains the names of the files with the experimental data and the starting parameters for the FFs. After the data is loaded, the parameters of MINUIT are set. This includes the starting parameters for the FFs, which may be fixed depending on the current fit, and optionally limits

for the parameters. Then the chi-squared function is given to MINUIT, which will attempt to find the minimum in a limited number of calls of the chi-squared function by variations of the parameters. Typically one has to restart the program with the result of the last run several times, before the minimization processes converges. Also we have to restart the fit with completely different parameters to check that MINUIT has not converged in a local minimum. If the parameters wander off into absurd regions (like negative normalization) one can set limits for the parameters, however it is not advised to do so without need since MINUIT applies a mapping on the parameter in question. This mapping can disturb the convergence of the algorithm.

In the chi square function, the FFs are set according to the input parameters provided by MINUIT and evolved numerically according to the DGLAP equations. After that the program calculates the convolution integral (3.5). The parton cross section (3.81) contains distributions, as we can see in eq.(3.83). For the actual implementation we use the definition of the plus distribution (2.13):

$$\begin{aligned}\frac{\mathrm{d}\sigma}{\mathrm{d}x} &= \int\limits_{y_{\min}}^{1} \frac{\mathrm{d}y}{y} f(y) D(x/y) \left(\frac{1}{1-y}\right)_+ \qquad (4.28)\\ &= \int\limits_{y_{\min}}^{1} \mathrm{d}y \frac{\frac{f(y)}{y} D(x/y) - f(1)D(x)}{1-y} - f(1)D(x) \int\limits_{0}^{y_{\min}} \frac{\mathrm{d}y}{1-y}\\ &= \int\limits_{y_{\min}}^{1} \mathrm{d}y \frac{\frac{f(y)}{y} D(x/y) - f(1)D(x)}{1-y} + f(1)D(x)\ln(1-y_{\min}).\end{aligned}$$

The terms proportional to $(\ln(1-x)/(1-x))_+$ (occuring in the subtraction terms) are treated in an analogue way. The version for the delta distributions is trivial. The remaining integrations are calculated numerically with a Gaussian integration routine.

The prediction for the Belle and the CLEO data is then corrected for ISR. For the multi-dimensional integration in the ISR integral (4.25) we use the Vegas algorithm from the CUBA library [68].

4.5 Fit results

For each hadron species (D^0, D^+ and D^{*+}) we perform a combined fit to all available data sets (Belle, CLEO, ALEPH and OPAL), which we call the global fit. Furthermore we run a seperate fit to the B-factory (Belle/CLEO) data sets and to the OPAL data (ALEPH and OPAL combined for D^{*+}) respectively. All fits are executed in the GM-VFNS with heavy quark and hadron masses and for comparison a second time in the massless approach.

We summarize the values for fixed parameters in the following paragraph. We start at the initial scale $\mu_f = m_c = 1.5\,\mathrm{GeV}$, where the c-quark FF is set according to the Bowler parametrization. The parameters of the parametrization are chosen by the user in the first step and subsequently altered by the MINUIT routine for each step to find the set of parameters which minimizes $\overline{\chi^2}$, that is χ^2 divided by the number of data points. The remaining FFs start with zero. The FFs are then evolved with $n_f = 4$ active quark flavors. We switch to $n_f = 5$ at the threshold value $\mu_f = m_b = 5.0\,\mathrm{GeV}$. The FFs are evolved according to DGLAP to the appropiate scale $\mu_f = \sqrt{s}$ depending on the data set. For the global fit this procedure is repeated for each scale where we have at least one set of data available.

Table 4.1: Values of fit parameters for the D^0 meson resulting from the Belle, CLEO, OPAL, and global fits in the GM approach together with the values of $\overline{\chi^2}$ achieved.

	Belle+CLEO-GM	OPAL-GM	global-GM
N_c	$1.51 \cdot 10^7$	$4.42 \cdot 10^4$	$8.80 \cdot 10^6$
a_c	1.56	1.52	1.54
γ_c	3.64	2.83	3.58
N_b	13.5	13.5	78.5
a_b	3.98	3.98	5.76
γ_b	0.921	0.921	1.14
$\overline{\chi^2}$	3.15	0.794	4.03

Table 4.2: Values of fit parameters for the D^+ meson resulting from the Belle, CLEO, OPAL, and global fits in the GM approach together with the values of $\overline{\chi^2}$ achieved.

	Belle+CLEO-GM	OPAL-GM	global-GM
N_c	$5.66 \cdot 10^5$	$2.82 \cdot 10^4$	$5.67 \cdot 10^5$
a_c	1.15	1.49	1.16
γ_c	3.39	2.92	3.39
N_b	18.8	18.8	185
a_b	4.71	4.71	7.08
γ_b	1.17	1.17	1.42
$\overline{\chi^2}$	1.30	0.509	1.99

We find that the value $\Lambda^{(4)}_{\overline{\text{MS}}}$ has only a small impact on the fit result and is therefore, if used as an additional fit parameter, only weakly constrained. We therefore adopt the value $\Lambda^{(5)}_{\overline{\text{MS}}} = 221\,\text{MeV}$ from Ref.[70] and match $\Lambda^{(4)}_{\overline{\text{MS}}}$ accordingly to $\Lambda^{(4)}_{\overline{\text{MS}}} = 321\,\text{MeV}$ with the help of [69]. The masses of the hadrons are $m_{D^0} = 1.86\,\text{GeV}$, $m_{D^+} = 1.87\,\text{GeV}$ and $m_{D^{*+}} = 2.01\,\text{GeV}$ [70].

We start with fits at one scale. In the Belle/CLEO data, all charmed hadrons coming from B-meson decay are excluded. Therefore we don't add the contribution from b-quarks which fragment into D-mesons. But we still want the $D_b^{H_c}$ fragmentation function to take part in the DGLAP evolution, since it influences the form of the remaining FFs. Therefore we start with the LEP data and use the result for the $b \to H_c$ fragmentation as input for the Belle/CLEO fits. However the parameters for the b-quark FFs get fixed for the B-factory data, since the influence through the evolution is rather small and the parameters are barely constrained by the fit.

For LEP we have two sets of data per experiment and particle sort: In addition to each sum over all partons we have a b-tagged data set, which contains only the events stemming from a $Z \to b\bar{b}$ decay before fragmentation. The latter set is fitted to the appropiate theory curve, in which only the b contribution is used.

For the global fit the parameters of the c and b fragmentation functions are free fit parameters. Of course the result for the $b \to H_c$ fragmentation will be dominated by the LEP data set, while the Belle data has the biggest influence on the other FFs. We present the resulting parameters together with the value of $\overline{\chi^2}$ achieved in Tables 4.1 to 4.3.

Table 4.3: Values of fit parameters for the D^{*+} meson resulting from the Belle+CLEO, ALEPH+OPAL, and global fits in the GM approach together with the values of $\overline{\chi^2}$ achieved.

	Belle+CLEO-GM	ALEPH+OPAL-GM	global-GM
N_c	$1.33 \cdot 10^7$	$4.58 \cdot 10^4$	$1.10 \cdot 10^7$
a_c	0.992	1.38	1.07
γ_c	3.84	3.00	3.81
N_b	6.67	6.67	14.0
a_b	3.28	3.28	3.85
γ_b	1.04	1.04	1.14
$\overline{\chi^2}$	3.74	2.06	6.90

4.6 Discussion of results

Fig.4.2 shows the fits to LEP data graphically. We observe in Fig.4.2(c) that the D^{*+} data sets from ALEPH and OPAL are only moderately compatible. This explains the larger value of $\overline{\chi^2}$ compared to the values for D^0 and D^+. Apart from this problem theory and experiment are compatible.

We present the fits to the data from the B factories in Fig.4.3. In all cases the theory curve does not match the data distribution completely. The theory prediction is too high for small x_p values up to approximately $x_p < 0.35$, before being too low by up to one σ. The maximum of the theory curve is shifted slightly to higher x_p values. One could say that the fit is not able to produce a steep enough curve to match the data perfectly. Still the fits are acceptable, especially the D^+ fit achieves a good $\overline{\chi^2}$ value.

And finally Figs.4.4 to 4.6 contain the global fits with two plots for each hadron, one for Belle and CLEO data and one for OPAL and ALEPH data. Due to the precision of the Belle data, it dominates the fit except for the $b \to H_c$ fragmentation. We can see that for LEP data the charm contribution is too high, which is the main reason for the higher $\overline{\chi^2}$ value. It is possible that the data sets are not completely compatible. In Ref.[28] the fragmentation functions were allowed to have different normalizations thus correcting possible systematic differences in the experimental results. However that method ruins the global fits as a check for the FF evolution. Also in Ref.[28] it was speculated that non-perturbative power corrections are the source of the problem.

We have repeated the fits in the ZM approach for comparison. We set $m_c = m_b = 0$ except in the definition of the starting scale μ_0. We still have $m_H \neq 0$, so that the x distributions have finite lower endpoints. The results are presented in Tables (4.4) to (4.6). The comparison of the fit results in the GM-VFNS and in the ZM approach shows that the inclusion of finite quark masses reduces the χ^2 values of the global fits by $11 - 16\%$. The fit result for the Belle/CLEO fits is slightly better with quark masses for the D^0 and the D^+ with a $3 - 5\%$ lower $\overline{\chi^2}$, while it is $1 - 2\%$ higher for the D^{*+}. The latter differences are small enough that conclusions should be drawn with care. As expected the ALEPH/OPAL fits are practically unaffected by the quark masses.

From the comparison of the fit parameters it is hard to judge how much the FFs differ. In order to compare the GM and ZM approaches, we plot the fragmentation functions of the $c \to D^+$ and the $g \to D^+$ fragmentation as functions of z in the GM and in the ZM approach in Fig. 4.7. We find only a little difference between the GM and ZM results. In order to see the impact of the differences of the FFs,

Table 4.4: Values of fit parameters for the D^0 meson resulting from the Belle, OPAL, and global fits in the ZM approach together with the values of $\overline{\chi^2}$ achieved.

	Belle+CLEO-ZM	OPAL-ZM	global-ZM
N_c	$1.03 \cdot 10^7$	$3.43 \cdot 10^4$	$1.04 \cdot 10^7$
a_c	1.48	1.48	1.50
γ_c	3.60	2.80	3.60
N_b	13.4	13.4	80.8
a_b	3.96	3.96	5.77
γ_b	0.923	0.923	1.15
$\overline{\chi^2}$	3.25	0.789	4.66

Table 4.5: Values of fit parameters for the D^+ meson resulting from the Belle, OPAL, and global fits in the ZM approach together with the values of $\overline{\chi^2}$ achieved.

	Belle+CLEO-ZM	OPAL-ZM	global-ZM
N_c	$7.30 \cdot 10^5$	$2.62 \cdot 10^4$	$7.31 \cdot 10^5$
a_c	1.12	1.48	1.13
γ_c	3.43	2.91	3.43
N_b	19.0	19.0	163
a_b	4.71	4.71	6.93
γ_b	1.17	1.17	1.40
$\overline{\chi^2}$	1.37	0.507	2.21

Table 4.6: Values of fit parameters for the D^{*+} meson resulting from the Belle, ALEPH, OPAL, and global fits in the ZM approach together with the values of $\overline{\chi^2}$ achieved.

	Belle+CLEO-ZM	ALEPH+OPAL-ZM	global-ZM
N_c	$1.05 \cdot 10^7$	$2.80 \cdot 10^4$	$1.14 \cdot 10^7$
a_c	0.929	1.33	1.03
γ_c	3.82	2.93	3.82
N_b	6.52	6.52	14.9
a_b	3.25	3.25	3.87
γ_b	1.04	1.04	1.16
$\overline{\chi^2}$	3.69	2.04	7.64

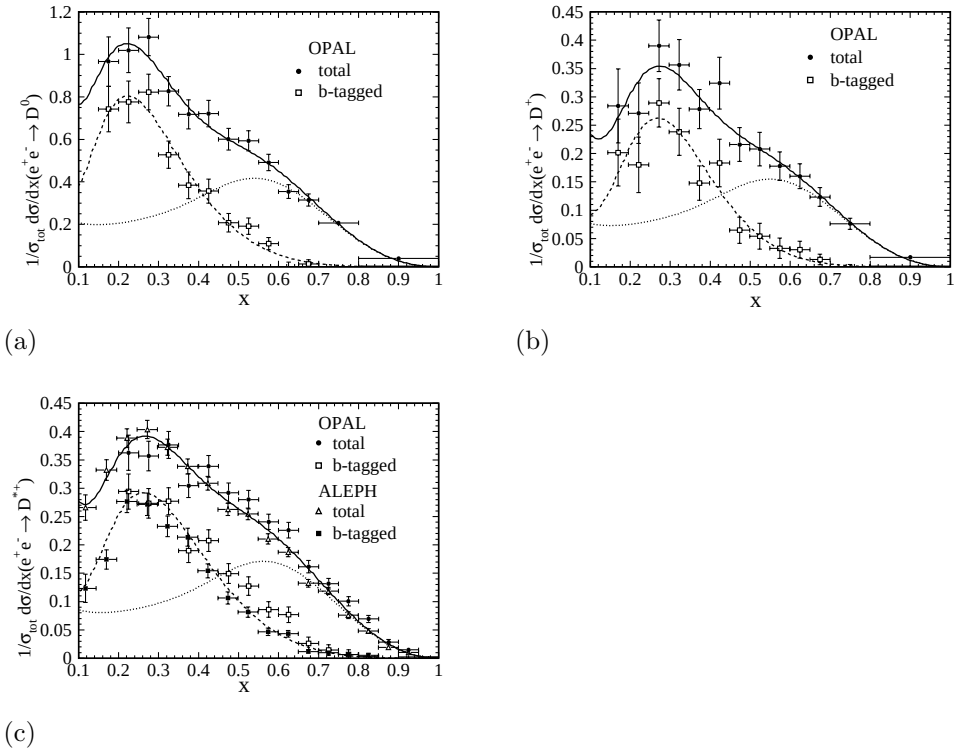

Figure 4.2: x_p distributions of (a) D^0, (b) D^+, and (c) D^{*+} mesons from OPAL [19] and ALEPH [21] compared to the respective fits in the GM approach from Tables 4.1–4.3. The dotted, dashed, and solid lines refer to the c-quark-initiated, b-quark-initiated, and total contributions, respectively. In frame (c), the D^{*+} data from OPAL [20] are included for comparison.

we convolute the ZM parton sections with the GM FFs in Fig. 4.8 and plot the result together with the proper GM-VFNS result. It turns out that the finite-m_c correction to the hard-scattering correction only amounts to a few percent. A similar observation was made in [71] using perturbative FFs [5].

For further comparisons we study the impact of the finite-m_H correction. We repeat the Belle/CLEO-ZM fit for the D^+ meson with $m_H = 0$. This requires some special measures. First of all $m_H = 0$ implies $x = x_p$. The fit works very badly for low x_p values, therefore we exclude the six data bins with $x_p < 0.2$ to get an acceptable fit to the more interesting part of the distribution. Furthermore we introduce the condition $\tau > \rho_{D^+}$ in the ISR correction (4.25), in which ρ_{D^+} is put to 0 otherwise, to ensure that the hadronic energy after ISR is above the production threshold. The resulting $c \to D^+$ and $g \to D^+$ FFs are also shown in Figs. 4.7. We immediately see a clear difference. The peak of the $c \to D^+$ FF is reduced significantly and shifted to a lower value of z. The $g \to D^+$ FF is only moderately affected. As expected we find a reciprocal change in the line shape of the x_p distribution in Fig. 4.8, where the peak position and height are substantially increased. The situation is similar for the D^0 and D^{*+} mesons.

In Fig. 4.9 we compare our new FF for the D^+ meson to the FFs from [23] and [24]. The fits from the two latter works are extracted from LEP data only. Therefore it is not surprising that our new FF with the Bowler parametrization gives a better description near the production threshold. The main difference between [23] and

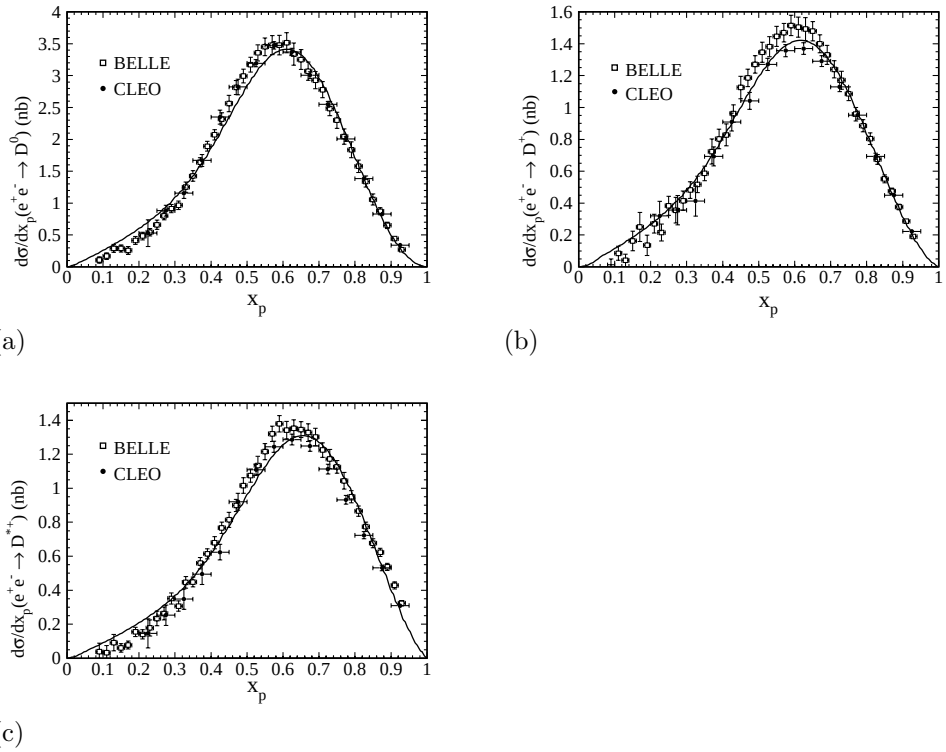

Figure 4.3: x_p distributions of (a) D^0, (b) D^+, and (c) D^{*+} mesons from Belle [25] compared to the respective fits in the GM approach from Tables 4.1–4.3.

[24] is the choice of the flavor threshold. While in [24] n_f is increased at the quark masses like in this work, in [23] the flavor thresholds are $2m_q$. This explains the difference between the dashed and the dotted line. The dotted line has barely been influenced by the evolution equations, which is especially visible for the $g \to D^+$ FF.

Besides the $c \to H_c$ and $b \to H_c$ themselves, another object of interest are their first two moments. The first moment corresponds to the branching fraction

$$B_Q(\mu_f) = \int\limits_{\max(\sqrt{\rho_H}, z_{\rm cut})}^{1} \mathrm{d}z\, D_Q(z, \mu_f), \tag{4.29}$$

with the heavy quark $Q = c, b$. The second moment corresponds to the average fraction of energy that the meson H_c receives from the quark:

$$\langle z \rangle_Q(\mu_f) = \frac{1}{B_Q(\mu_f)} \int\limits_{\max(\sqrt{\rho_H}, z_{\rm cut})}^{1} \mathrm{d}z z\, D_Q(z, \mu_f). \tag{4.30}$$

The value $z_{\rm cut} = 0.1$ excludes for ALEPH and OPAL data the problematic z range where our formalism is not valid. At that range there is no experimental data either. For BELLE and CLEO the lower integration limit is quite high with $\sqrt{\rho_H} \approx 0.4$, which we have to keep in mind. We have collected the values of $B_Q(\mu_f)$ and $\langle z \rangle_Q(\mu_f)$ for $Q = c$ at $\mu_f = 10.52\,\mathrm{GeV}$ and $\mu_f = m_Z$, and for $Q = b$ at $\mu_f = 2m_b$ and $\mu_f = m_Z$ in Tables 4.7 and 4.8. We give the values for all fits, which means for

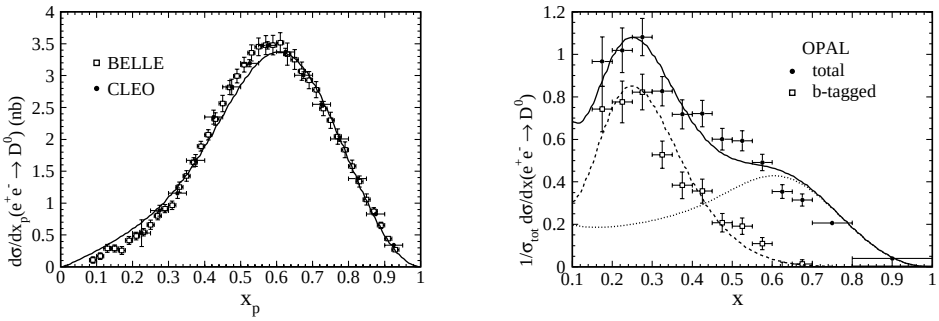

(a) (b)

Figure 4.4: x_p distributions of D^0 mesons from (a) Belle [25], CLEO [26], and (b) OPAL [19] compared to the global fit from Table 4.1. In frame (b), the dotted, dashed, and solid lines refer to the c-quark-initiated, b-quark-initiated, and total contributions, respectively.

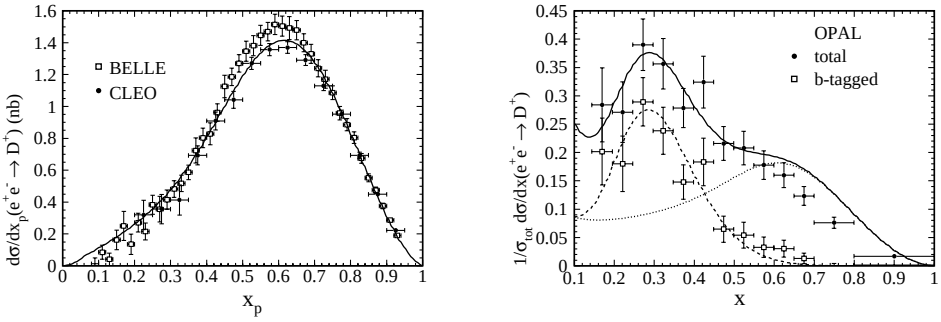

(a) (b)

Figure 4.5: x_p distributions of D^+ mesons from (a) Belle [25], CLEO [26], and (b) OPAL [19] compared to the global fit from Table 4.2. In frame (b), the dotted, dashed, and solid lines refer to the c-quark-initiated, b-quark-initiated, and total contributions, respectively.

the Belle/CELO-fits, for the ALEPH/OPAL-fits and for the global fits in the GM and in the ZM approach respectively.

We observe from Table 4.7 that regardless of the approach the values of $B_c(\mu_f)$ from ALEPH/OPAL fits are smaller than those from the Belle/CLEO fits. The difference is less than 10% for the D^0 and D^{*+} mesons and approximately 20% for the D^+ meson. The corresponding results from the global fits lie between both results, but more towards the Belle/CLEO data, which can be expected due to the bigger and more precise data set. The GM and the ZM approach both yield similar results. In the case of the $B_b(\mu_f)$ the differences between the three fits and the two approaches are minor. We remember that the $b \to H_c$ fragmentation function is mostly evaluated from the LEP data and in the case of the BELLE/CLEO data taken directly from the ALEPH/OPAL fit.

Also from Table 4.7 we find that it is fruitless to compare the branching fractions from one fit at different scales. The evolution should have little effect on the branching fractions, but due to the hadron mass we have introduced the lower inte-

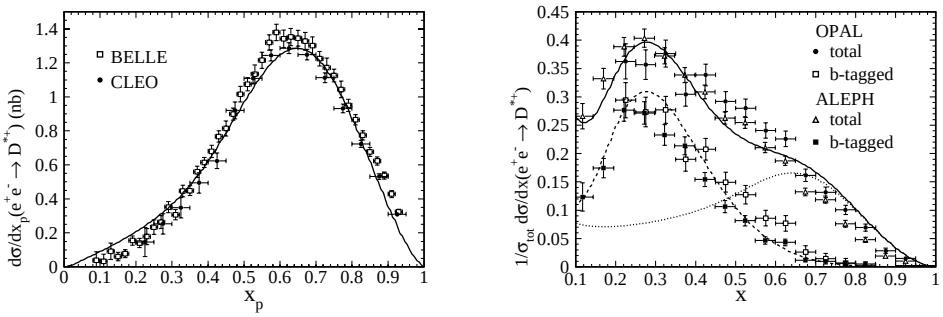

(a) (b)

Figure 4.6: x_p distributions of D^{*+} mesons from (a) Belle [25], CLEO [26], (b) ALEPH [21], and OPAL [20] compared to the global fit from Table 4.3. In frame (b), the dotted, dashed, and solid lines refer to the c-quark-initiated, b-quark-initiated, and total contributions, respectively.

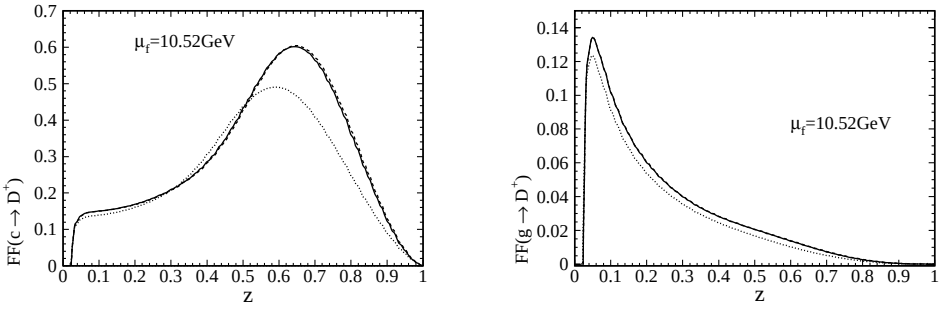

(a) (b)

Figure 4.7: (a) $c \to D^+$ and (b) $g \to D^+$ FFs of the Belle/CLEO fits at $\mu_f = 10.52\,\text{GeV}$ as functions of z in the GM approach (solid lines) and in the ZM approaches with $m_H \neq 0$ (dashed lines) and $m_H = 0$ (dotted lines).

gration limit. It seems that at $\sqrt{s} \approx 10\,\text{GeV}$ this limit cuts away important parts of the fragmentation function, especially for $b \to H_c$. As a result $B_b(2m_b)$ is typically around four times smaller than $B_b(m_Z)$. The FF for $c \to H_c$ loses only $\sim 20\%$, which can be explained by the fact that the $c \to H_c$ FFs have their peaks at higher values as we will see in Table 4.8. We have to conclude that parts of the FF, which are kinematically forbidden near the production threshold, contain important parts for the evolution to higher scales. Or as a second possibility one might want to keep in mind, that fit algorithms in multi-scale fits might use the part of the FF, which doesn't contribute at a low scale, to improve the fit at higher scales without physical justification. The latter possibility is however limited by the parametrization of the FFs, in our case Bowler.

Looking at Table 4.8, we see that the values of $\langle z \rangle_c(\mu_f)$ are shifted towards smaller values through the DGLAP evolution in μ_f. The quark-mass effects turn out to be insignificant here. The values of $\langle z \rangle_c(\mu_f)$ from the ALPEH/OPAL fits fall below $5 - 9\%$ below those from the Belle/CLEO fits. Again the values from the global fits very close to the Belle/CLEO results, but slightly shifted towards

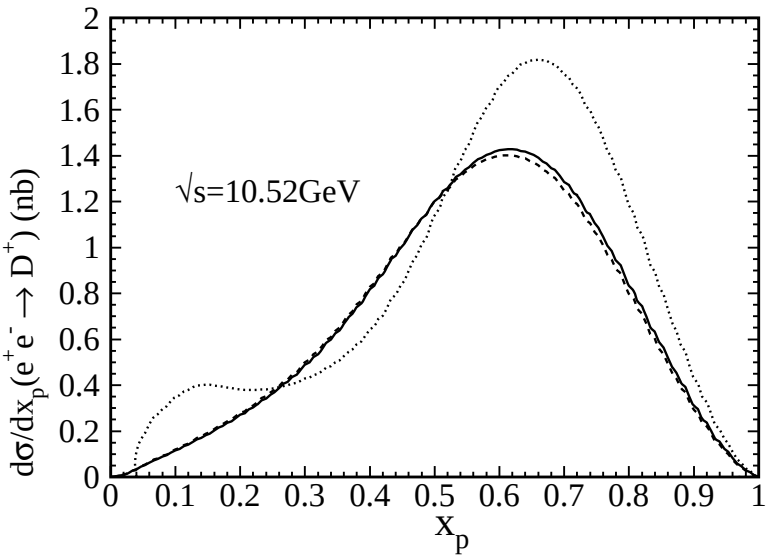

Figure 4.8: x_p distributions of $e^+e^- \to D^+ + X$ at $\sqrt{10.52}\,\mathrm{GeV}$ in the GM approach (solid line) and in the ZM approaches with $m_H \neq 0$ (dashed lines) and $m_H = 0$ (dotted lines), all valuated with the FFs from the Belle/CLEO-GM fit.

the ALEPH/OPAL results. This is also visible in the plots of the cross sections (Figs.4.4 to 4.6). For $\langle z \rangle_c(\mu_f)$ the differences between the various fits are marginal.

We point out that the fragmentation functions and their moments, while useful for a quick comparison with other FFs, are non-physical quantities which depend on scale, scheme, order, parametrization and initial scale. Nevertheless a comparison of our values of $B_Q(\mu_f)$ and $\langle z \rangle_Q(\mu_f)$ to the corresponding results from measured x distributions might be interesting. We cite the results from the experimental analysis in the Tables 4.9, 4.10 and 4.11. For a more direct comparison we also list the values of $B_Q(\mu_f)$ and $\langle z \rangle_Q(\mu_f)$, that are calculated from our theoretical predictions of the differential cross sections.

First we compare the branching fractions and the average energy from our fragmentation functions in Tables 4.7 and 4.8 with the ones from our actual cross sections in Tables 4.9, 4.10 and 4.11. In LO the two quantities are directly proportional, in our case the cross section is shifted due to NLO effects and the ISR correction. We find that the branching fractions at the scale $\mu_f = m_Z$ are higher by approximately 3% when calculated from the cross sections. We expect the ISR correction to lower these values, so the remaining NLO corrections must lead to an increase. The final difference is rather small, which justifies the usual direct comparison of values from the FFs to experimental values from measured cross sections.

The average energy fraction passed is also higher when coming from the observable cross section. At the b-factory scale we observe a difference of 2%, which seems acceptable. At the LEP scale the difference is higher at approximately 5%. Therefore we can conclude that in our approach branching fractions and average energy fractions passed to the hadron derived from the observable cross section are overestimated by a few percents compared to their theoretical counterparts in the fragmentation.

Table 4.7: Values of $c \to H_c$ and $b \to H_c$ branching fractions at $\mu_f = 2m_b$, 10.52 GeV and m_Z.

FF set	H_c	$B_c(10.52\,\text{GeV})$	$B_c(m_Z)$	$B_b(2m_b)$	$B_b(m_Z)$
Belle/CLEO-GM	D^0	0.525	0.611	0.146	0.492
	D^+	0.232	0.269	0.0590	0.168
	D^{*+}	0.211	0.249	0.0696	0.206
ALEPH/OPAL-GM	D^0	0.493	0.591	0.146	0.491
	D^+	0.185	0.220	0.0590	0.167
	D^{*+}	0.200	0.247	0.0695	0.206
global-GM	D^0	0.522	0.608	0.140	0.490
	D^+	0.230	0.268	0.0512	0.157
	D^{*+}	0.206	0.245	0.0716	0.212
Belle/CLEO-ZM	D^0	0.534	0.622	0.146	0.490
	D^+	0.235	0.273	0.0592	0.167
	D^{*+}	0.215	0.254	0.0695	0.205
ALEPH/OPAL-ZM	D^0	0.489	0.587	0.146	0.489
	D^+	0.185	0.221	0.0591	0.166
	D^{*+}	0.201	0.248	0.0694	0.204
global-ZM	D^0	0.527	0.614	0.141	0.488
	D^+	0.234	0.272	0.0517	0.157
	D^{*+}	0.209	0.248	0.0718	0.210

We now take a look at the available branching fractions from the experiments in Table 4.9. We only have values for OPAL and ALEPH. For the latter the publication [21] contains branching fractions for the D^0 and D^+ despite the lack of x distributions. Looking at the theoretical values from the global fit, we find that the theory predictions are substantially higher in the range of $10-20\%$ and even over 25% for the only $b \to D$ value available. The overestimation of the c contribution for high x values has already been seen in Figs. 4.4 to 4.6. However the high value for $b \to D^{*+}$ cannot be explained by the influence of Belle data. By looking at Fig. 4.6 we observe that the b-tagged ALEPH data is incompatible to the b-tagged OPAL data and much higher in the range $0.4 < x < 0.7$. For last three bins it's almost a factor of 2. This can very well be the reason for the discrepancy between the branching fraction from the fitted theory and from the experimental data.

Finally we take a look at the average energy passed from the c quark to the D meson. In Table 4.10 we compare the values for Belle and CLEO and our theory value. The theory values are lower by approximately $1\%-3\%$, which is outside the rather small error margins of the experimental values.

The values for ALPEH, OPAL and the matching theory value from the global fit are listed in Table 4.11. Here the theory values are too high by up to 5% for the OPAL data. So the shift of the theory data during the evolution from $\sqrt{s} = 10.52\,\text{GeV}$ to $\sqrt{s} = m_Z$ is a too high, but to a rather small degree. The discrepancy between theory and the ALEPH value is higher (almost 10%), but the ALEPH and the OPAL values are already incompatible to each other. However since our theory values are systematically too high for both sets, it would go too far to conclude that our theor supports the OPAL analysis.

Table 4.8: Values of average energy fractions for $c \to H_c$ and $b \to H_c$ transitions at $\mu_f = 2m_b$, 10.52 GeV and m_Z.

FF set	H_c	$\langle z \rangle_c(10.52\,\text{GeV})$	$\langle z \rangle_c(m_Z)$	$\langle z \rangle_b(2m_b)$	$\langle z \rangle_b(m_Z)$
Belle/CLEO-GM	D^0	0.623	0.479	0.470	0.273
	D^+	0.629	0.484	0.470	0.293
	D^{*+}	0.659	0.503	0.508	0.305
ALEPH/OPAL-GM	D^0	0.591	0.450	0.470	0.273
	D^+	0.596	0.455	0.470	0.293
	D^{*+}	0.614	0.462	0.508	0.305
global-GM	D^0	0.621	0.477	0.453	0.274
	D^+	0.629	0.484	0.451	0.288
	D^{*+}	0.655	0.499	0.501	0.306
Belle/CLEO-ZM	D^0	0.624	0.480	0.471	0.274
	D^+	0.632	0.486	0.470	0.293
	D^{*+}	0.661	0.504	0.509	0.306
ALEPH/OPAL-ZM	D^0	0.591	0.450	0.471	0.274
	D^+	0.596	0.455	0.470	0.294
	D^{*+}	0.613	0.461	0.509	0.306
global-ZM	D^0	0.623	0.479	0.454	0.275
	D^+	0.631	0.486	0.452	0.289
	D^{*+}	0.657	0.500	0.501	0.308

Table 4.9: Values of $c \to H_c$ and $b \to H_c$ branching fractions extracted by ALEPH [21] and OPAL [19, 20] at $\sqrt{s} = m_Z$ from their measured cross section distributions and from our theoretical distribution from the global fit.

$Q \to H_c$	ALEPH	OPAL	Theory
$c \to D^0$	0.559 ± 0.022	0.605 ± 0.040	0.628
$c \to D^+$	0.238 ± 0.024	0.235 ± 0.032	0.276
$c \to D^{*+}$	0.233 ± 0.015	0.222 ± 0.020	0.252
$b \to D^0$	-	-	0.515
$b \to D^+$	-	-	0.164
$b \to D^{*+}$	-	0.173 ± 0.020	0.221

Table 4.10: Values of average energy fractions for $c \to H_c$ transitions by Belle [25] and CLEO [26] at $\sqrt{s} = 10.52\,\text{GeV}$ and the matching value from our theoretical cross section distribution from the global fit. The values for Belle and CLEO are obtained by converting the corresponding average momentum fractions quoted in Refs. [25, 26], respectively.

H_c	Belle	CLEO	Theory
D^0	0.640 ± 0.002	0.640 ± 0.005	0.632
D^+	0.647 ± 0.001	0.650 ± 0.007	0.640
D^{*+}	0.682 ± 0.001	0.682 ± 0.006	0.666

Table 4.11: Values of average energy fractions for $c \to H_c$ transitions by ALEPH [21] and OPAL [19, 20] at $\sqrt{s} = m_Z$ from their measured cross section distributions and the matching value from our theoretical cross section distribution from the global fit.

H_c	ALEPH	OPAL	Theory (m_Z)
D^0	-	0.487 ± 0.014	0.509
D^+	-	0.483 ± 0.019	0.516
D^{*+}	0.488 ± 0.008	0.515 ± 0.009	0.532

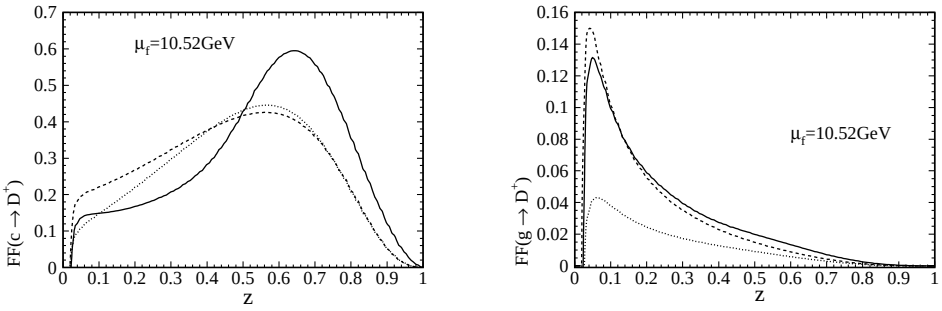

(a) (b)

Figure 4.9: (a) $c \to D^+$ and (b) $g \to D^+$ FFs of the global fit in the GM approach at $\mu_f = 10.52\,\text{GeV}$ (solid lines) compared with their counterparts from Refs. [24] (dashed lines) and [23] (dotted lines).

Chapter 5

Applications

5.1 Implementation of fragmentation functions

In this chapter we use the fragmentation functions from chapter 4 in different processes, which requires a more general implementation for different programs. For practical uses the evolution routine from the fit program is too slow. The main problem is that in most processes the factorization scale is not fixed like in electron-positron-annihilation. In deep-inelastic scattering (DIS) the typical process scale is a combination of the squared momentum transfer between the lepon to the hadron Q^2 and the produced hadron's squared transversal momentum p_T^2. Both variables may be integrated over and thus we require the FFs for many different scales when calculating a semi-inclusive cross section in DIS and other processes.

We provide the FFs $D_i^H(x, \mu_f)$ in the form of a Fortran routine which uses a grid in x and μ_f^2. This means that we have calculated the FFs for 29 values of Q^2 between $2.25\,\mathrm{GeV}^2 < \mu_f^2 < 10^6\,\mathrm{GeV}^2$ times 132 values of x between $10^{-4} < x < 1$. These values are saved in a grid. The function reads the selected FFs grid from a file and interpolates the return value from the grid entries with the help of a function from the CERN library.

5.2 Deep-inelastic scattering

In this section we utilize the FFs in deep-inelastic scattering in comparison with HERA data [31]. Since the GM-VFNS subtraction terms are not yet known for DIS, we use the ZM-VFNS results by Daleo et.al. [30] for the partonic cross section, which are available in the form of the Fortran program TIMBA. Here we use the affinity of the GM-VFNS to the massless result. Only the finite mass terms are missing in the partonic cross section, so the result shows the impact of the mass effects in the FFs on the semi-inclusive hadron cross section.

Unfortunately during our work we have learned about problems with TIMBA, which limit the range of applications. The first problem are errors in the terms which contain the logarithms of Q^2 [72]. At least some of these terms have the wrong prefix. We can eliminate these terms by setting the scale to Q^2, but as a consequence we cannot vary the scale. Therefore we cannot calculate a meaningful theoretical uncertainty.

The second problem occurs for large p_T values, where the calculated cross section is sometimes negative. This problem has also been observed in [73] for pion production, where it has been narrowed down to the channels with either quark or antiquark in the initial state and a fragmenting gluon in the final state. The contribution from the gluon fragmentation into D mesons is small and the program

has passed checks for other calculations like in [30]. We will therefore assume that the error only becomes sizable in certain kinematic regions like the high p_T region.

We will further use the partonic cross section to deduce the result for two-photon-scattering in the next section. In order to do that we will have to modify the program which contains the results by Daleo et.al. We therefore cite the most important formulae from [30] here.

5.2.1 Kinematics

We consider the process

$$l(l) + P(P) \to l'(l') + H_c(P_h) + X. \tag{5.1}$$

On the parton level we have to consider the process:

$$l(l) + q/\bar{q}/g(p) \to l'(l') + q/\bar{q}(k_1) + \bar{q}/q(k_2) + g(k_3). \tag{5.2}$$

We use the usual variables for deep inelastic scattering:

$$\begin{aligned} Q^2 = -q^2 = -(l' - l)^2, \quad x_B = \frac{Q^2}{2P \cdot q}, \\ y_e = \frac{P \cdot q}{P \cdot l}, \quad S_H = (P + l)^2, \quad S = (P + q)^2. \end{aligned} \tag{5.3}$$

The variable q is the spacelike momentum transfer between the lepton and hadron, while x_B is the Bjorken scaling variable. S_H is the CMS energy squared of the hadron system. And y_e measures the ratio of the energy transferred from the leptonic system to the hadronic system available in the target rest frame. From the latter follows, that $0 \leq y_e \leq 1$. It can also be written as

$$y_{el} = \frac{Q^2}{x_B S_H}, \quad p \cdot q = \frac{Q^2}{2x_B}, \tag{5.4}$$

and thus

$$Q^2 \leq x_B S_H. \tag{5.5}$$

The definition of the Mandelstam variables - at the hadron and the parton level - is given by

$$\begin{aligned} s = (q + p)^2, \quad S = (q + P)^2, \\ t = -2q \cdot k_1, \quad T = -2q \cdot P_h, \\ u = -2p \cdot k_1, \quad U = -2P \cdot P_h. \end{aligned} \tag{5.6}$$

We call the parton density functions $f_i(\xi)$, where ξ is the fraction of the proton momentum carried by the parton i, and the fragmentation functions $D_{c/j}(\zeta)$, where ζ is the fraction of the parton j carried by the final-state charmed hadron.

With these definitions the relation between hadronic and partonic Mandelstam variables is

$$s = \xi S - Q^2(1 - \xi), \quad t = \frac{T}{\zeta}, \quad u = \frac{\xi}{\zeta} U. \tag{5.7}$$

The program by Daleo et.al. contains the analytic result for $\mathrm{d}\sigma/(\mathrm{d}x_B \mathrm{d}Q^2 \mathrm{d}p_T \mathrm{d}\eta)$, where p_T is the transverse momentum and η the rapidity of the final-state hadron. The result is given in the CMS of the virtual photon and the incoming proton. Any of the differential variables can be integrated out in an arbitrary range using a VEGAS algorithm. It is important to note that the underlying theory does not

work for $p_T \to 0$ due to the missing masses, therefore we always have to use a lower bound for p_T in the magnitude $p_T \sim m_c$.

Some kinematic limits are respected by TIMBA automatically. The upper limit for the Q^2-integration is lowered to $Q^2 = x_B S_H$, if it is too high. With the energy $\sqrt{S} = \sqrt{(P+q)^2}$ in the photon-proton-CMS, TIMBA enforces the condition $p_T < \sqrt{S}/2$. The range of the rapidity is set to ensure $|\eta| < -\ln(\sqrt{S} - \sqrt{S - 4p_T^2}/(2p_T))$.

We make some changes to the program to adapt it to our calculation. The routine for α_s is replaced by our α_s-routine from chapter 4, so we use $\Lambda^{(5)}_{\overline{\text{MS}}} = 221\,\text{MeV}$ for $\mu > m_b$ and the accordingly matched value $\Lambda^{(4)}_{\overline{\text{MS}}} = 321\,\text{MeV}$ for scales below that. We use the PDF set CTEQ 6.5 by the CTEQ collaboration [74], which is implemented as a part of the LHAPDF library [75]. For the FFs we use our own set, where we use the FFs from the global fits with and without mass effects. Also we replace the built-in VEGAS integration routine, which did not work correctly on some ocassions, with the one from the CUBA library [68].

The factorization integral in [30] is written in the form:

$$\begin{aligned}
&\frac{\mathrm{d}\sigma^h}{\mathrm{d}x_B \mathrm{d}Q^2 \mathrm{d}p_T^2 \mathrm{d}\eta} \\
&= \sum_{i,j,n} \frac{e^{-\eta}\sqrt{S}}{|p_T|(Q^2+S)} \int\limits_{e^\eta |p_T|/\sqrt{S}}^{e^{2\eta}/(1+e^{2\eta})} \frac{\mathrm{d}y}{1-y} \\
&\quad \times \int\limits_0^{1-y/(1-y)e^{-2\eta}} \frac{\mathrm{d}z}{1-z} \left[f_i(\xi) D_{h/j}(\zeta) \frac{\mathrm{d}\sigma_{ij}^{(n)}}{\mathrm{d}x_B \mathrm{d}Q^2 \mathrm{d}y \mathrm{d}z} \right],
\end{aligned} \tag{5.8}$$

where y and z are auxiliary variables, which are defined in terms of the partonic Mandelstam variables:

$$\begin{aligned}
y &= -\frac{u}{Q^2+s}, \\
z &= \frac{(Q^2+s)(s+t+u)}{s(Q^2+s+u)}.
\end{aligned} \tag{5.9}$$

They are used instead of ξ and ζ, which can be calculated with the equations

$$\xi = \frac{Q^2(1-y)(1-z) + Sye^{-2\eta}}{(Q^2+S)(1-y)(1-z)}, \quad \zeta = \frac{e^\eta |p_T|}{\sqrt{S}y}. \tag{5.10}$$

The partonic cross sections are written in the form

$$\frac{\mathrm{d}\sigma_{ij}^{(n)}}{\mathrm{d}x_B \mathrm{d}Q^2 \mathrm{d}y \mathrm{d}z} = \frac{\alpha^2}{e^2} \frac{1}{\xi x_B^2 S_H^2} \left(Y_M(-g^{\mu\nu}) + Y_L \frac{4x_B^2}{Q^2} P^\mu P^\nu \right) \sum_n \overline{H}_{\mu\nu}^{(n)}(i,j), \tag{5.11}$$

where the $\overline{H}_{\mu\nu}^{(n)}(i,j)$ are the parton-photon squared matrix elements for the $i + \gamma \to j + X$ processes. Y_M and Y_L are the projectors for the metric and the longitudinal part of the cross section respectively:

$$Y_M = \frac{1 + (1-y_e)^2}{2y_e^2}, \quad Y_L = \frac{1 + 4(1-y_e) + (1-y_e)^2}{2y_e^2}. \tag{5.12}$$

5.2.2 Reference frames

A problem between theoretical and experimental results is the choice of reference frames. Theorists work in the CMS of the virtual boson and of the proton, which provides advantages due to the symmetry between the incoming particles after factorizing the cross section into a hadron and a lepton tensor. However the data are not collected in this reference frame. Experimentalists provide data in the laboratory frame, where one axis is defined by the proton and the electron beam.

In order to apply the experimental cuts from the HERA analysis in the theory, we have to use transformation formulas between the two systems. We take those from [76]. With the help of the auxiliary variable

$$A = \sqrt{\frac{Q^2(S_H - S - Q^2)}{S_H S}} m_T \exp(\eta) \tag{5.13}$$

with the transversal mass $m_T = \sqrt{p_T^2 + m_H^2}$ we can calculate the laboratory frame variables - denoted by the index L - by

$$\begin{aligned} p_T^L &= \sqrt{(p_T)^2 + A(A - 2p_T \cos\phi)}, \\ \eta_L &= \eta + \ln\left(\frac{(S+Q^2)m_T}{\sqrt{S_H} S m_T^L}\right) + \frac{1}{2}\ln\frac{E_e}{E_p}, \\ \cos\phi_L &= \frac{p_T\cos\phi - A}{p_T}. \end{aligned} \tag{5.14}$$

One should note that we need the variable ϕ, which is the azimuthal angle of the produced hadron. In the theorist's reference frame the cross section is independent of this angle, so we have to introduce an integration over ϕ in the calculation, where ϕ is only used to reproduce the experimental cuts via the transformation formulae (5.14).

5.2.3 Comparison to HERA data

We can now calculate theory predictions comparable to the HERA results from [31]. The data was taken in the years 1999 and 2000 colliding 27.5 GeV positrons and 920 GeV protons, which results in center-of-mass energy of $\sqrt{S_H} = 318\,\text{GeV}$.

The differential cross section is given in terms of x_B, Q^2, p_T^L and η_L, where the L denotes variables in the laboratory frame. The analysis is restricted to the kinematic region $2 \le Q^2 \le 100\,\text{GeV}^2$ and $0.05 \le y \le 0.7$. We implement the Q^2-region in the theory simply by the choice of the integration interval, while the limits on y are built into the program as cuts. However due to the relation between x_B, y and Q^2 we can conclude using eq.(5.4) that x_B will only have values within the interval $2.8 \cdot 10^{-5} \le x_B \le 2 \cdot 10^{-2}$.

A further constraint in [31] is $|\eta_L| < 1.5$, which is implemented as a cut. We ignore the constraint on p_T^L, but we use the results from [31], where the cut $p_T > 2.0\,\text{GeV}$ was applied, and use that value as lower bound for our p_T.

We calculate the cross sections with the global fit result with mass effects in the FFs and with the pure ZM-VFNS theory respectively. We use the theory with the scales $\mu_1 = Q^2$ and $\mu_2 = p_T^2 + Q^2$, where μ_1 is safe from the mentioned prefix errors in $\ln Q^2$ terms. The experimental results from [31] are taken from Table 7 therein. For comparison we compute values that are averaged over bins. We collect our results in the Tables (5.1) to (5.3) and list the experimental results where available for comparison. The results are also shown in Figs.(5.1) to (5.3).

We observe in Table (5.1), that the inclusion of mass effects in the FFs decreases the differential cross sections by $2-3\%$. The choice between the scales μ_1 and μ_2

x_B	Global-GM μ_1	Global-ZM μ_1	Global-GM μ_2	Global-ZM μ_2	Experiment
$[2.8 \cdot 10^{-5}, 0.0002]$	10280 (2858)	10503 (2935)	10538 (3658)	10826 (3747)	$7916 \pm 407^{+606}_{-791}$
$]0.0002, 0.0005]$	5285 (2233)	5394 (2287)	4961 (2245)	5082 (2298)	$3340 \pm 186^{+250}_{-316}$
$]0.0005, 0.0013]$	1324 (791.4)	1359 (809)	1263 (745.4)	1297 (762.0)	$974 \pm 60^{+107}_{-104}$
$]0.0013, 0.0032]$	237.0 (182.8)	241.8 (187.2)	234.6 (174.5)	239.5 (178.4)	$205 \pm 18^{+26}_{-43}$
$]0.0032, 0.02]$	9.473 (8.415)	9.720 (8.566)	9.414 (8.116)	9.416 (8.167)	$7.1 \pm 1.1^{+0.5}_{-1.9}$

Table 5.1: Values of D^* production cross section $\mathrm{d}\sigma/\mathrm{d}x_B$ in nb for deep-inelastic scattering averaged over bins in x_B in comparison with HERA data [31]. Theory values are with scales $\mu_1^2 = Q^2$ and $\mu_2^2 = p_T^2 + Q^2$ respectively. The values in brackets are the LO results.

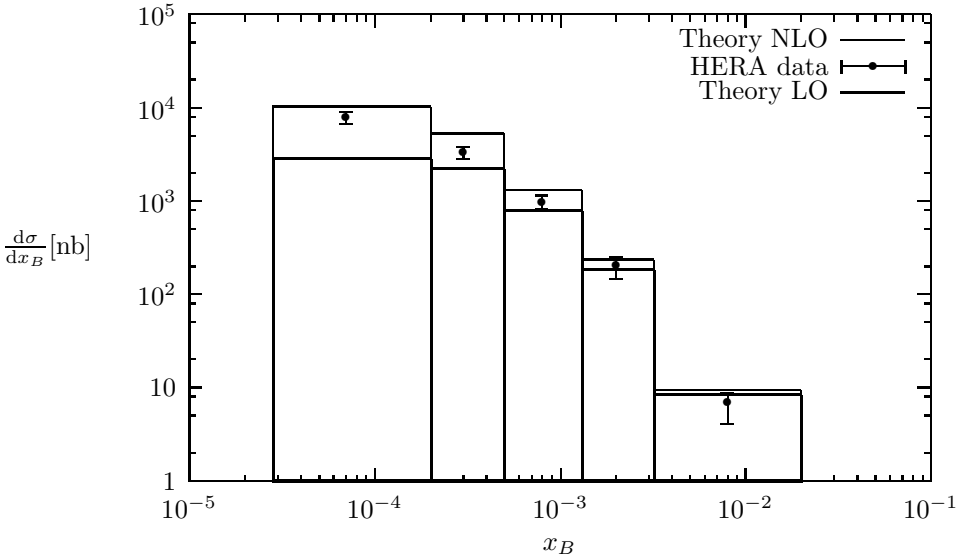

Figure 5.1: Production cross-section $\mathrm{d}\sigma/\mathrm{d}x_B$ in nb of D^* mesons for deep-inelastic scattering, distribution averaged over bins in x_B in comparison with HERA data [31].

Q^2	Global-GM μ_1	Global-ZM μ_1	Global-GM μ_2	Global-ZM μ_2	Experiment
$[2, 4.22]$	0.857 (0.231)	0.876 (0.237)	0.856 (0.294)	0.878 (0.301)	$0.54 \pm 0.03^{+0.04}_{-0.05}$
$]4.22, 10]$	0.278 (0.121)	0.285 (0.124)	0.261 (0.117)	0.267 (0.120)	$0.181 \pm 0.010^{+0.021}_{-0.019}$
$]10, 17.8]$	0.0841 (0.0503)	0.0860 (0.0516)	0.0841 (0.0482)	0.0859 (0.0494)	$0.069 \pm 0.005^{+0.005}_{-0.008}$
$]17.8, 31.7]$	0.0311 (0.0224)	0.0317 (0.0229)	0.0323 (0.0221)	0.0329 (0.0225)	$0.031 \pm 0.003^{+0.003}_{-0.004}$
$]31.7, 100]$	0.00620 (0.00539)	0.00630 (0.00549)	0.00613 (0.00521)	0.00632 (0.00530)	$0.0058 \pm 0.0005^{+0.0010}_{-0.0009}$

Table 5.2: Values of D^* production cross section $\mathrm{d}\sigma/\mathrm{d}Q^2$ in nb/GeV^2 for deep-inelastic scattering averaged over bins in Q^2 in comparison with HERA data [31]. Theory values are with scales $\mu_1^2 = Q^2$ and $\mu_2^2 = p_T^2 + Q^2$ respectively. The values in brackets are the LO results.

p_T	Global-GM μ_1	Global-ZM μ_1	Global-GM μ_2	Global-ZM μ_2
$[2, 2.5]$	3.503(1.662)	3.556(1.697)	3.910(1.851)	4.006(1.893)
$]2.5, 3.5]$	1.808(0.804)	1.849(0.823)	1.815(0.855)	1.856(0.874)
$]3.5, 5]$	0.636(0.276)	0.652(0.283)	0.547(0.267)	0.561(0.274)

Table 5.3: Theory values of D^* production cross section $\mathrm{d}\sigma/\mathrm{d}p_T$ in nb/GeV deep-inelastic scattering averaged over bins in p_T. The values are with scales $\mu_1^2 = Q^2$ and $\mu_2^2 = p_T^2 + Q^2$ respectively. The values in brackets are the LO results.

leads to a difference of similar magnitude. Both differences are hardly noticable in the graph, so we only plot the result of the GM-VFNS with μ_1 in NLO and LO in Fig.(5.1).

The enhancement of the cross section due to the inclusion of NLO effects is very strong for small x_B values. In the first bin the NLO result is almost a factor 4 higher than the LO result. This drops quickly to a factor of 2 in the next bins and settles down to $\sim 10\%$ in the last bin. In comparison between theory and experiment the NLO theory results are $\sim 30\%$ too high. Only one bin is compatible within the errors of the experimental measurement.

The results for the distribution in Q^2 are listed in Table (5.2) and plotted in Figure (5.2). We make very similar observations as in the case of x_B distributions. Only the comparison of theory and experiment is quite different: For the first bin the theory is too high by approximatley 50%. This difference gets smaller for higher values of Q^2 and leads to a match in the second-to-last bin. In the last two bins theory and experiment are compatible.

We have also calculated a distribution in p_T without a possibility for direct comparison with experimental data. The result can be found in Table 5.3 and Figure 5.3. The influence of the mass effects is similar as in the other distributions. However we observe a bigger influence of the choice of scale, possibly because p_T is not integrated out over its whole range. In the first bin the results with the scale $\mu_2^2 = p_T^2 + Q^2$ are $\sim 10\%$ bigger, while they are almost equal in the middle bin and

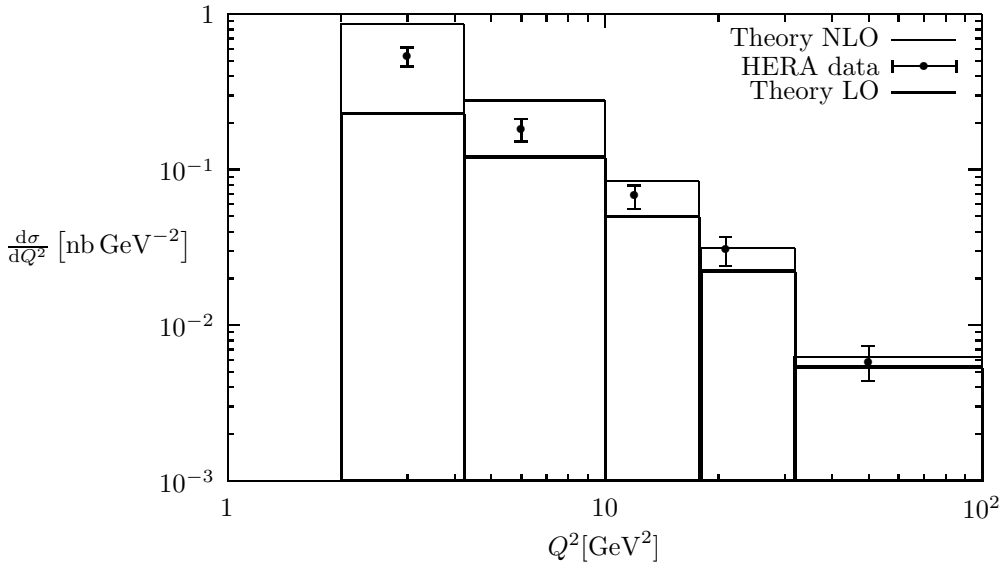

Figure 5.2: Production cross-section $d\sigma/dQ^2$ in nb/GeV^2 of D^* mesons for deep-inelastic scattering, distribution averaged over bins in Q^2 in comparison with HERA data [31].

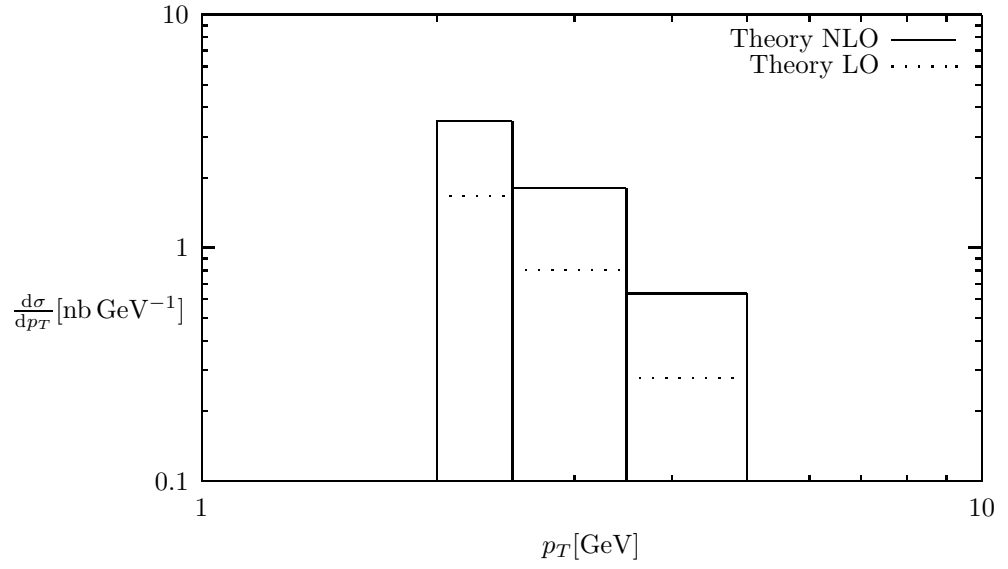

Figure 5.3: Production cross-section $d\sigma/dp_T$ in nb/GeV of D^* mesons for deep-inelastic scattering, distribution averaged over bins in p_T.

$\sim 15\%$ smaller in the third bin.

5.3 Deep-inelastic two-photon-scattering

We consider the scattering process $\gamma + \gamma^* \to H_c + X$ which is a subprocess of the process $e^- + e^+ \to e^- + e^+ + H_c + X$ and occurs in two kinds of colliders. The first type is an electron-positron-collider. The real photon can be radiated off a lepton as a collinear quasi-real particle, where the energy spectrum of the real photons is described by the Weizsäcker-Williams approximation [36]. For this kind of photon radiation we follow the approach in [77]. In addition a future ILC is expected to have a sizable contribution of photons due to beamstrahlung, which can be described by an additional spectrum in good approximation.

In terms of the experiment we are looking for single-tagged events, that means that one lepton - the one emitting the virtual photon - is detected in the final state. In contrast events where both leptons emit real photons lead to no-tagged events without detected leptons in the final state, since the leptons are only slightly deflected when emitting real photons and therefore hit the detector's blind cone around the beam pipe.

The other kind of collider is the future $e\gamma$ mode of the International Linear Collider (ILC), where a beam of high-energetic photons is going to be produced by back-scattering a laser beam in one of the collider's lepton beams. Instead of the Weizsäcker-Williams formula we have to take the Compton spectrum of the back-scattered photons into account.

In order to compute results for these processes we use the result above for deep-inelastic scattering and replace the proton by a photon. There are two kinds of photon contribution, which have to be summed: In the case of the resolved photon the photon is modeled as a particle containing partons just like a proton. While the photon is an elementary particle in the standard model, it can fluctuate into virtual quark-antiquark-pairs and hence into gluons. This contribution is calculated simply by replacing the proton PDF by a photon PDF, which are available in the literature.

In the second case we consider the direct contribution of a photon scattering with the virtual photon coming from the particle beam's electron. This process is related to the deep-inelastic scattering of the proton via the gluon channel. We will only consider the gluon channel contribution of the Daleo result and replace the gluon in the initial state by the photon, which means that we have to adjust the coupling factor and we have to discard the contributions coming from the non-Abelian part of the gluon coupling.

5.3.1 Photon spectra

We have to add a convolution with a photon spectrum to the differential cross section formula in the program TIMBA, whether we consider the Weizsäcker-Williams formula or the beamstrahlung spectrum for the e^+e^- collider or the possible $e\gamma$ mode of the ILC with a Compton spectrum. In analogy to the DIS kinematics we call the four-momentum of the lepton, which radiates the photon, P and assume that it is the lepton flying in positive direction along the beam axis. The photon then has the four-momentum $P_\gamma = \tau P$. We denote all variables in the intermediate state with the initial-state photon with a γ. The hadronic variables in TIMBA have to be replaced by the ones of the intermediate state. The variables affected by the reduced photon energy are

$$S_H \quad \to \quad S_{H\gamma} = \tau S_H \tag{5.15}$$

$$x_B \quad \rightarrow \quad x_\gamma = x_B/\tau,$$

while the remaining variables are deduced from S_H, x_B and unaffected variables such as Q^2. However the respective CM systems of the intermediate state and of the overall hadronic state differ by a boost along the direction of the electron radiating the real photon. The $e\gamma^*$-system is moving compared to the $\gamma\gamma^*$-system in the direction of the electron with a velocity (see (4.13)) of

$$\beta_L = \frac{1-\tau}{1+\tau}. \tag{5.16}$$

This translates into a rapidity between the systems of

$$\eta_\Delta = -\frac{1}{2}\ln\tau. \tag{5.17}$$

Therefore we have the relation

$$\eta_\gamma = \eta + \eta_\Delta = \eta - \frac{1}{2}\ln\tau. \tag{5.18}$$

The cross section is then

$$\frac{\mathrm{d}\sigma}{\mathrm{d}x_B}(x_B, S_H, \eta) = \int_{x_B}^{1} \frac{\mathrm{d}\tau}{\tau}\frac{\mathrm{d}\sigma_\gamma}{\mathrm{d}x_\gamma}(x_\gamma, S_\gamma, \eta_\gamma) f_{\gamma/l}(\tau), \tag{5.19}$$

where $f_{\gamma/l}(\tau)$ is the photon spectrum.

For the photon distribution we consider the following three spectra. First we apply the Weizsäcker-Williams (WW) approximation, which describes quasi-real photons emitted by leptons:

$$f_{\gamma/l}(\tau) = \frac{\alpha}{2\pi}\frac{1+(1-\tau)^2}{\tau}\ln\left(\frac{Q^2_{max}}{Q^2_{min}}\right). \tag{5.20}$$

Here we use the leading approximation and have neglected some terms, which only give a small correction. The limits of Q^2 are set to $Q^2_{min} = m_e^2 x_B^2/(1-x_B)$, which comes from the kinematics, and $Q^2_{max} = 1\,\mathrm{GeV}^2$. The variable τ runs in the theoretic kinematical range [79]

$$\frac{p_T \cdot e^{-\eta}}{\sqrt{S_H} - p_T e^{\eta}} < \tau < 1. \tag{5.21}$$

We can expect an additional source of quasi-real photons to become non-negligible at the ILC: The leptons move within the electromagnetic field of the opposing particle bunch at the crossing point, which leads to the possibility of photon radiation. This phenomenon is known as beamstrahlung. Since the ILC beam design is not finalized yet, we settle for using the ready-to-use parameters from [80], which were deduced for the comparable TESLA design, and take the photon spectrum from equations (2.11) to (2.16) in [37].

In the third case we examine a plausible scenario for a $e\gamma$-mode at ILC proposed in [38]. The energy of a photon back-scattered by the electron beam is

$$\omega = \frac{\omega_m}{1+(\vartheta/\vartheta_0)^2}, \tag{5.22}$$

where ϑ is the photon scattering angle with respect of the initial direction of the electron. The other variables are

$$\omega_m = \frac{x_T}{x_T+1}E_0, \quad \vartheta_0 = \frac{m}{E_0}\sqrt{x_T+1}, \tag{5.23}$$

where ω_m is the photon's highest possible energy and E_0 is the beam energy and x_T is a parameter calculated from the laser's properties like the laser photon energy ω_0.

Plausible values to achieve high luminosity and energy with currently available lasers are $E_0 = 250\,\mathrm{GeV}$, $\omega_0 = 1.17\,\mathrm{eV}$ and $x_T = 4.8$ leading to $\omega_m/E_0 = 0.83$.

The energy spectrum of the back-scattered photons is [78]

$$\frac{1}{\sigma_c}\frac{\mathrm{d}\sigma_c}{\mathrm{d}y_T} = \frac{2\sigma_0}{x_T\sigma_c}\left(1 - y_T + \frac{1}{1-y_T} - \frac{4y_T}{x_T(1-y_T)} + \frac{4y_T^2}{x_T^2(1-y_T)^2}\right) \tag{5.24}$$

with the total cross section

$$\sigma_c = \frac{2\sigma_0}{x_T}\left[\left(1 - \frac{4}{x_T} - \frac{8}{x_T^2}\right)\ln(x_T+1) + \frac{1}{2} + \frac{8}{x_T} - \frac{1}{2(x_T+1)^2}\right] \tag{5.25}$$

and the constant $\sigma_0 = \pi(e^2/m_e)^2$. The spectrum is cut off at $y_T = \omega_m$.

5.3.2 Resolved photon contribution

For the resolved contribution we apply the photon PDFs by Aurenche, Guillet and Fontannaz [35]. The AGF-PDFs have been extracted from LEP data in a variable flavor number scheme. Similar to the GM-VFNS, they keep mass terms of the order m_Q^2/Q^2 in the cross section and recover the ZM-VFNS in the massless limit. In addition they have to model non-perturbative input for smaller ξ, where they apply a vector dominance model. We refer to their publication [35] for more details.

The AGF PDFs are fitted with $\Lambda^{(4)}_{\overline{\mathrm{MS}}} = 300\,\mathrm{MeV}$, so there we have a slight mismatch to out value of $\Lambda^{(4)}_{\overline{\mathrm{MS}}} = 321\,\mathrm{MeV}$.

5.3.3 Direct photon contribution

First we have to remove the PDFs from the calculation. This can be done analytically by setting

$$f_g(\xi) = \delta(1-\xi). \tag{5.26}$$

The formula from Daleo for ξ is

$$\xi = \frac{Q^2(1-y)(1-z) + Sye^{-2\eta}}{(Q^2+S)(1-y)(1-z)}. \tag{5.27}$$

From this we get a delta function for z:

$$\delta(1-\xi) = \frac{(Q^2+S)ye^{-2\eta}}{S(1-y)} \cdot \delta\left(z - 1 + \frac{ye^{-2\eta}}{1-y}\right). \tag{5.28}$$

For elastic contributions - the Born part and the delta distribution terms - the integration over z is already performed in TIMBA using a $\delta(z)$ function in the coefficient functions. For the inelastic part divergencies are handled by a plus distribution in z. Therefore it is advisable to use the new delta distribution to perform the integration over y. The delta distribution is then:

$$\delta(1-\xi) = \frac{(Q^2+S)e^{-2\eta}(1-z)}{S(1-z+e^{-2\eta})^2} \cdot \delta\left(y - \frac{1-z}{1-z+e^{-2\eta}}\right). \tag{5.29}$$

Furthermore we change the order of integrations. The integration over y becomes the inner integral, so that we can apply the delta distribution. From eq.(5.8) we read off the integration boundaries for the original integration order are

$$\begin{aligned} y_{\min} &= e^{\eta}|p_T|/\sqrt{S}, \quad y_{\max} = e^{2\eta}/(1+e^{2\eta}), \\ z_{\min} &= 0, \quad z_{\max} = 1 - y/(1-y)e^{-2\eta}. \end{aligned} \tag{5.30}$$

In a $y-z$-plane these integration boundaries give an area which is limited by the straight lines given by $y_{\min}$, $z_{\min}$ and the curve given by $z_{\max}(y)$. In order to reverse the integration order we rewrite this curve as a function of y, which gives

$$\tilde{y}_{\max}(z) = \frac{1-z}{1-z+e^{-2\eta}}. \tag{5.31}$$

The lower bounds stay the same. For the upper bound of z we require the crossing point of the curve with the $y_{\min}$-line, which we get by inserting $y_{\min}$ into $z_{\max}$:

$$\tilde{z}_{\max} = \frac{\sqrt{S} - 2p_T \cosh\eta}{\sqrt{S} - e^{\eta} p_T}. \tag{5.32}$$

In summary:

$$\tilde{y}_{\min} = e^{\eta}|p_T|/\sqrt{S}, \quad \tilde{y}_{\max} = \frac{1-z}{1-z+e^{-2\eta}}, \tag{5.33}$$

$$\tilde{z}_{\min} = 0, \quad \tilde{z}_{\max} = \frac{\sqrt{S} - 2p_T \cosh\eta}{\sqrt{S} - e^{\eta} p_T}.$$

The PDFs of the quarks and antiquarks are set to zero, since we only need the incoming gluon which we are going to convert into a photon.

5.3.4 Couplings and color factors

For the direct photon contribution we can discard the non-Abelian parts of the gluon coupling by using the color factors. We examine the change of the coupling and charge factors at diagrams representing the squared matrix element. In Fig.(5.4) we show the cut diagrams of NLO scattering graphs with real gluon radiation. The left graph has an incoming gluon in the initial state, which is replaced by a photon in the right graph. The first change is trivial: One factor of the strong coupling constant α_s is replaced by the electro-weak α. Also we square the occuring electrical charge fractions of the quarks, since they now couple twice to a photon instead of once.

The case with the incoming gluon leads to the color factor:

$$\frac{1}{8}\sum_{a,b} \mathrm{Tr}\left[T_a^{(F)} T_a^{(F)} T_b^{(F)} T_b^{(F)}\right] = \frac{1}{8} C_F^2 \mathrm{Tr}(\mathbf{1}\cdot\mathbf{1}) = \frac{1}{8} C_A C_F^2 = T_F C_F = \frac{2}{3}, \tag{5.34}$$

with $T_F = 1/2$ and the factor $1/8$ coming from the averaging over the possible color states of the incoming gluon.

If we replace the incoming gluon by a photon, this changes to:

$$\sum_{a} \mathrm{Tr}\left[T_a^{(F)} T_a^{(F)}\right] = C_F \mathrm{Tr}(\mathbf{1}) = C_A C_F = 4. \tag{5.35}$$

So we just have to multiply with a factor of 6 for this class of diagrams. The same applies for the Born contributions, where the color factor in the gluon case is $T_F = 1/2$ and for the photon case $C_A = 3$.

We take a look at the other types of cut diagrams concerning color factors in Fig.(5.5), which have been calculated with the help of the program COLOR [81]. The first graph is non-Abelian and has the color factor $-1/12$. The second graph with initial-state gluon radiation has the factor $T_F C_A = 3/2$. The latter two graphs - describing vertex corrections and interference terms between graphs radiating a gluon from their gluon and their quark line respectively - provide the factor $T_F^2 C_A = 3/4$.

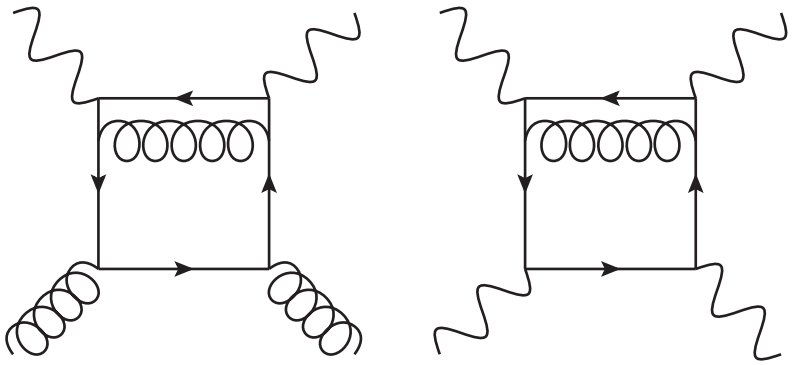

Figure 5.4: Cut diagrams for comparison of initial state gluon and initial state photon

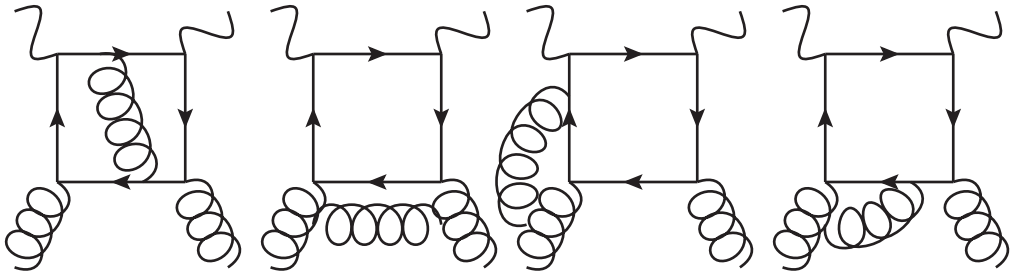

Figure 5.5: Cut diagrams for possible color factors in DIS, the first graph is non-Abelian, the other three contain gluon self-couplings and are therefore Abelian.

The final result for DIS contains terms with the color factors T_F in the Born terms, and $C_A T_F$ and $C_F T_F$ in the NLO terms. This makes it possible to distinguish Abelian and non-Abelian terms. The terms proportional to $C_A T_F$ are dropped. The remaining result for LO and NLO has to be multiplied with the already mentioned factor of 6 to correct the color factors.

5.3.5 Theory predicitions for LEP1

We are now ready to run some calculations with exploratory character. The process in question is $e^- + e^+ \to e^- + e^+ + 2(3)\,\text{Jets}$. In [32] this process is examined for the LEP1 run. While the reference does not examine heavy hadron production, we take the kinematic ranges from the analysis to have a realistic prediction in regards to possible experimental analysis and we focus on D^* production.

For LEP1 we have $\sqrt{S_H} = M_Z$. According to [32] the reach of S is $3 < \sqrt{S} < 35\,\text{GeV}$. We pick values of $Q^2 = 2.5,\ 10,\ 30\,\text{GeV}^2$, while we integrate out x_B in the range that follows from the kinematics. The rapidity is set to $\eta = 0$. The scale is set to $\mu^2 = Q^2$. We assume that the lepton flying in positive direction emits the real photon and the other lepton emits the virtual photon. If an analysis of single-tagged events does not differentiate which lepton radiated off the real photon one has to double the results.

During the calculation we notice that the direct contribution takes longer to calculate, despite the fact that it is integrated over one less variable. We suspect that the delta functions (5.28) and (5.29) increase the contribution of divergent

p_T [GeV]	Direct GM-FFs	Resolved GM-FFs	Sum GM-FFs
1	722	205	927
2	124	19.1	143
3	26.7	2.83	29.5
4	7.18	0.588	7.77
5	2.06	0.149	2.21
6	0.567	0.0415	0.609
7	0.107	0.0119	0.119

Table 5.4: Differential production cross section $\mathrm{d}\sigma/(\mathrm{d}Q^2\mathrm{d}p_T\mathrm{d}\eta)$ in $\mathrm{fb\,GeV}^{-3}$ for D^* mesons in deep-inelastic two-photon-scattering with Weizsäcker-Williams photon spectrum for LEP1, distribution in p_T at $Q^2 = 2.5\,\mathrm{GeV}^2$.

p_T [GeV]	Direct GM-FFs	Resolved GM-FFs	Sum GM-FFs
1	45.0	12.5	57.5
2	11.6	2.21	13.8
3	3.42	0.454	3.87
4	1.13	0.113	1.24
5	0.409	0.0315	0.441
6	0.157	$9.51 \cdot 10^{-3}$	0.167
7	0.0619	$3.15 \cdot 10^{-3}$	0.0651
8	0.0241	$9.51 \cdot 10^{-4}$	0.0251
9	$8.63 \cdot 10^{-3}$	$2.41 \cdot 10^{-4}$	$8.87 \cdot 10^{-3}$
10	$2.68 \cdot 10^{-3}$	$2.85 \cdot 10^{-5}$	$2.71 \cdot 10^{-3}$

Table 5.5: Differential production cross section $\mathrm{d}\sigma/(\mathrm{d}Q^2\mathrm{d}p_T\mathrm{d}\eta)$ in $\mathrm{fb\,GeV}^{-3}$ for D^* mesons in deep-inelastic two-photon-scattering with Weizsäcker-Williams photon spectrum for LEP1, distribution in p_T at $Q^2 = 10\,\mathrm{GeV}^2$.

parts of the integrand at the boundaries of the integration region. This would lead to a worse convergence behaviour of the integration routine and thus explain the longer calculation time.

We have collected the results in Tables (5.4) to (5.6) and plotted them in Figs.(5.6) to (5.8). In all cases the direct contribution dominates the result. For low values of p_T it surpasses the resolved contribution by a factor of 3 to 5, for higher values of p_T the resolved contribution almost becomes negligible being a factor of 100 smaller. We have to point out that the results for the lowest values of p_T are probably unrealistic due to using massless parton cross sections.

With regards to the leading order formula for DIS (5.8) it is not surprising that the differential cross section drops off with rising p_T and rising Q^2. However we observe a huge drop of the cross section by a factor of 10^4 while raising p_T by a factor of 10. The dependence of the cross section of Q^2 is weaker but still strong: When raising Q^2 by a factor of 12, the final value drops by a factor between 5 and 100.

5.3.6 Comparison to LEP2

For the LEP2 run there has been an analysis by the OPAL Collaboration of charm quark production in deep-inelastic electron-photon-scattering in [33]. This has been achieved by the analysis of D^*-production events and the extrapolation to charm

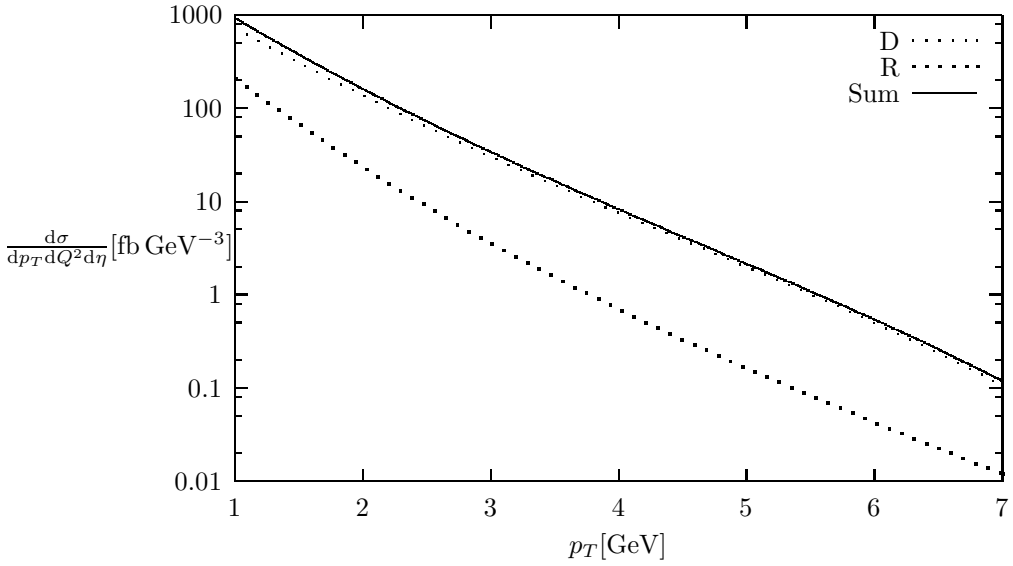

Figure 5.6: Differential production cross section $d\sigma/(dQ^2 dp_T d\eta)$ for D^* mesons in deep-inelastic two-photon-scattering with Weizsäcker-Williams photon spectrum for LEP1, distribution in p_T at $Q^2 = 2.5\,\mathrm{GeV}^2$. Direct contribution (D) thin-dotted line, resolved contribution (R) thick-dotted line and sum solid line.

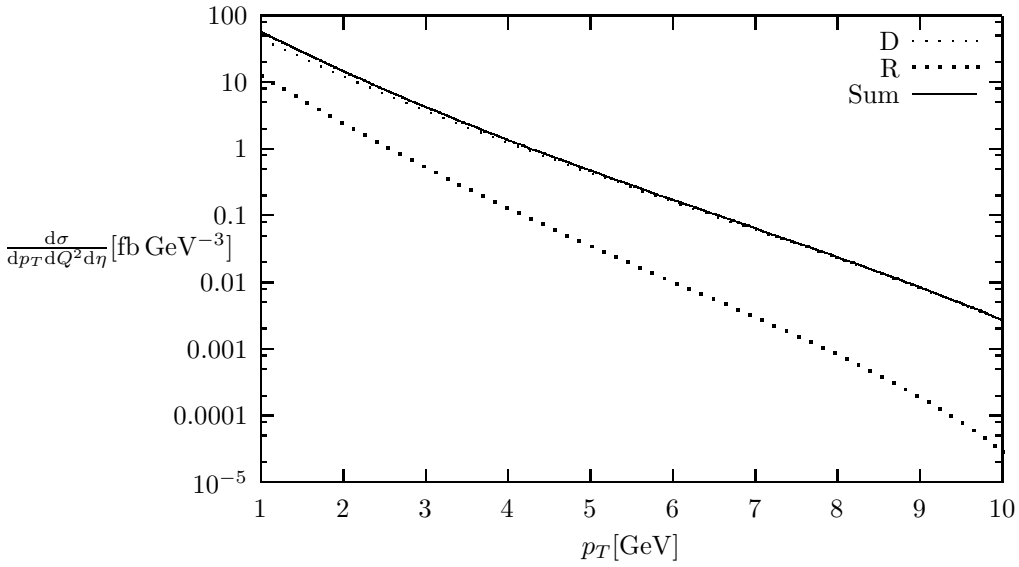

Figure 5.7: Differential production cross section $d\sigma/(dQ^2 dp_T d\eta)$ for D^* mesons in deep-inelastic two-photon-scattering with Weizsäcker-Williams photon spectrum for LEP1, distribution in p_T at $Q^2 = 10\,\mathrm{GeV}^2$. Direct contribution (D) thin-dotted line, resolved contribution (R) thick-dotted line and sum solid line.

p_T [GeV]	Direct GM-FFs	Resolved GM-FFs	Sum GM-FFs
1	8.67	1.72	10.4
2	1.53	0.336	1.87
3	0.620	0.0955	0.716
4	0.254	0.0303	0.284
5	0.108	0.0104	0.118
6	0.0479	$3.83 \cdot 10^{-3}$	0.0517
7	0.0218	$1.46 \cdot 10^{-3}$	0.0233
8	0.0100	$5.70 \cdot 10^{-4}$	0.0106
9	$4.54 \cdot 10^{-3}$	$2.21 \cdot 10^{-4}$	$4.76 \cdot 10^{-3}$
10	$2.02 \cdot 10^{-3}$	$8.31 \cdot 10^{-5}$	$2.10 \cdot 10^{-3}$

Table 5.6: Differential production cross section $\mathrm{d}\sigma/(\mathrm{d}Q^2\mathrm{d}p_T\mathrm{d}\eta)$ in $\mathrm{fb\,GeV^{-3}}$ for D^* mesons in deep-inelastic two-photon-scattering with Weizsäcker-Williams photon spectrum for LEP1, distribution in p_T at $Q^2 = 30\,\mathrm{GeV}^2$.

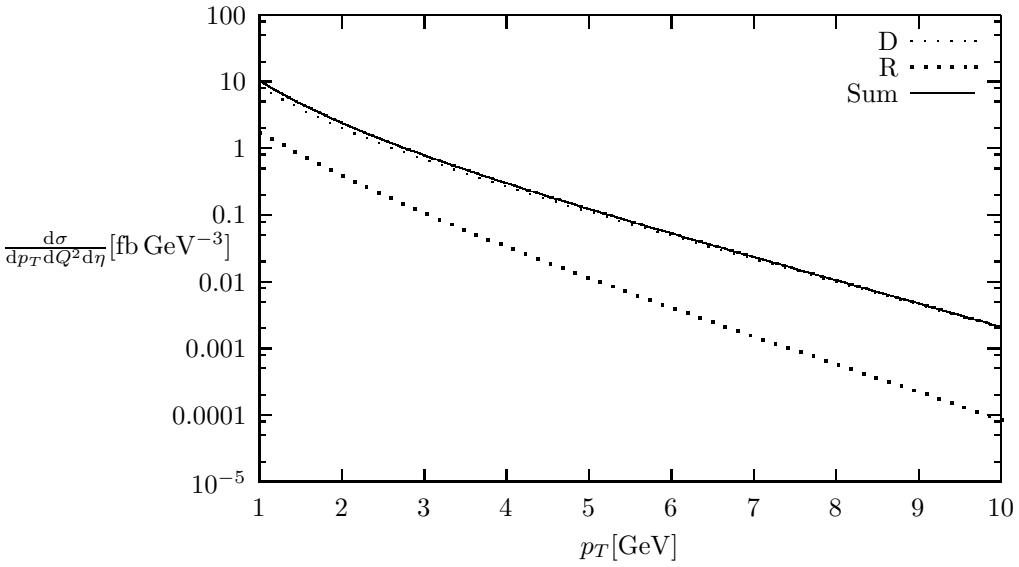

Figure 5.8: Differential production cross section $\mathrm{d}\sigma/(\mathrm{d}Q^2\mathrm{d}p_T\mathrm{d}\eta)$ for D^* mesons in deep-inelastic two-photon-scattering with Weizsäcker-Williams photon spectrum for LEP1, distribution in p_T at $Q^2 = 30\,\mathrm{GeV}^2$. Direct contribution (D) thin-dotted line, resolved contribution (R) thick-dotted line and sum solid line.

production with the help of Monte Carlo simulations, so that some D^* data is available as an intermediate step.

Several data sets are included in the analysis with an weighted average energy CMS energy of $\sqrt{S_H} = 196.6\,\text{GeV}$. The kinematical ranges are $5 < Q^2 < 100\,\text{GeV}^2$, $|\eta_L| < 1.5$ with the two bins $0.0014 < x_B < 0.1$ and $0.1 < x_B < 0.87$. The limit on p_T^L depends on the scattering angle θ of the electron which emitted the virtual photon: It is $p_T^L > 1\,\text{GeV}$ for $33 < \theta < 55\,\text{mrad}$ and $p_T^L > 3\,\text{GeV}$ for $60 < \theta < 120\,\text{mrad}$. We implement the limits of variables in the laboratory frame as cuts using the transformation formulae (5.14) and the ones on x_B and Q^2 as the integration range. The result has to be doubled since real photons radiated off by leptons from both directions have been accepted in the OPAL analysis. In addition we have to set a lower bound for p_T.

For the conditions on p_T^L we need to know θ in the program to implement the cuts. Fortunately we can calculate it together with the scattered electron's energy E_e from x_B and Q^2. In the laboratory frame we deduce from the definition

$$\begin{aligned} Q^2 &= \sqrt{S_H} E_e (1 - \cos\theta), \\ x_B &= \frac{E_e(1-\cos\theta)}{\sqrt{S_H} - E_e(1+\cos\theta)}, \end{aligned} \tag{5.36}$$

and this leads to

$$\cos\theta = \frac{x_B S_H - Q^2 - x_B Q^2}{x_B S_H - Q^2 + x_B Q^2}. \tag{5.37}$$

Work with the program shows that the several integrations and the cuts push the numerical integration routine to its limits. The number of iterations for VEGAS has to be increased significantly compared to the earlier LEP1 calculations to get a result, which seems stable against small variations of the integration parameters.

The results are acceptable for the first bin of x_B. The resolved contribution is $\sigma_R(0.0014 < x_B < 0.1) = 0.97\,\text{pb}$. In [33] (Table 1 therein) the result calculated with the event generator HERWIG is $\sigma_R^H(0.0014 < x_B < 0.1) = 0.43\,\text{pb}$. The direct contribution is $\sigma_D(0.0014 < x_B < 0.1) = 0.46\,\text{pb}$, while the HERWIG prediction is $\sigma_D^H(0.0014 < x_B < 0.1) = 0.71\,\text{pb}$. Added together our prediction is $\sigma(0.0014 < x_B < 0.1) = 1.43\,\text{pb}$ and therefore about $\sim 30\%$ higher than HERWIGs $\sigma^H(0.0014 < x_B < 0.1) = 1.13\,\text{pb}$. The measured value from the data of the detector OPAL is $\sigma^O(0.0014 < x_B < 0.1) = 3.1 \pm 1.0 \pm 0.5\,\text{pb}$. Our results lies almost within the error bars of the measurement. If we take into account the lower bound for p_T and the lack of precision for low p_T values in our approach, this is a good result.

For the second bin $0.1 < x_B < 0.87$ we fail to get a meaningful result. With higher values of x_B higher values of Q^2 play a larger role and the difference between p_T and p_T^L grows. In this case the lower bound for p_T required for the theory together with the strict cuts on p_T^L from the experimental analysis reduce the calculation result by several magnitudes.

5.3.7 Theory predictions for ILC

We now focus our attention on the planned International Linear Collider (ILC)[34]. We present predictions for the D^* production in analogy to the LEP1 calculations above. In addition we provide extra data for one value of Q^2 including differential production cross sections for D^0 and D^+ for comparison.

The planned CMS energy for the first phase of the ILC is $\sqrt{S_H} = 500\,\text{GeV}$ with an integrated luminosity of $\mathcal{L} = 1000\,\text{fb}^{-1}$. For kinematic limits we use the equation $Q^2 = y_{el} x_B S_H$. We pick the values $Q^2 = 2.5$, 10, 30 GeV respectively and

p_T[GeV]	Direct WW	Resolved WW	Direct Beam	Resolved Beam	Sum
2	98.5	79.5	257	201	637
6	7.02	2.42	16.3	4.74	30.4
10	1.62	0.357	2.82	0.476	5.28
14	0.574	0.0903	0.713	0.0800	1.45
18	0.253	0.0300	0.213	0.0175	0.514
22	0.126	0.0118	0.0702	$4.49 \cdot 10^{-3}$	0.212
26	0.0685	$5.22 \cdot 10^{-3}$	0.0244	$1.30 \cdot 10^{-3}$	0.0994
30	0.0393	$2.45 \cdot 10^{-3}$	$8.45 \cdot 10^{-3}$	$3.42 \cdot 10^{-4}$	0.0506

Table 5.7: Differential production cross section $\mathrm{d}\sigma/(\mathrm{d}Q^2\mathrm{d}p_T\mathrm{d}\eta)$ in $\mathrm{fb\,GeV}^{-3}$ for D^* mesons in deep-inelastic two-photon-scattering with Weizsäcker-Williams and beamstrahlung photon spectrum for ILC, distribution in p_T at $Q^2 = 2.5\,\mathrm{GeV}^2$.

set $\eta = 0$. The limits for y_{el} depend on the detection range for the outgoing lepton which emitted the virtual photon. We use $0.2 < y_{el} < 0.9$ as plausible limits, where the upper limit is more interesting since it determines the lower limit of x_B. The limits for x_B are therefore $1.11 \cdot 10^{-5} < x_B < 5 \cdot 10^{-5}$, $4.44 \cdot 10^{-5} < x_B < 2 \cdot 10^{-4}$ and $1.33 \cdot 10^{-4} < x_B < 6 \cdot 10^{-4}$ for the three values of Q^2 respectively. We assume that the lepton flying in positive direction along the beam axis provides the real photon, so the result has to be doubled if the sources of the real and virtual photon are not discriminated.

In contrast to the LEP1 case we now have to add the beamstrahlung spectrum as a source for quasi-real photons. As described in section 5.3.1, we use the parameters from [80] with the equations (2.11) to (2.16) in [37].

We present the results for D^* production distributed in p_T in Tables 5.7 to 5.9 and in Figures 5.9 to 5.11. The contributions for Weizsäcker-Williams and beamstrahlung spectra have been calculated seperately. For the WW case we naturally find similarities to the LEP1 calculations. Typically the direct contribution dominates. For values around $p_T \sim 30\,\mathrm{GeV}$ it is higher by a factor of ~ 10. However for $Q^2 = 10\,\mathrm{GeV}$ and $Q^2 = 30\,\mathrm{GeV}$ the value for $p_T = 2\,\mathrm{GeV}$ the resolved contribution is actually higher, but drops off quicker with rising p_T.

When comparing the WW spectrum and the beamstrahlung spectrum contributions, we observe a stronger p_T dependence of the beamstrahlung parts. For all values of Q^2 the beamstrahlung contributions at $p_T = 2\,\mathrm{GeV}$ are higher by a factor of 2 to 3, however for $p_T = 30\,\mathrm{GeV}$ they are almost one magnitude smaller. The point where both spectrum contributions are equal is in all cases around $p_T \sim 15\,\mathrm{GeV}$.

The overall result depends strongly on p_T. We raise p_T by a factor of 15, as a consequence the differential cross sections drop by a factor of up to 10^4. Going from $Q^2 = 2.5\,\mathrm{GeV}$ to $Q^2 = 30\,\mathrm{GeV}$ reduces the result by a factor of ~ 50.

Next we examine the process for $e\gamma$ mode of the ILC. We do this by describing the photon spectrum with the Compton spectrum (5.24). Variations of that spectrum are possible depending on the polarization of the electron beam and of the laser beam. Apart from the different photon spectrum the luminosity will drop off by a factor of ~ 5 or more, which should be kept in mind when comparing cross sections of the e^-e^+ and of the $e\gamma$ mode. This is discussed in more detail in [38].

We first present as above for the e^-e^+ mode distributions in p_T for the three values $Q^2 = 2.5\,\mathrm{GeV}^2$, $Q^2 = 10\,\mathrm{GeV}^2$ and $Q^2 = 30\,\mathrm{GeV}^2$ with $\eta = 0$ and the range $0.2 < y_{el} < 0.9$. The results can be found in the Tables 5.10 to 5.12 and the accompanying Figures 5.12 to 5.14.

The first observation is that the p_T dependence is milder. When increasing p_T by a factor of 15 the differential cross decreases by a factor of only ~ 500 instead of

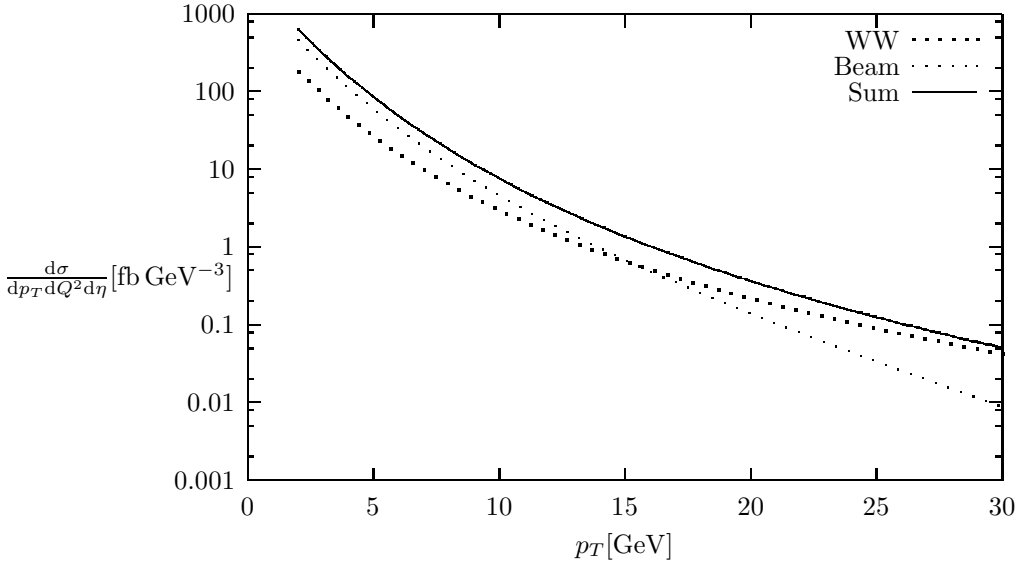

Figure 5.9: Differential production cross section $d\sigma/(dQ^2 dp_T d\eta)$ in fb GeV^{-3} for D^* mesons in deep-inelastic two-photon-scattering with Weizsäcker-Williams (thick-dotted) and beamstrahlung (thin-dotted) photon spectrum for ILC, distribution in p_T at $Q^2 = 2.5\,\text{GeV}^2$.

p_T[GeV]	Direct WW	Resolved WW	Direct Beam	Resolved Beam	Sum
2	4.26	8.21	10.7	19.4	42.6
6	0.684	0.320	1.57	0.599	3.17
10	0.175	0.0480	0.302	0.0612	0.586
14	0.0646	0.0124	0.0767	0.0105	0.165
18	0.0291	$4.28 \cdot 10^{-3}$	0.0237	$2.27 \cdot 10^{-3}$	0.0594
22	0.0147	$1.65 \cdot 10^{-3}$	$7.94 \cdot 10^{-3}$	$5.77 \cdot 10^{-4}$	0.0249
26	$8.16 \cdot 10^{-3}$	$7.77 \cdot 10^{-4}$	$2.91 \cdot 10^{-3}$	$1.92 \cdot 10^{-4}$	0.0121
30	$4.69 \cdot 10^{-3}$	$3.67 \cdot 10^{-4}$	$1.09 \cdot 10^{-3}$	$4.89 \cdot 10^{-5}$	$6.20 \cdot 10^{-3}$

Table 5.8: Differential production cross section $d\sigma/(dQ^2 dp_T d\eta)$ in fb GeV^{-3} for D^* mesons in deep-inelastic two-photon-scattering with Weizsäcker-Williams and beamstrahlung photon spectrum for ILC, distribution in p_T at $Q^2 = 10\,\text{GeV}^2$.

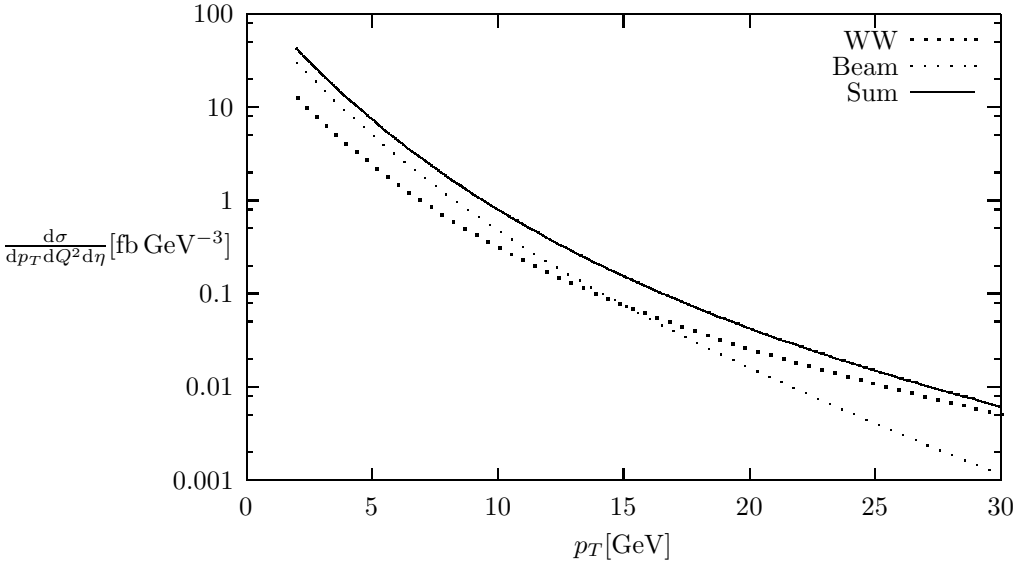

Figure 5.10: Differential production cross section $d\sigma/(dQ^2 dp_T d\eta)$ in fb GeV^{-3} for D^* mesons in deep-inelastic two-photon-scattering with Weizsäcker-Williams (thick-dotted) and beamstrahlung (thin-dotted) photon spectrum for ILC, distribution in p_T at $Q^2 = 10\,\text{GeV}^2$.

p_T[GeV]	Direct WW	Resolved WW	Direct Beam	Resolved Beam	Sum
2	0.149	1.10	0.283	2.31	3.84
6	0.103	0.0754	0.228	0.137	0.543
10	0.0317	0.0123	0.0520	0.0154	0.111
14	0.0125	$3.27 \cdot 10^{-3}$	0.0145	$2.81 \cdot 10^{-3}$	0.0331
18	$5.80 \cdot 10^{-3}$	$1.21 \cdot 10^{-3}$	$4.70 \cdot 10^{-3}$	$7.40 \cdot 10^{-4}$	0.0124
22	$2.96 \cdot 10^{-3}$	$4.92 \cdot 10^{-4}$	$1.60 \cdot 10^{-3}$	$1.98 \cdot 10^{-4}$	$5.25 \cdot 10^{-3}$
26	$1.68 \cdot 10^{-3}$	$2.24 \cdot 10^{-4}$	$6.17 \cdot 10^{-4}$	$5.70 \cdot 10^{-5}$	$2.58 \cdot 10^{-3}$
30	$1.00 \cdot 10^{-3}$	$1.10 \cdot 10^{-4}$	$2.36 \cdot 10^{-4}$	$1.65 \cdot 10^{-5}$	$1.37 \cdot 10^{-3}$

Table 5.9: Differential production cross section $d\sigma/(dQ^2 dp_T d\eta)$ in fb GeV^{-3} for D^* mesons in deep-inelastic two-photon-scattering with Weizsäcker-Williams and beamstrahlung photon spectrum for ILC, distribution in p_T at $Q^2 = 30\,\text{GeV}^2$.

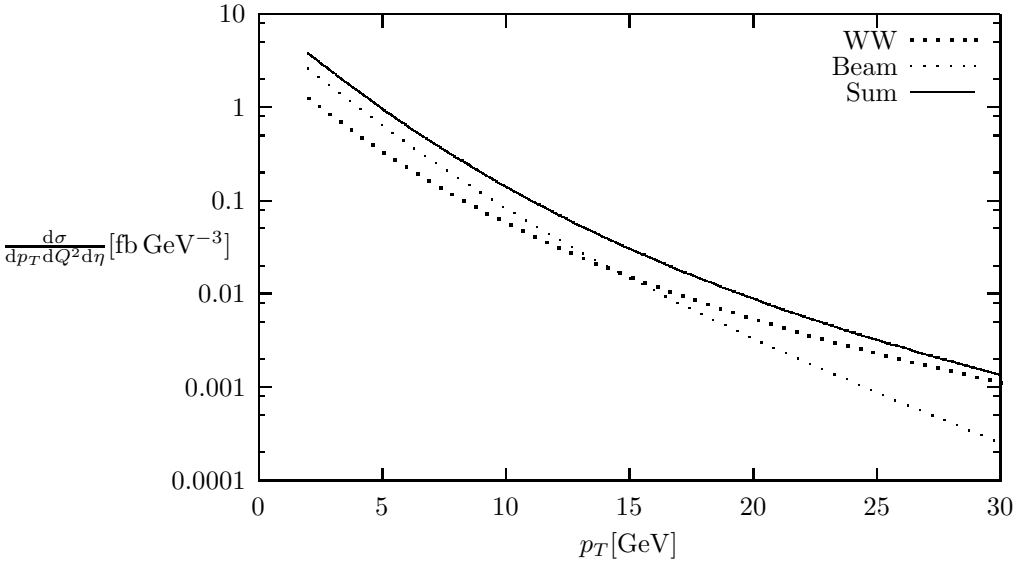

Figure 5.11: Differential production cross section $d\sigma/(dQ^2 dp_T d\eta)$ in fb GeV^{-3} for D^* mesons in deep-inelastic two-photon-scattering with Weizsäcker-Williams (thick-dotted) and beamstrahlung (thin-dotted) photon spectrum for ILC, distribution in p_T at $Q^2 = 30\,\text{GeV}^2$.

$\sim 10^4$. As a consequence the cross sections start lower for small p_T than the ones from the e^-e^+ mode but are higher for larger values of p_T. We also see that we are in a kinematic area where the resolved contribution is higher at $p_T = 2\,\text{GeV}$. However at $p_T = 30\,\text{GeV}$ it merely contributes $\sim 10\%$. The Q^2 dependence is similar to the e^-e^+ mode.

We pick the case with $Q^2 = 10\,\text{GeV}^2$ for further comparisons. In Table 5.13 we have listed the sum from Table 5.11 together with the leading order result and a NLO calculation where we have used the FFs without mass effects. We have already seen for DIS predictions that the NLO contribution can be several times higher than the Born result. This is also true here, where the NLO result is approximately 10 times higher than the Born result. The cause of this is probably the inelastic contribution which has its leading order at the overall NLO.

The mass effects in the FFs have a small impact. When calculating with our FF set without mass effects we get a result that is $\sim 2 - 3\%$ higher, which is the expected effect after our earlier comparisons of the FFs.

Finally we have repeated the calculations for all three spectra with $Q^2 = 10\,\text{GeV}^2$ with the FFs for the D^+ and for the D^0 meson respectively. The results for the D^0 meson can be found in Table 5.14 and Figure 5.15, the numbers for the D^+ meson are listed in Table 5.15 and plotted in Figure 5.16.

Using the WW and beamstrahlung spectra the D^0 production cross section is roughly twice as large as the one for D^* production. This can be attributed to the branching fraction of $c \to D^0$ and is expected. We find an interesting behaviour for the Compton spectrum: Here we see the factor 2 for the small p_T values, but for larger p_T the two cross sections approach each other until the D^0 cross section is only $\sim 10\%$ higher for $p_T = 30\,\text{GeV}$. It seems that in the latter case the different forms of the FFs play a larger role.

p_T[GeV]	Direct WW	Resolved WW	Sum
2	117	134	251
6	18.8	9.36	28.2
10	6.76	2.14	8.90
14	3.27	0.731	4.00
18	1.85	0.304	2.15
22	1.14	0.142	1.28
26	0.746	0.0717	0.818
30	0.504	0.0380	0.542

Table 5.10: Differential production cross section $\mathrm{d}\sigma/(\mathrm{d}Q^2\mathrm{d}p_T\mathrm{d}\eta)$ in $\mathrm{fb\,GeV^{-3}}$ for D^* mesons in deep-inelastic two-photon-scattering with Compton photon spectrum for $e\gamma$ mode of ILC, distribution in p_T at $Q^2 = 2.5\,\mathrm{GeV}^2$.

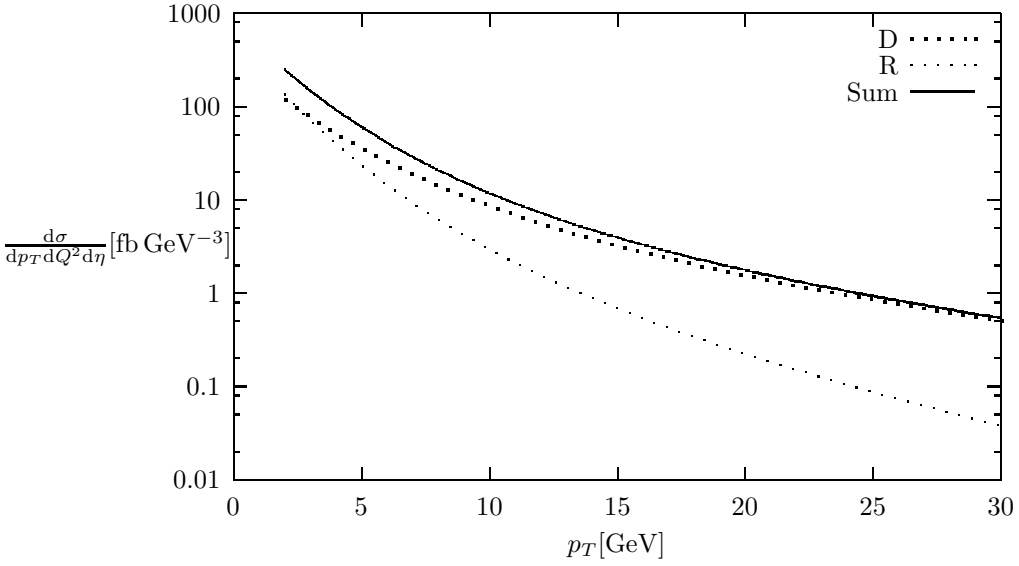

Figure 5.12: Differential production cross section $\mathrm{d}\sigma/(\mathrm{d}Q^2\mathrm{d}p_T\mathrm{d}\eta)$ in $\mathrm{fb\,GeV^{-3}}$ for D^* mesons in deep-inelastic two-photon-scattering with Compton photon spectrum for $e\gamma$ mode of ILC, distribution in p_T at $Q^2 = 2.5\,\mathrm{GeV}^2$. Direct contribution as thick-dotted line, resolved contribution as thin-dotted line and sum as solid line.

p_T[GeV]	Direct WW	Resolved WW	Sum
2	7.40	20.6	28.0
6	1.95	1.41	3.36
10	0.763	0.313	1.08
14	0.383	0.107	0.490
18	0.218	0.0451	0.263
22	0.135	0.0217	0.157
26	0.0891	0.0113	0.100
30	0.0604	$6.33 \cdot 10^{-3}$	0.0667

Table 5.11: Differential production cross section $\mathrm{d}\sigma/(\mathrm{d}Q^2\mathrm{d}p_T\mathrm{d}\eta)$ in $\mathrm{fb\,GeV}^{-3}$ for D^* mesons in deep-inelastic two-photon-scattering with Compton photon spectrum for $e\gamma$ mode of ILC, distribution in p_T at $Q^2 = 10\,\mathrm{GeV}^2$.

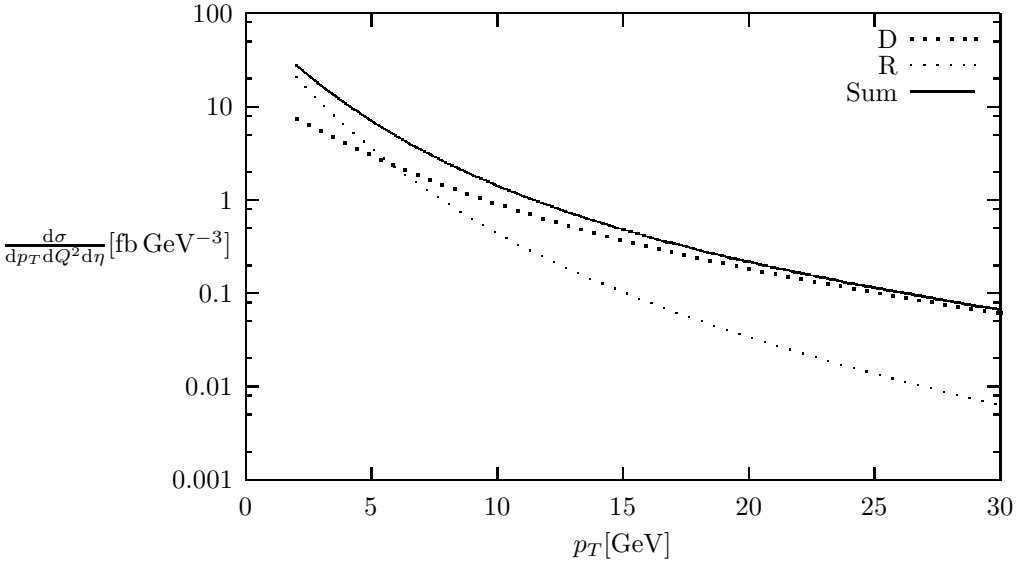

Figure 5.13: Differential production cross section $\mathrm{d}\sigma/(\mathrm{d}Q^2\mathrm{d}p_T\mathrm{d}\eta)$ in $\mathrm{fb\,GeV}^{-3}$ for D^* mesons in deep-inelastic two-photon-scattering with Compton photon spectrum for $e\gamma$ mode of ILC, distribution in p_T at $Q^2 = 10\,\mathrm{GeV}^2$. Direct contribution as thick-dotted line, resolved contribution as thin-dotted line and sum as solid line.

p_T[GeV]	Direct WW	Resolved WW	Sum
2	0.493	4.16	4.65
6	0.318	0.352	0.670
10	0.143	0.0819	0.225
14	0.0753	0.0284	0.104
18	0.0442	0.0123	0.0565
22	0.0278	$6.10 \cdot 10^{-3}$	0.0339
26	0.0183	$3.21 \cdot 10^{-3}$	0.0215
30	0.0126	$1.86 \cdot 10^{-3}$	0.0145

Table 5.12: Differential production cross section $\mathrm{d}\sigma/(\mathrm{d}Q^2\mathrm{d}p_T\mathrm{d}\eta)$ in $\mathrm{fb\,GeV^{-3}}$ for D^* mesons in deep-inelastic two-photon-scattering with Compton photon spectrum for $e\gamma$ mode of ILC, distribution in p_T at $Q^2 = 30\,\mathrm{GeV}^2$.

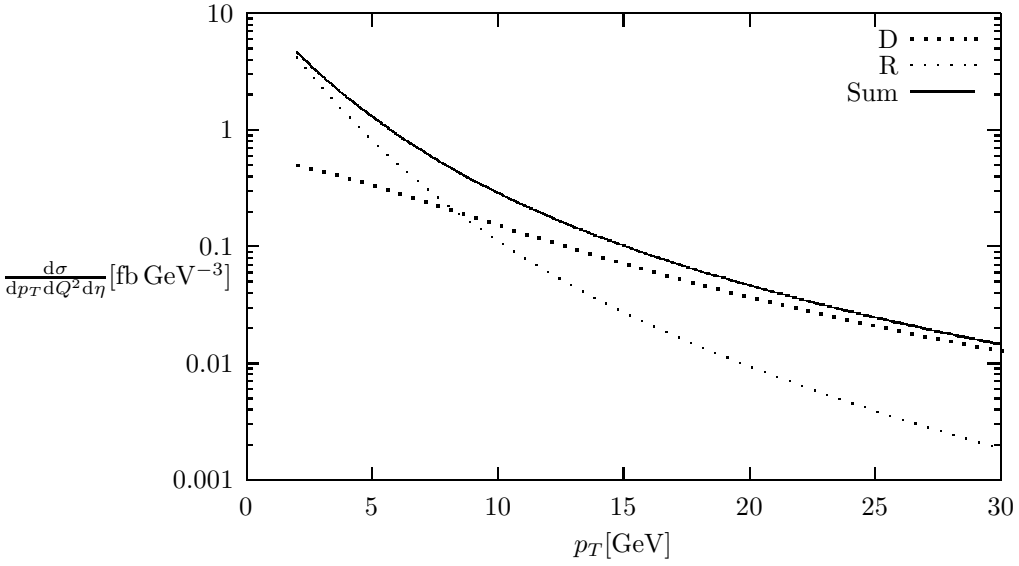

Figure 5.14: Differential production cross section $\mathrm{d}\sigma/(\mathrm{d}Q^2\mathrm{d}p_T\mathrm{d}\eta)$ in $\mathrm{fb\,GeV^{-3}}$ for D^* mesons in deep-inelastic two-photon-scattering with Compton photon spectrum for $e\gamma$ mode of ILC, distribution in p_T at $Q^2 = 30\,\mathrm{GeV}^2$. Direct contribution as thick-dotted line, resolved contribution as thin-dotted line and sum as solid line.

p_T[GeV]	NLO with mass	LO with mass	NLO with $m = 0$
2	28.0	7.62	28.5
6	3.36	0.518	3.43
10	1.08	0.131	1.10
14	0.490	0.0523	0.499
18	0.263	0.0265	0.269
22	0.157	0.0155	0.160
26	0.100	0.0102	0.103
30	0.0667	0.00731	0.0684

Table 5.13: Differential production cross section $\mathrm{d}\sigma/(\mathrm{d}Q^2\mathrm{d}p_T\mathrm{d}\eta)$ in $\mathrm{fb\,GeV}^{-3}$ for D^* mesons in deep-inelastic two-photon-scattering with Compton photon spectrum for $e\gamma$ mode of ILC, distribution in p_T at $Q^2 = 10\,\mathrm{GeV}^2$. Comparison of NLO with GM-VFNS FFs, LO with GM-VFNS and NLO with ZM-VFNS.

p_T[GeV]	WW	Beam	Sum	Compton
2	30.4	73.3	104	56.3
6	2.29	4.85	7.14	5.18
10	0.503	0.774	1.28	1.47
14	0.173	0.185	0.358	0.622
18	0.0739	0.0536	0.128	0.318
22	0.0362	0.0174	0.0536	0.183
26	0.0194	0.00609	0.0255	0.114
30	0.0109	0.00204	0.0129	0.0740

Table 5.14: Differential production cross section $\mathrm{d}\sigma/(\mathrm{d}Q^2\mathrm{d}p_T\mathrm{d}\eta)$ in $\mathrm{fb\,GeV}^{-3}$ for D^0 mesons in deep-inelastic two-photon-scattering with WW, beamstrahlung, the sum of the two latter and Compton photon spectrum for $e\gamma$ mode of ILC, distribution in p_T at $Q^2 = 10\,\mathrm{GeV}^2$.

The production cross sections for the D^+ mesons are $\sim 5 - 10\%$ larger than the ones for the D^* meson, where the larger difference is found for small p_T values. This is true for all three spectra, so we don't find a shift in the ratio when using the Compton spectrum.

5.4 Applications in the literature

In the literature, our FFs have been applied for different processes. We briefly present the results for further discussion.

5.4.1 Hadroproduction of charmed hadrons

In [82] Kniehl, Kramer, Schienbein and Spiesberger have calculated the production cross sections for D^0, D^+ and D^* mesons in hadroproduction in the GM-VFNS, using the global fit FF set from this work. However parts of the partonic cross section are calculated with $m = 0$. The result is compared with experimental data from the CDF collaboration [83]. The CDF collaboration has measured events at the Tevatron collider, where $p\bar{p}$-scattering was measured at $\sqrt{s} = 1.96\,\mathrm{TeV}$ within the kinematical region $|\eta| < 1$.

The theory prediction is calculated with the CTEQ6.5 proton PDFs [74]. In the work [82] variations of the PDFs are tested for different models of the intrinsic charm

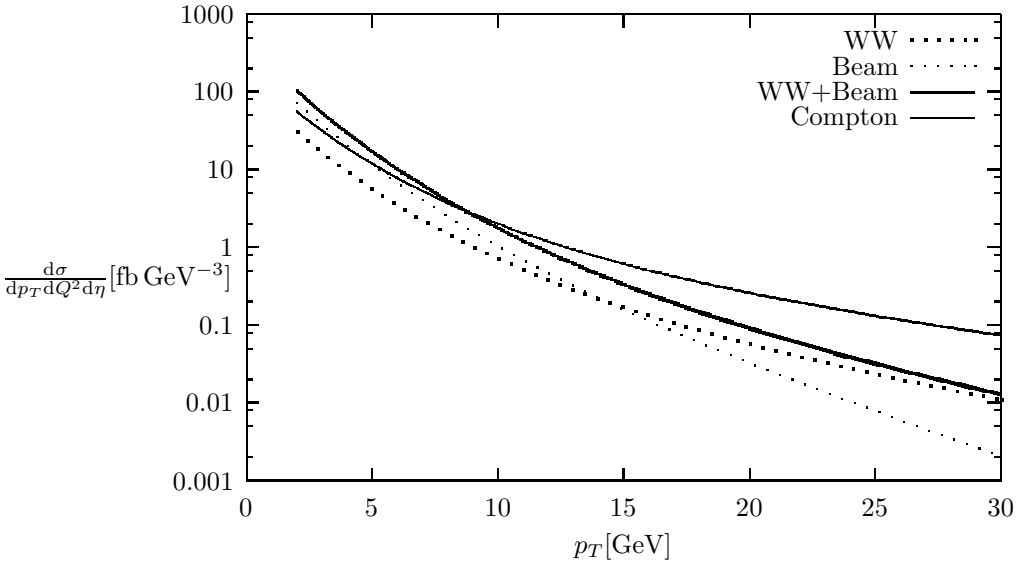

Figure 5.15: Differential production cross section $d\sigma/(dQ^2 dp_T d\eta)$ in fb GeV^{-3} for D^0 mesons in deep-inelastic two-photon-scattering with WW spectrum (thick-dotted), beamstrahlung spectrum (thin-dotted), the sum of the two latter (bold) and Compton photon spectrum (solid) for ILC, distribution in p_T at $Q^2 = 10\,\mathrm{GeV}^2$.

p_T[GeV]	WW	Beam	Sum	Compton
2	14.0	33.5	47.5	31.3
6	1.08	2.27	3.35	3.70
10	0.237	0.370	0.607	1.18
14	0.0815	0.0894	0.171	0.531
18	0.0351	0.0263	0.0614	0.286
22	0.0173	0.00846	0.0258	0.170
26	0.00930	0.00304	0.0123	0.108
30	0.00523	0.00105	0.00628	0.0711

Table 5.15: Differential production cross section $d\sigma/(dQ^2 dp_T d\eta)$ in fb GeV^{-3} for D^+ mesons in deep-inelastic two-photon-scattering with WW, beamstrahlung, the sum of the two latter and Compton photon spectrum for $e\gamma$ mode of ILC, distribution in p_T at $Q^2 = 10\,\mathrm{GeV}^2$.

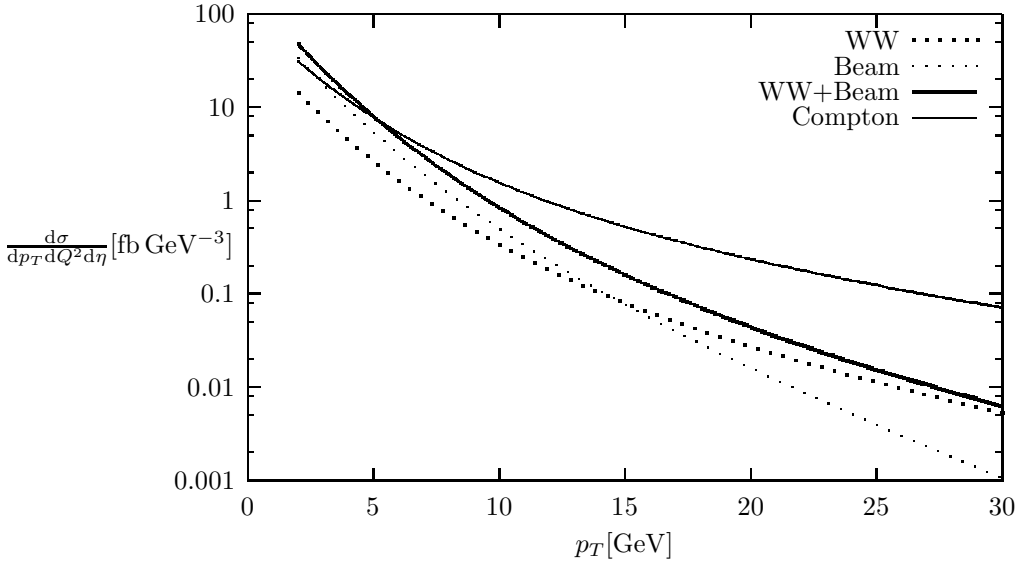

Figure 5.16: Differential production cross section $d\sigma/(dQ^2 dp_T d\eta)$ for D^+ mesons in deep-inelastic two-photon-scattering with WW spectrum (thick-dotted), beamstrahlung spectrum (thin-dotted), the sum of the two latter (bold) and Compton photon spectrum (solid) for ILC, distribution in p_T at $Q^2 = 10\,\mathrm{GeV}^2$.

content of the proton. We focus on the main predictions with $f_c(\xi, \mu_f = m_c) = 0$ in Figs.(5.17) and (5.18). The theory uncertainty is evaluated by variation of the scales, which are $\mu_R = \xi_R m_T$ and $\mu_f = \mu'_f = \xi_F m_T$. The main values are $\xi_R = 1$ and $\xi_F = 1$, which are variied between $1/2 < \xi_R, \xi_F < 2$.

The data points lie within the theory band, which is a progress over the older analysis [13] by the same authors, where the main difference is due to the new FFs based on BELLE and CLEO data. In the older publication the majority of the data points lies over the error bands of the theory, which is especially true for the D^+-production. These improvements allow the authors to examine the influence of different models of the charm content of the proton in [82].

The study of hadroproduction also includes predictions for proton-proton-collisions the RHIC collider, which operates at a CMS energy of $\sqrt{s} = 200\,\mathrm{GeV}$. Unfortunately the only available analysis for the production of charmed hadrons covers only the range $p_T < 2.5\,\mathrm{GeV}$, which is problematic for the theory. A direct comparison of theory and experiment is therefore not yet possible. We show the figures from [82] for $\sqrt{s} = 200\,\mathrm{GeV}$ in Fig.(5.19) and for the high-energy mode of RHIC at $\sqrt{s} = 500\,\mathrm{GeV}$ in Fig.(5.20). In Fig.(5.20(b)) several variations of the calculation are plotted normalized to the default prediction. In the variations different models for the intrinsic charm content of the proton were used which were taken from [84].

5.4.2 D^*-meson production in ep scattering at low virtuality

Kramer and Spiesberger have calculated the D^*-meson production in ep scattering at low Q^2 [85] in comparison with HERA data from [86]. The authors have used the GM-VFNS and applied the Belle/CLEO FF set from this work to describe the fragmentation part of the cross section. Using the Belle/CLEO set leads in their

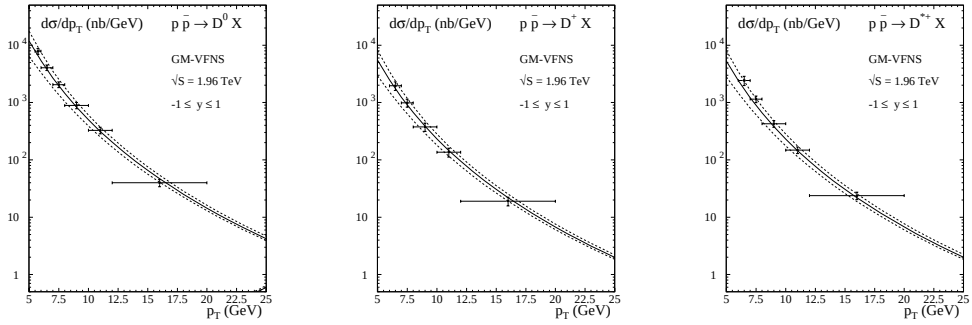

Figure 5.17: p_T distributions $\mathrm{d}\sigma/\mathrm{d}p_T$ of $p + \overline{p} \to H_c + X$ with (a) $H_c = D^0$, (b) $H_c = D^+$, and (c) $H_c = D^{*+}$ for $\sqrt{s} = 1.96$ TeV evaluated at NLO in the GM-VFNS in comparison with experimental data from CDF [83]. The solid line represents the theory prediction for $\mu_F, \mu_R = 1$, while the dashed lines give the maximum deviations through variation of the scales.

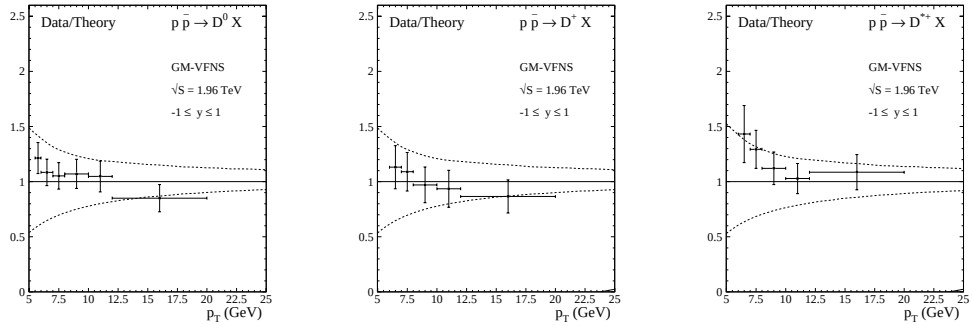

Figure 5.18: Same as in Figs. 5.17(a)–(c), but normalized to the default predictions.

case to a $25 - 30\%$ higher photoproduction cross section compared to the global fit set.

The low Q^2 leads to the following treatment of the virtual photon: It enters the calculation as a real photon, where the spectrum is given by the Weizsäcker-Williams approximation. The range of Q^2 is given by the cuts applied in the HERA analysis, which are $Q^2_{\mathrm{min}} = 0.05\,\mathrm{GeV}^2$ and $Q^2_{\mathrm{max}} = 0.7\,\mathrm{GeV}^2$. This spectrum is convoluted with the cross section for photoproduction $\gamma + P \to D^* + X$.

Furthermore the result is the sum of direct and resolved contributions. As above, for the resolved contribution the photon is treated like a hadron in the sense, that it contains partons. In the case of [85] the photon PDF set GRV92 [87] is used. For the proton the CTEQ6.6M set is used [88].

The renormalization and factorization scales are $\mu_R = \xi_R m_T$ and $\mu_F = \mu'_F = \xi_F m_T$ with the transversal mass $m_T = \sqrt{m^2 + p_T^2}$. The main values are $\xi_R = \xi_F = 1$, which are varied between $1/2 < \xi_R, \xi_F < 2$ with the added condition $1/2 < \xi_R/\xi_F < 2$ to estimate the scale dependence of the theory prediction.

The exact values of the experimental analysis are a proton energy of $E_p = 920\,\mathrm{GeV}$ and an electron energy of $E_e = 27.5\,\mathrm{GeV}$. The inelasticity varies in the

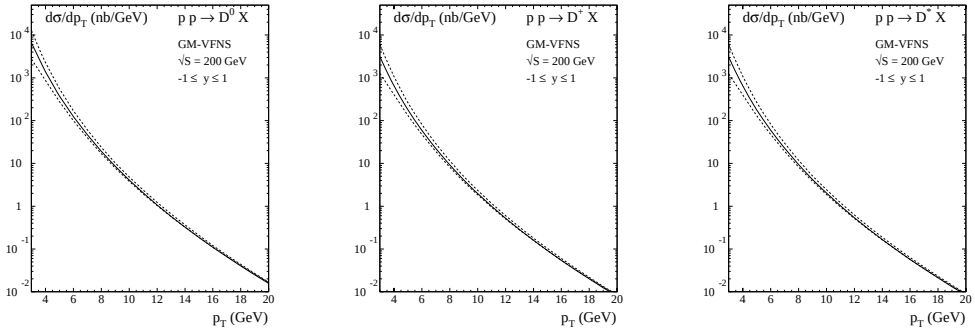

Figure 5.19: Same as in Fig. 5.17, but for pp collisions with $\sqrt{s} = 200$ GeV.

range $0.02 < y_e < 0.85$. The range of the transversal momentum is $1.5\,\mathrm{GeV} < p_T^L < 9\,\mathrm{GeV}$, and the rapidity is limited to $|\eta_L| < 1.5$.

Theory and experimental data are compatible within the errors. The largest deviations can be found in the lower bins, where also the scale dependence is bigger except for the distribution in η_L. This deviations stem from terms with massless charm quarks in the proton PDF. We observe in the p_T distribution that the theory and the experiment agree for larger values of p_T.

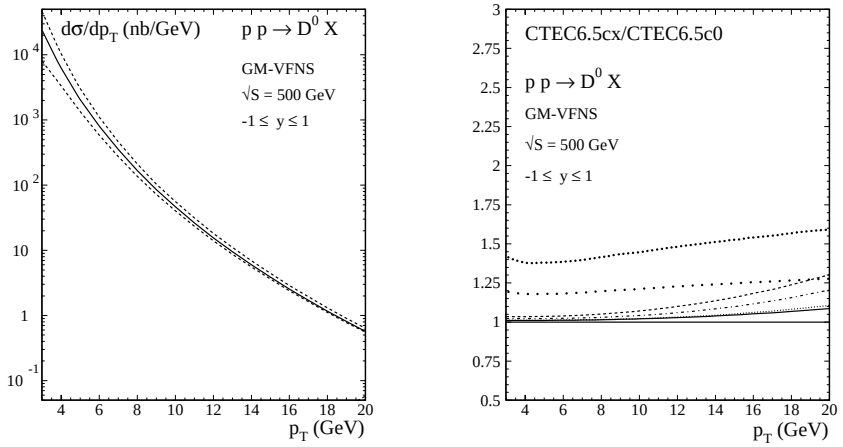

(a) (b)

Figure 5.20: Ssame as in Figs. 5.19(a), but for $\sqrt{s} = 500$ GeV. In (b) variations of the cross section with different intrinsic charm content of the protons are plotted normalized to (a). The variations are intrinsic charm parametrizations from [84] with the parameter $n = 1$ (solid line), $n = 2$ (dashed line), $n = 3$ (densely dotted line), $n = 4$ (dot-dashed line), $n = 5$ (scarcely dotted line) and $n = 6$ (dotted line).

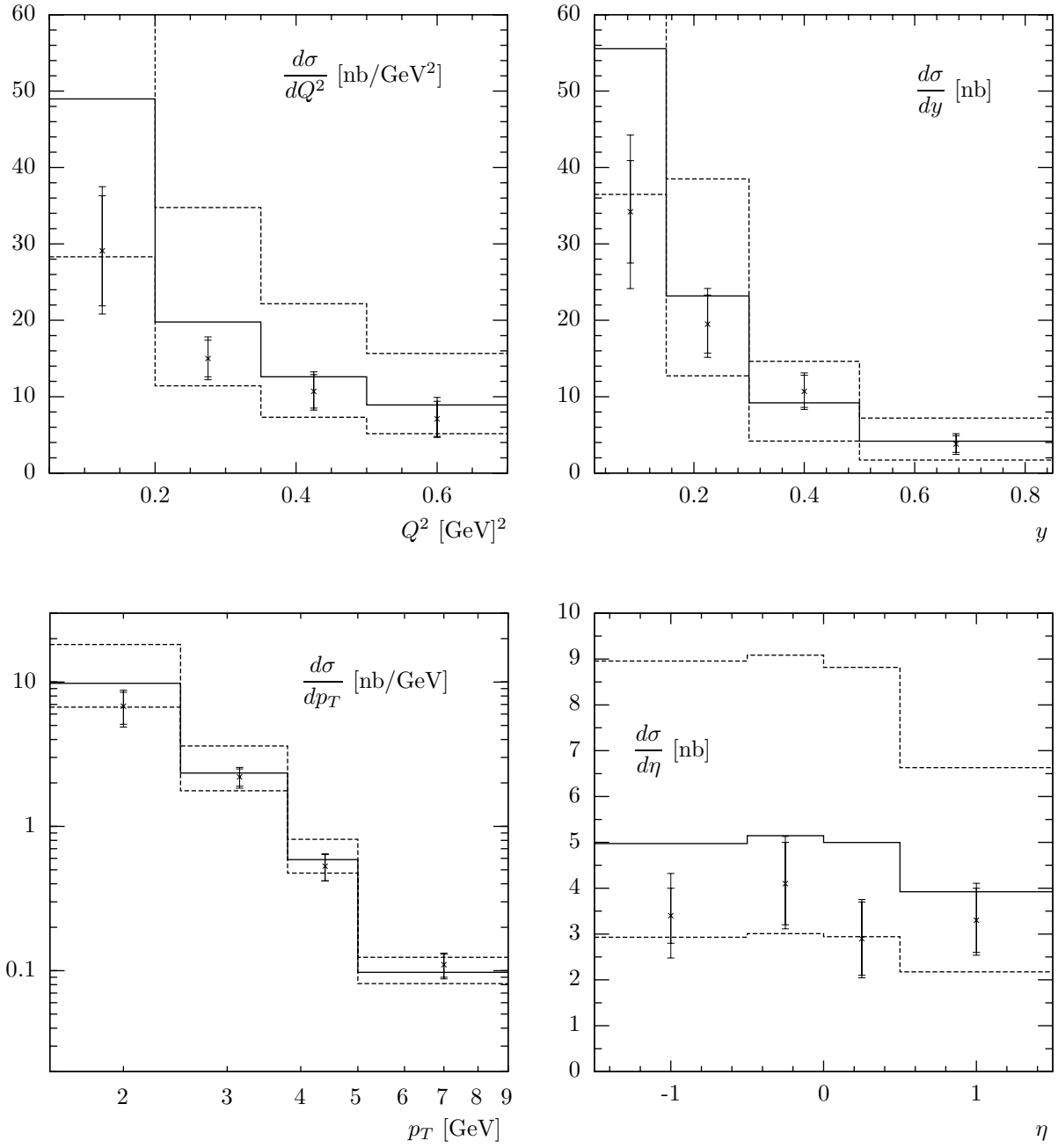

Figure 5.21: Differential cross sections for D^*-meson production in low-Q^2 ep scattering, compared with experimental results from the ZEUS collaboration [86]. The default choice for the scale parameters is $\xi_R = \xi_F = 1$ (full lines) and error bands are obtained by varying ξ_R and ξ_F. The kinematic range is given by $0.05 < Q^2 < 0.7$ GeV^2, $0.02 < y < 0.85$, $1.5 < p_T < 9.0$ GeV and $|\eta| < 1.5$.

Chapter 6

Summary

We have given an introduction to perturbative QCD, where we have focussed on the problem of infrared singularities. The structure of cross sections with collinear singularities motivates the definition of splitting functions and leads to the DGLAP evolution equations for distribution functions. Then we have given an overview over several factorization schemes. As all schemes in perturbative QCD they share the concept of factorization of the QCD cross section in a partonic cross section and non-perturbative PDFs and FFs. We have then focused on the GM-VFNS, which we use in our work to analyse the production of heavy hadrons. The scheme's defining properties are the use of a scale dependent number of active quark flavors and the construction of the subtraction terms. These terms lead to a transition to the well-known ZM-VFNS for larger scales when the massless limit becomes valid, but leave finite mass terms in the partonic cross sections for accurate results when the scale is near the heavy quark masses. In our work the masses also serve as transition points for the number of active flavors.

We have presented the calculation of the electron-positron-annihilation semi-inclusive cross section, which is the scattering process best suited for the extraction of fragmentation functions. The cross section was calculated including the NLO QCD corrections and the masses of heavy quarks. With our independent calculation we have verified the literature result [5] and demonstrated a complete analytical calculation of a parton cross section.

The starting point of the calculation are the contributing Feynman graphs. We have shown how the cross section can be written as a product of a lepton tensor and a hadron tensor. The lepton tensor has been written in terms of projectors. After that we have focussed on the hadron tensor, which contains all strong corrections and the phase space of the outgoing particles. The NLO corrections consist of virtual and real corrections, which are only combined after the integration over their respective phase spaces. Throughout the calculation we have used dimensional regularization to handle singularities.

Since the number of contributing Feynman graphs is small, we have calculated the respective matrix element contributions from the Feynman rules by hand. For the virtual corrections, a renormalization and thus the calculation of a counterterm is necessary. The evaluation of the squared matrix element has been done with the help of FORM, which has multiplied the matrix element contributions and calculated the traces of the fermions' Dirac chains. This has been combined with the phase space factors, that we have calculated for two and for three outgoing particles respectively including quark masses. For the integration of the phase space we have applied pole subtraction to handle the seperation of the result in delta and plus distribution parts in the case of the real corrections. The calculated cross section is given in the equations (3.81) to (3.87).

We have then calculated the massless limit of the result, which requires special care to reproduce the distributions correctly. Together with the ZM-VFNS result from the literature, this has lead to the GM-VFNS subtraction terms for electron-positron-annihilation (3.111).

This result has been used for the extraction of the fragmentation functions from data of D^0, D^+ and D^* heavy meson production. The data in question is the result of the analysis from the Belle [25], CLEO [26], OPAL [19, 20] and ALEPH [21] collaborations, where the ALEPH data is available only for D^* production. Both Belle and CLEO have analysed data from B factories at a CMS energy of $\sqrt{s} = 10.5\,\mathrm{GeV}$, where we have to take initial state radiation into account. The ISR reduces the CMS energy of the process through radiation of photons from the initial electron or positron and as a consequence enhances the cross section. We have derived an expression to include this effect in our theory prediction. Thanks to some reasonable approximations it is efficient enough to be included in the fit routine without slowing it down too much.

We have extracted FF sets for all three particles with and without masses. The selected ansatz for the FFs is the Bowler parametrisation, which has for now proven to be the most accurate parametrization close to the threshold. In each case we have performed a fit of the FFs to the combined Belle/CLEO data, one to the data of the LEP experiments ALEPH and OPAL (at $\sqrt{s} = M_Z$) and one global fit using all those data sets and therefore testing the evolution of the FFs. All fits have worked satisfactory with some room for improvement.

The global fits lead to $\overline{\chi^2}$ values - χ^2 divided by the degrees of freedom - between 2 and 6.9, where the worse fits can partially be explained by incompatible data sets. Regarding that even the data at one scale is not completely compatible, the fit result including evolution is satisfactory. In comparison the fit result in the ZM-VFNS is slightly worse with $\overline{\chi^2}$ values which are approximately 10% higher, which indicates that the treatment of quark masses is sensible. The main problem of the global fits is visible at the LEP scale: The contribution of hadrons produced from charm quarks, which is determined mainly by Belle data, is too high to describe the LEP data. This can either be a problem of the theory or incompatibility of the data sets from different experiments.

The fits to the Belle/CLEO data reaches a $\overline{\chi^2}$ value of 1.3 for D^+ and 3.2 and 3.7 for D^0 and D^* respectively. It is interesting to see that the quality of the fits without masses are almost equal. So the changes in the cross section due to heavy quark masses can be compensated by a shift in the parameters of the FFs. We have to refer to the global fits to show that the inclusion of the masses leads to a more succesful description.

At the LEP scale we have not expected a difference between the GM-VFNS and the ZM-VFNS, because of the masses being negligible at the higher scale, and as expected have only found minor differences. The fits for D^0 and D^+ to OPAL data reach average χ^2 values of 0.8 and 0.5 respectively. The fit quality for the D^* data is worse with $\overline{\chi^2} = 2.1$, but here we have combined ALEPH and OPAL data sets, which aren't completely compatible.

We have further studied the impact of masses on the results for D^+ production. The result is that the influence of the charm quark masses is only small, e.g. a few percent on the cross section. Instead the big effect is the hadron mass m_H. The height of the peak of the $c \to D^+$ FF with hadron masses is raised by $\sim 20\%$, both with quark masses and without quark masses in the parton cross section.

Finally we have calculated the branching fractions and the average energy fraction passed from parton to hadron for each FF at different scales. Here we find that the differences are very small when comparing GM-VFNS and ZM-VFNS. The comparison of differents fit sets is more conclusive: The branching fractions are up to 20% higher for the pure Belle/CLEO fits compared to the corresponding

ALEPH/OPAL fits, which we have already observed in the high charm contribution at the M_Z scale in the global fit. Also the average energy fractions are $\sim 5-10\%$ higher in the case of the Belle/CLEO fits. Not surprisingly the branching fractions and average momenta calculated from the theory are substantially higher compared to experimental values from ALEPH and OPAL, while the theory values and available Belle and CLEO energy fraction values are only slightly incompatible.

The most important results of the FF extractions are:

- In contrast to older FF extractions of our group, which relied solely on LEP data, we have used the Bowler parametrization. In comparison to the Peterson and the power ansatz which worked well at the LEP scales, the Bowler form has proven far superior for the B factory data near the mass thresholds and has led unlike the other two parametrizations to acceptable fits. The only other parametrization which leads to similar - but still higher - $\overline{\chi^2}$ values is the Lund parametrization, which is similar to Bowler.

- The inclusion of masses leads to improvements of the global fit. We have found that the influence of the hadron mass in the kinematics is the main factor, while the influence of the heavy quark's masses only amounts to a few percent.

- The global fit and the branching fractions indicate, that either the normalization of Belle/CLEO and ALEPH/OPAL experiments are not compatible or that evolution does not work perfectly. The charm quark contribution, mostly fixed by the Belle data, is too high in the cross sections for the LEP data.

In conclusion we strongly encourage the use of the Bowler parametrization for future works. With our new FFs theory predictions with sizable contributions from scales $\mu \approx m_Q$ should have higher accuracies. More tests of the FFs are desirable to determine whether the problem in the global fit arises from the experimental data or from the evolution of the FFs.

Finally we have applied the new fragmentation functions to deep-inelastic processes using the result and program by Daleo et.al [30], where we have modified the program where necessary. The Daleo result is calculated in the ZM-VFNS, so the mass terms in the parton cross sections are missing. However, since the GM-VFNS has a smooth transition into the ZM-VFNS in the massless limit, this should suffice for first applications until GM-VFNS cross sections are calculated.

The first application was the usual electron-proton-scattering, where we have compared theory predictions to data from the HERA experiment [31]. We have calculated differential cross section distributions in x_B and in Q^2. For low values of x_B, starting with $2.8 \cdot 10^{-5}$, the theory prediction is too high by $\sim 30\%$. The discrepancy gets smaller for higher values of x_B, where we have found a bin with compatible theoretical and experimental results around $x_B = 0.002$. The picture is similar for the distribution in Q^2, where we started at $Q^2 = 2\,\mathrm{GeV}^2$ and found a theory prediction which is 50% too high. For the last two bins with $Q^2 > 17.6\,\mathrm{GeV}^2$ theory and experiment are compatible. The lower bins are already at the border of the kinematic region where the theory is applicable. $Q^2 = 2\,\mathrm{GeV}^2$ might be better considered in the photoproduction mode, while $p_T < 2\,\mathrm{GeV}$ is perhaps a too small cut on p_T when using ZM-VFNS parton cross sections.

This discrepancy overshadows the differences between different theory approaches. We have applied the global fit FFs from the GM-VFNS and from the ZM-VFNS. The predictions with the GM-VFNS FFs are $2-3\%$ lower than the one with the ZM-VFNS FFs, which is consistent with the branching fractions. Unfortunately in this case the difference is of the same magnitude as the difference due to a different choise of scales.

We have then made a number of further changes to the program in order to calculate predictions for deep-inelastic two-photon-scattering. First we have introduced an additional convolution with a photon spectrum. For the resolved contribution we have simply replaced the proton PDFs with photon PDFs. For the direct contribution we have taken the incoming gluon and replaced it with a photon, which is possible by adjusting the coupling factors and taking out the non-Abelian parts.

With the modified program we have calculated the differential cross section $\mathrm{d}\sigma/(\mathrm{d}Q^2\mathrm{d}p_T\mathrm{d}\eta)$ for LEP1 data in the Tables 5.4 to 5.6. The highest value for the cross section is $927\,\mathrm{fbGeV}^{-3}$ for $\eta = 0$, $p_T = 1\,\mathrm{GeV}$ and $Q^2 = 2.5\,\mathrm{GeV}^2$,which seems rather low compared to the integrated luminosity of the LEP1 run at $\sim 170\,\mathrm{pb}^{-1}$ [89].

For LEP2 we have calculated a theory result for comaprison with the experimental result from [33]. For the bin in the range $0.0014 < x_B < 0.1$ we have calculated a cross section of 1.43 pb, which is a bit too low compared to the measured value of $3.1 \pm 1.0 \pm 0.5\,\mathrm{GeV}$.

For the ILC we have calculated differential D^* production cross sections in the Tables 5.7 to 5.9 for the e^-e^+ mode with the Weizsäcker-Williams photon spectrum and with a beamstrahlung spectrum. Beamstrahlung dominates for low values of p_T up to $\sim 15\,\mathrm{GeV}$ before the contribution from WW photons becomes more important.

We have repeated the calculations with a Compton spectrum for thr $e\gamma$ mode and have listed the results in the Tables 5.10 to 5.12. In the $e\gamma$ mode we find lower cross sections for small p_T, but it does not fall off as quickly when going to higher values of p_T. Overall we have to expect less events in the $e\gamma$ due to smaller cross sections and reduced luminosity. The $e\gamma$ mode might still be interesting for this kind of processes thanks to less background and less strict tagging conditions.

Further calculations for comparison show that NLO calculations - the leading order for inelastic contributions - are mandatory for the process, since the NLO parts are several times higher than the Born part. Using the FFs from our ZM-VFNS fit in contrast to our GM-VFNS FFs only leads to a difference of $2 - 3\%$.

We have also run calculations for the D^0 and D^+ mesons in Tables 5.14 and 5.15. Mostly the difference to the D^* cross section can be attributed to the different branching fractions regardless of the differences in the curves of the FFs. An exception is the D^0 result when using a Compton spectrum: Here the cross section starts out as expected approximately two times higher than the D^* one for low p_T values, but is only $\sim 10\%$ higher for larger p_T values.

Finally we have shown with kind permission results from first works in the literature which make use of our new FFs. Reference [82] contains calculations for the hadroproduction of charmed hadrons in comparison with data from the Tevatron collider. And in reference [85] Kramer and Spiesberger have used them for deep-inelastic scattering at low virtuality in comparison with HERA data.

To summarize we have given first predictions for single-tagged D^* meson production at LEP1 and LEP2. For the former there is currently no analysis of the events in question, but we have used kinematic ranges from a similar analysis to have a comparable prediction. For LEP2 our calculation is almost compatible with the experimental result despite the unrealistic cross section for low p_T.

We have also given D meson production predictions for the e^-e^+ and the $e\gamma$ mode of the planned ILC. These numbers show the large contribution by beamstrahlung photons compared to WW photons especially in the low p_T region, which one can also see by comparing the respective spectrum functions. In the $e\gamma$ mode it can be said that the overall cross sections for our process are smaller than in the e^-e^+ mode, so our process is not especially suited for that mode.

The ILC predictions are of course rather rough. The exact parameters of this collider and its detectors are not yet decided. The beamstrahlung spectrum strongly depends on the beam geometry, which is a compromise out of maximising luminosity

and avoiding effects like beamstrahlung. The Compton spectrum depends on the achieved polarisations of the lepton and the laser beam. Further effects depend on the implementation of the laser near the beam interaction point.

On the theory side the calculation can also be refined in several ways. Firstly we have used a ZM-VFNS cross section and therefore have not included finite mass terms, which would affect the low p_T region with the cross sections the most. Secondly we have occasionally encountered numerical problems which could be approached in several ways: Having an analytical formula which still allows the implementation of cuts, finding a better suited integration algorithm or using optimisations for the kinematic region used in the analysis. And of course an estimation of the theoretical uncertainty is desirable, for which one has to be able to vary the scale without errors.

Still our results give an overview over the expected magnitude of heavy hadron production in deep-inelastic two-photon-scattering. Refinements can be made when more concrete ILC paramaters become available. Until then we have already seen the use of our new fragmentation functions in hadroproduction at Tevatron, so the application for hadroproduction at the Large Hadron Collider is likely. We hope our fragmentation functions help science in the analysis and precise prediction of heavy hadron production.

Bibliography

[1] P. Nason, S. Dawson and R. K. Ellis, Nucl. Phys. B **303** (1988) 607.

[2] P. Nason, S. Dawson and R. K. Ellis, Nucl. Phys. B **327** (1989) 49 [Erratum-ibid. B **335** (1990) 260].

[3] W. Beenakker, H. Kuijf, W. L. van Neerven and J. Smith, Phys. Rev. D **40** (1989) 54.

[4] W. Beenakker, W. L. van Neerven, R. Meng, G. A. Schuler and J. Smith, Nucl. Phys. B **351** (1991) 507.

[5] P. Nason and B. R. Webber, Nucl. Phys. B **421** (1994) 473 [Erratum-ibid. B **480** (1996) 755].

[6] W. K. Tung, S. Kretzer and C. Schmidt, J. Phys. G **28** (2002) 983 [arXiv:hep-ph/0110247].

[7] M. A. G. Aivazis, J. C. Collins, F. I. Olness and W. K. Tung, Phys. Rev. D **50** (1994) 3102 [arXiv:hep-ph/9312319].

[8] G. Kramer and H. Spiesberger, Eur. Phys. J. C **22** (2001) 289 [arXiv:hep-ph/0109167].

[9] G. Kramer and H. Spiesberger, Eur. Phys. J. C **28** (2003) 495 [arXiv:hep-ph/0302081].

[10] G. Kramer and H. Spiesberger, Eur. Phys. J. C **38** (2004) 309 [arXiv:hep-ph/0311062].

[11] B. A. Kniehl, G. Kramer, I. Schienbein and H. Spiesberger, Phys. Rev. D **71** (2005) 014018 [arXiv:hep-ph/0410289].

[12] B. A. Kniehl, G. Kramer, I. Schienbein and H. Spiesberger, Eur. Phys. J. C **41** (2005) 199 [arXiv:hep-ph/0502194].

[13] B. A. Kniehl, G. Kramer, I. Schienbein and H. Spiesberger, Phys. Rev. Lett. **96** (2006) 012001 [arXiv:hep-ph/0508129].

[14] B. A. Kniehl, G. Kramer, I. Schienbein and H. Spiesberger, Phys. Rev. D **77** (2008) 014011 [arXiv:0705.4392 [hep-ph]].

[15] B. Mele and P. Nason, Nucl. Phys. B **361** (1991) 626.

[16] S. Kretzer and I. Schienbein, Phys. Rev. D **58** (1998) 094035 [arXiv:hep-ph/9805233].

[17] S. Kretzer and I. Schienbein, Phys. Rev. D **59** (1999) 054004 [arXiv:hep-ph/9808375].

[18] M. Cacciari and S. Catani, Nucl. Phys. B **617** (2001) 253 [arXiv:hep-ph/0107138].

[19] G. Alexander *et al.* [OPAL Collaboration], Z. Phys. C **72** (1996) 1.

[20] K. Ackerstaff *et al.* (OPAL Collaboration), Eur. Phys. J. C **1**, 439 (1998) [arXiv:hep-ex/9708021].

[21] R. Barate *et al.* (ALEPH Collaboration), Eur. Phys. J. C **16**, 597 (2000) [arXiv:hep-ex/9909032].

[22] J. Binnewies, B. A. Kniehl, and G. Kramer, Phys. Rev. D **58**, 014014 (1998) [arXiv:hep-ph/9712482].

[23] B. A. Kniehl and G. Kramer, Phys. Rev. D **71**, 094013 (2005) [arXiv:hep-ph/0504058].

[24] B. A. Kniehl and G. Kramer, Phys. Rev. D **74**, 037502 (2006) [arXiv:hep-ph/0607306].

[25] R. Seuster *et al.* (Belle Collaboration), Phys. Rev. D **73**, 032002 (2006) [arXiv:hep-ex/0506068].

[26] M. Artuso *et al.* (CLEO Collaboration), Phys. Rev. D **70**, 112001 (2004) [arXiv:hep-ex/0402040].

[27] T. Kneesch, B. A. Kniehl, G. Kramer and I. Schienbein, Nucl. Phys. B **799** (2008) 34 [arXiv:0712.0481 [hep-ph]].

[28] M. Cacciari, P. Nason and C. Oleari, JHEP **0604** (2006) 006 [arXiv:hep-ph/0510032].

[29] G. Corcella and G. Ferrera, JHEP **0712** (2007) 029 [arXiv:0706.2357 [hep-ph]].

[30] A. Daleo, D. de Florian and R. Sassot, Phys. Rev. D **71** (2005) 034013 [arXiv:hep-ph/0411212].

[31] A. Aktas *et al.* [H1 Collaboration], Eur. Phys. J. C **51** (2007) 271 [arXiv:hep-ex/0701023].

[32] [ALEPH, L3 and OPAL Collaborations], Eur. Phys. J. C **23** (2002) 201.

[33] G. Abbiendi *et al.* [OPAL Collaboration], Phys. Lett. B **539** (2002) 13 [arXiv:hep-ex/0206021].

[34] J. Brau *et al.*, "International Linear Collider reference design report. 1: Executive summary. 2: Physics at the ILC. 3: Accelerator. 4: Detectors,"

[35] P. Aurenche, M. Fontannaz and J. P. Guillet, Eur. Phys. J. C **44** (2005) 395 [arXiv:hep-ph/0503259].

[36] C. F. von Weizsäcker, Z. Phys. **88** (1934) 612; E. J. Williams, Phys. Rev. **45**, 729 (1934).

[37] P. Chen, T. L. Barklow and M. E. Peskin, Phys. Rev. D **49** (1994) 3209 [arXiv:hep-ph/9305247].

[38] V. I. Telnov, Nucl. Phys. Proc. Suppl. **179-180** (2008) 81.

[39] R. Brock *et al.* [CTEQ Collaboration],

[40] R. K. Ellis, H. Georgi, M. Machacek, H. D. Politzer and G. G. Ross, Nucl. Phys. B **152** (1979) 285.

[41] R. S. Thorne and R. G. Roberts, Phys. Rev. D **57** (1998) 6871 [arXiv:hep-ph/9709442].

[42] G. Altarelli and G. Parisi, Nucl. Phys. B **126** (1977) 298.

[43] D. Amati, R. Petronzio and G. Veneziano, Nucl. Phys. B **140** (1978) 54. D. Amati, R. Petronzio and G. Veneziano, Nucl. Phys. B **146** (1978) 29.

[44] V. N. Gribov and L. N. Lipatov, Sov. J. Nucl. Phys. **15** (1972) 438 [Yad. Fiz. **15** (1972) 781].

[45] Y. L. Dokshitzer, Sov. Phys. JETP **46** (1977) 641 [Zh. Eksp. Teor. Fiz. **73** (1977) 1216].

[46] W. Furmanski and R. Petronzio, Phys. Lett. B **97** (1980) 437.

[47] G. Curci, W. Furmanski and R. Petronzio, Nucl. Phys. B **175** (1980) 27.

[48] G. Passarino and M. J. G. Veltman, Nucl. Phys. B **160** (1979) 151.

[49] J.A.M. Vermaseren, Symbolic Manipulation with FORM, Computer Algebra Netherlands, Amsterdam, 1991.

[50] A. Denner, Fortsch. Phys. **41** (1993) 307 [arXiv:0709.1075 [hep-ph]].

[51] R. Mertig, M. Bohm and A. Denner, Comput. Phys. Commun. **64** (1991) 345.

[52] G. Rodrigo, A. Santamaria and M. S. Bilenky, J. Phys. G **25** (1999) 1593 [arXiv:hep-ph/9703360].

[53] M. Bohm, A. Denner and H. Joos, *Stuttgart, Germany: Teubner (2001) 784 p* [54]

[54] R. Baier and K. Fey, Z. Phys. C **2** (1979) 339.

[55] L. Montanet *et al.* [Particle Data Group], Phys. Rev. D **50** (1994) 1173.

[56] R. M. Barnett *et al.* [Particle Data Group], Phys. Rev. D **54** (1996) 1.

[57] C. Caso *et al.* [Particle Data Group], Eur. Phys. J. C **3** (1998) 1.

[58] K. Hagiwara, S. Matsumoto, D. Haidt and C. S. Kim, Z. Phys. C **64** (1994) 559 [Erratum-ibid. C **68** (1995) 352] [arXiv:hep-ph/9409380].

[59] E. A. Kuraev and V. S. Fadin, Sov. J. Nucl. Phys. **41** (1985) 466 [Yad. Fiz. **41** (1985) 733]. G. Altarelli and G. Martinelli, *In *Ellis, J. (Ed.), Peccei, R.d. (Ed.): Physics At Lep, Vol. 1*, 47-57* O. Nicrosini and L. Trentadue, Z. Phys. C **39** (1988) 479. F. A. Berends, W. L. van Neerven and G. J. H. Burgers, Nucl. Phys. B **297** (1988) 429 [Erratum-ibid. B **304** (1988) 921]. W. Beenakker, F. A. Berends and S. C. van der Marck, Nucl. Phys. B **349** (1991) 323.

[60] O. Nicrosini and L. Trentadue, Phys. Lett. B **196** (1987) 551.

[61] V. N. Gribov and L. N. Lipatov, Sov. J. Nucl. Phys. **15** (1972) 675 [Yad. Fiz. **15** (1972) 1218].

[62] M. G. Bowler, Z. Phys. C **11** (1981) 169.

[63] B. Andersson, G. Gustafson and C. Peterson, Z. Phys. C **1** (1979) 105.

[64] X. Artru and G. Mennessier, Nucl. Phys. B **70** (1974) 93.

[65] J. D. Bjorken, Phys. Rev. D **17** (1978) 171.

[66] C. Peterson, D. Schlatter, I. Schmitt and P. M. Zerwas, Phys. Rev. D **27** (1983) 105.

[67] F. James and M. Roos, Comput. Phys. Commun. **10** (1975) 343.

[68] T. Hahn, Comput. Phys. Commun. **168** (2005) 78 [arXiv:hep-ph/0404043].

[69] W. J. Marciano, Phys. Rev. D **29** (1984) 580.

[70] W. M. Yao *et al.* [Particle Data Group], J. Phys. G **33** (2006) 1.

[71] P. Nason and C. Oleari, Nucl. Phys. B **565** (2000) 245 [arXiv:hep-ph/9903541].

[72] G.Kramer: /it Private Communication

[73] C. Sandoval,

[74] W. K. Tung, H. L. Lai, A. Belyaev, J. Pumplin, D. Stump and C. P. Yuan, JHEP **0702** (2007) 053 [arXiv:hep-ph/0611254].

[75] M. R. Whalley, D. Bourilkov and R. C. Group, arXiv:hep-ph/0508110.

[76] B. A. Kniehl and L. Zwirner, Nucl. Phys. B **621** (2002) 337 [arXiv:hep-ph/0112199].

[77] B. Pötter, Eur. Phys. J. direct C **1** (1999) 5 [arXiv:hep-ph/9707319].

[78] I. F. Ginzburg, G. L. Kotkin, V. G. Serbo and V. I. Telnov, Nucl. Instrum. Meth. **205** (1983) 47.

[79] J. Binnewies, B. A. Kniehl and G. Kramer, Phys. Rev. D **52** (1995) 4947 [arXiv:hep-ph/9503464].

[80] M. Cacciari, M. Greco, B. A. Kniehl, M. Kramer, G. Kramer and M. Spira, Nucl. Phys. B **466** (1996) 173 [arXiv:hep-ph/9512246].

[81] J. Hakkinen and H. Kharraziha, Comput. Phys. Commun. **100** (1997) 311 [arXiv:hep-ph/9603229].

[82] B. A. Kniehl, G. Kramer, I. Schienbein and H. Spiesberger, Phys. Rev. D **79** (2009) 094009 [arXiv:0901.4130 [hep-ph]].

[83] D. E. Acosta *et al.* [CDF Collaboration], Phys. Rev. Lett. **91** (2003) 241804 [arXiv:hep-ex/0307080].

[84] J. Pumplin, H. L. Lai and W. K. Tung, Phys. Rev. D **75** (2007) 054029 [arXiv:hep-ph/0701220].

[85] G. Kramer and H. Spiesberger, Phys. Lett. B **679** (2009) 223 [arXiv:0906.2533 [hep-ph]].

[86] S. Chekanov *et al.* [ZEUS Collaboration], Phys. Lett. B **649** (2007) 111 [arXiv:hep-ex/0702034].

[87] M. Gluck, E. Reya and A. Vogt, Phys. Rev. D **46** (1992) 1973.

[88] P. M. Nadolsky *et al.*, Phys. Rev. D **78** (2008) 013004 [arXiv:0802.0007 [hep-ph]].

[89] J. W. Gary, arXiv:hep-ex/9903020.